Die approbierte Originalversion dieser Dissertation ist in der Hauptbibliothek der Technischen Universität Wien aufgestellt und zugänglich.
http://www.ub.tuwien.ac.at

The approved original version of this thesis is available at the main library of the Vienna University of Technology.
http://www.ub.tuwien.ac.at/eng

TECHNISCHE UNIVERSITÄT WIEN
Vienna | Austria

DISSERTATION

# Flow regulation of hemostasis by the mechano-sensitive protein von Willebrand Factor

ausgeführt zum Zwecke der Erlangung des akademischen Grades eines Doktors der technischen Wissenschaften unter der Leitung von

Prof. Dr. Günter Allmaier

E166

Institut für Chemische Technologien und Analytik

eingereicht an der Technischen Universität Wien

Fakultät technische Chemie

von

Dipl. Ing. Klaus Bonazza

0325540

Bennogasse 23/39, 1080 Wien, Austria

Wien, am 20.1.2016

# Contents

1. Hemostasis overview ..... 2
2. FVIII Structure and Function ..... 2
2.1. FVIII Structure ..... 2
2.2. FVIII Activation ..... 3
2.3. Role of FVIIIa in the Activation Cascade ..... 4
2.4. FVIII bio-synthesis ..... 5
3. Von Willebrand Factor Structure ..... 5
4. VWF Function ..... 6
4.1. Interaction with ADAMTS13 ..... 7
4.2. Interaction with Collagen ..... 9
4.3. Interaction with GPIb and GPIIb/IIIa ..... 9
4.4. Storage, secretion and clearance ..... 10
4.5. VWF Biophysics ..... 12
4.5.1. Influence of flow to VWF ..... 12
4.5.2. Flow dependent functions of VWF ..... 12
5. Sources of VWF and FVIII ..... 13
6. Interaction between VWF and FVIII ..... 13
7. Methods ..... 15
7.1. Atomic force microscopy ..... 15
7.1.1. History and working principle ..... 15
7.1.2. Dynamic AFM modes ..... 16
7.1.3. High resolution bio-AFM ..... 17
7.1.4. High speed AFM ..... 18
7.1.5. AFM for protein structures ..... 20
7.2. Generation of shear-flow ..... 21
8. Aims and Goals of this thesis ..... 22
9. Papers ..... 22
10. Summary of Results and their Significance ..... 62
11. References ..... 63

# 1. Hemostasis overview

The vasculature is constantly exposed to friction from the flowing blood plasma and impacts of blood cells, which results in minor defects of the sub-endothlium at neuralgic points, and is occasionally injured by external invasion. Hemostasis is a well-controlled protective mechanism that prevents substantial blood loss and prepares wound healing. The process in which bleeding is suppressed can be divided into two parts, primary and secondary hemostasis.

Primary hemostasis means the recruitment of platelets to a site of vascular injury forming a primary plug which is also called white thrombus. In this very fast step, von Willebrand factor (VWF) serves as a bifunctional linker between platelets and the vessel wall. Primary hemostasis is controlled by shear-rates and by the multimer-size dependent (protease dependent) pro-coagulant potential of VWF. In this context it should be mentioned that injured vessels contract and cause locally increased shear rates.

Secondary hemostasis leads to a reinforcement of the primary platelet plug by a fibrin network. Also red blood cells are part of the compound, thus these structures are called red thrombi. Formation of fibrin networks from fibrinogen is regulated by a complex activation cascade in which Factor VIII (FVIII) plays a central role. More than 15 factors, receptors and other regulators are involved in activation of secondary hemostasis, each of them being a working point for up- and down-regulation. VWF is indirectly involved by stabilizing FVIII.

The processes of primary and secondary hemostasis are strongly intertwined, as essential parts of the activation cascade require the platelet´s phospholipid surface and an increased concentration of $Ca^{2+}$, which is secreted by activated platelets, hence platelet recruitment and platelet activation are preconditions for secondary hemostasis.

# 2. FVIII Structure and Function

## 2.1. FVIII Structure

The glycoprotein FVIII is a heterodimer consisting of a light chain (LC) with a molecular weight of 80 kDa and a heavy chain (HC) of variable size, ranging from 90 to 180 kDa [1]. The chains are associated by a central ion, which has been identified as $Cu^{2+}$ in earlier biochemical studies. In addition, the structure contains another bond $Cu^{2+}$ and two $Ca^{2+}$ ions which presumably contribute to stabilize the molecule as they are coordinated by glutamate and aspartate residues [2]. A crystal structure of B-domain deleted FVIII is shown in Figure 1, whereas full length FVIII could not be crystallized.

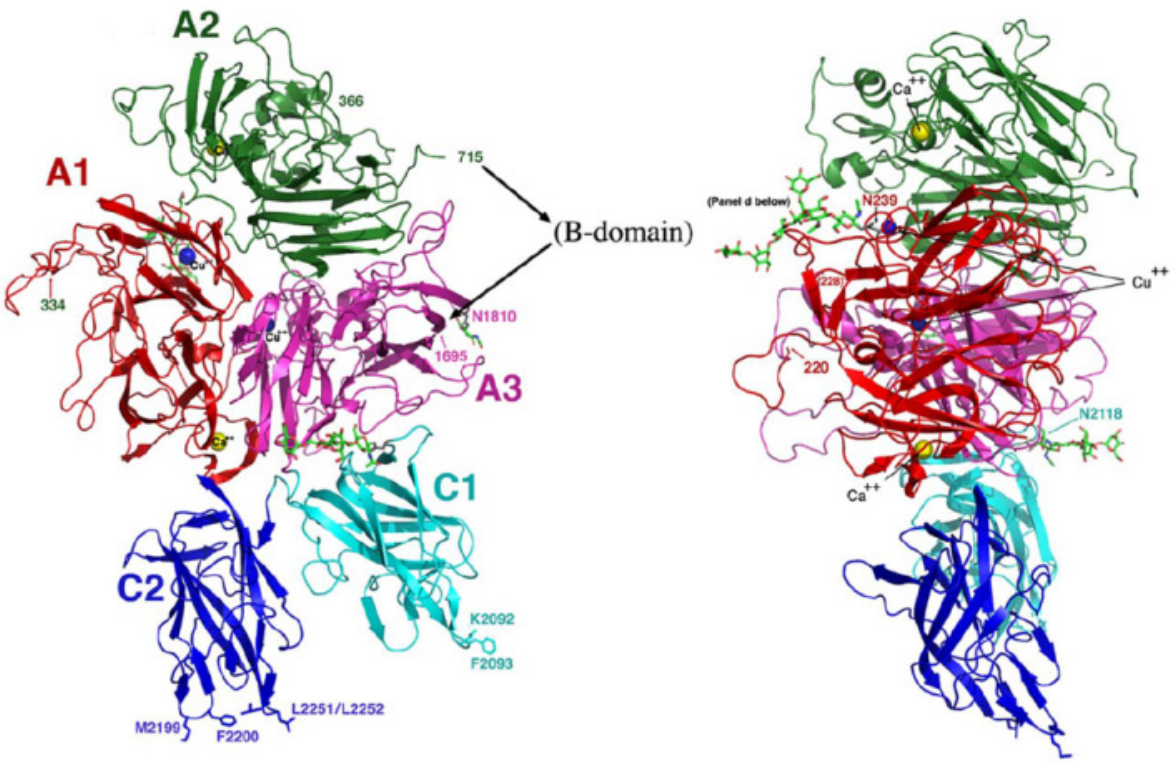


**Figure 1. (Source: Shen et al. [2]) Crystal structure of B-domainless FVIII.** 2 $Cu^{2+}$ are shown as blue globes and 2 $Ca^{2+}$ ions are colored in yellow. 3 sugar chains are depicted in light green.

The heavy chain includes domains A1a1, A2a2 and variable fractions of B. The light chain carries domains a3A3, C1 and C2. The lowercase characters denote linker regions between domains. a3 is acidic and plays a role in metal-ion coordination as well as in binding VWF. 3 well-ordered N-linked oligosaccharides are resolved in the crystal structure, but most glycosilations are located at the flexible B-domain.

## 2.2. FVIII Activation

Activation of FVIII is required for its cofactor activity in the X-ase complex. The heterodimer is thereby cleaved by thrombin within the heavy chain at residues 372 and 740, which is accompanied by elimination of the B-domain, and in the light chain at position 1689. The latter cleavage site removes the acidic a3 region which was considered to be essential for the release from the VWF complex [1] but is now in doubt because of the alternative FVIII release mechanism presented in this work. The resulting hetero-trimer FVIIIa is stabilized by the phospholipid membrane of platelets in presence of $Ca^{2+}$.

## 2.3. Role of FVIIIa in the Activation Cascade

Activated FVIIIa is essential for the formation of the Factor X activation complex (FXa, ten-ase complex) in the intrinsic pathway of the coagulation cascade depicted in Figure 2. As FXa converts prothrombin (FII) to thrombin (FIIa), which activates FVIII, this is a self-perpetuating circuit. FIXa on the one hand stabilizes FVIIIa on the other hand plays a role in its inactivation [1]. Most importantly, pro-coagulant participation of FVIIIa in the ten-ase complex requires phospholipid surfaces, especially phosphatidylserine (PS) which is abundant in the membrane of activated platelets. FVIII binds to phospholipid with its C2 domain[2], which appears to be also involved in VWF binding [3]. It is still controversial if PS binding is in concurrence to VWF binding, explaining FVIII release at sites of bleeding, or if FVIII activation by thrombin triggers its release. Interestingly, FX activation on the PS surface also requires $Ca^{2+}$. There is a $Ca^{2+}$ enriched environment at the surface of activated platelets because they secrete $Ca^{2+}$. The PS surface is often described as negatively charged (as in this sketch) but in presence of $Ca^{2+}$ a chelate complex occupies PS carboxyl- and phosphate-functionalities and can make the molecule neutral or positively charged. Furthermore, the electrostatic VWF-FVIII interaction is impaired by a salt effect. In this work it is shown that the VWF-FVIII interaction is also regulated by shear flow.

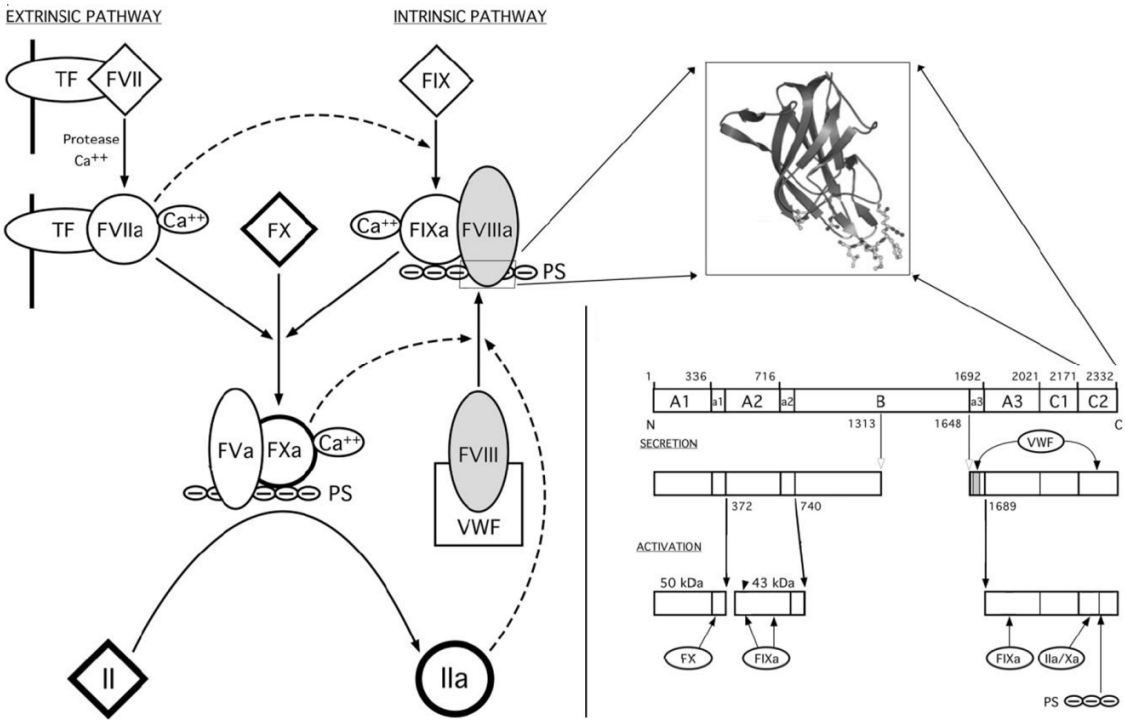


**Figure 2. (Source: Shen et al. [2]) FVIII in the activation cascade.** FX axtivation is mediated by an intrinsic and an extrinsic pathway. The extrinsic pathway consists of FVII activation via tissue factor (TF) and $Ca^{2+}$. In the intrinsic (essential) pathway FIX is activated by FVIIIa and $Ca^{2+}$ , which requires a phospholipid surface (PS). Anchorage of FVIII to PS is electrostatical and involves the C2 domain which is also engaged in VWF binding. In a self perpetuating circuit, activated FX converts pro-thrombin (FII) to thrombin (FIIa) which mediates FVIII activation. FVIII activation includes cleavage of the FVIII heterodimer to FVIIIa heterotrimer as depicted in the scheme on the right.

### 2.4. FVIII bio-synthesis

FVIII is mainly synthesized in the liver [1] although there are some indications that a part of FVIII is co-expressed and secreted together with VWF in certain cells [unpublished observation Lenting]. It is expressed as 2351 amino acids long precursor and subsequently the 19 acids signal peptide is cleaved. The mature protein is secreted as single chain and later cleaved into a light- and a heavy chain by a protease at residue 1648 and at two distinct sites within the B-domain, resulting in variable sizes of B-domains. Post translational modification includes N-linked glycosylation (mainly at the B-domain) and 6 sites of tyrosine sulphation.

## 3. Von Willebrand Factor Structure

VWF is the largest soluble glycoprotein in humans. It is a multimeric chain, circulating in blood in a wide range of multimer sizes. The smallest building unit of such multimer chains is a dimer (appr. 600kDa), the site of dimerization is located at the C-terminal ends. These dimers are linked to each other through two dimerization points close to the N-terminus at residues C1099 - C1099 and C1142 - C1142 providing a antiparallel, head-to-head and tail-to-tail concatement. Figure 3 shows the recently refined domain organization of the VWF monomer [4]. The mature subunit, which is found in multimeric form in the circulation, is composed of the domains D´D3, A1, A2, A3 the D4-assembly and the C-terminal "stem" region C1-CK. The pro-peptide , composed of D1- and D2-assemblies, is cleaved in the Golgi and serves as template for ordered storage of multimers [5] as explained later in more detail. Most VWF domains, except the A2 domain, are strongly disulfide cross-linked, moreover there are plenty of free cysteins. Several O- and N-linked glycans significantly contribute to the molecular mass.

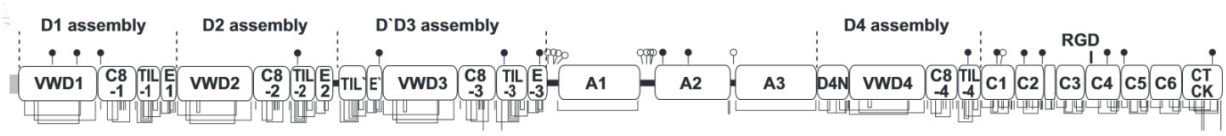


**Figure 3. (Source: Zhou et al. [4]) Recent refinement of the domain organization of VWF.** The D1 and D2 assemblies constitute the pro-peptide, the mature subunit consists of the D`D3 assembly, A1, A2 and A3 domains, D4 assembly and the domains C1-C6, CT-CK. Gray vertical lines and brackets symbolize free cysteins and disulfide bridges respectively. N-and O- linked glycanes are shown as closed and open lollipops.

The overall structure of VWF is much too large and flexible to be resolved all at once, neither with X-ray crystallography nor with NMR, but the last couple of years brought some breakthroughs in resolving the structures of domains A2 [6], A1 [7,8], A3 [9] and the cysteine knot dimerization region CT-CK [10]. Interestingly, all D-domains have resisted the rigorous attempts of crystallizing them. Especially the structure of the

D´D3 assembly, which hosts the FVIII binding sites, is of great interest and is therefore being resolved stepwise by NMR. This strategy resulted in solution structures of TIL [4], E` [3] and TIL`-domains [3], the latter one will be discussed later in view of FVIII binding.

## 4. VWF Function

Functions of VWF may be classified into hematological and other functions. For 3 decades VWF research was driven by pediatric tasks as early publications described VWF to fulfill dual functions in hemostasis, firstly as a fishing line for platelet recruitment in primary plug formation and secondly as a carrier protein for otherwise unstable FVIII. Before focusing on VWF as an ambivalent, beneficial and pathological agent in hemostasis, it should be mentioned briefly that this molecule carries multiple effectors which are soluble in plasma and contribute to survival and disease linked phenomena, such as apoptosis, angiogenesis, bone remodeling, cancer etc. Moreover, some binding sites to immobile membrane receptors (most of them integrins or similar glycoproteins) have been identified which explain its role in inflammation (including atherosclerosis and stroke), cancer suppression but also metastasis [11]. Table 1 summarizes most of the known VWF binding molecules and their physiological functions.

**Table 1. VWF binding ligands. (Source: Lenting et al. [11], modified)**

| Name | Binding domain | Site of interaction | Physiological function |
|---|---|---|---|
| **VWF pro-peptide** | D´D3 | Endothelial cells, platelets | VWF synthesis and folding |
| **FVIII** | D´D3 | Circulation, some endothelial cells | Secondary hemostasis |
| **p-selectin** | D´D3 | Endothelial cells | Inflammation |
| **$\beta_2$-integrins** | D´D3, A1, A2, A3 | Leukocytes | Inflammation |
| **Glycoprotein Ib (GPIb)** | A1 | platelets | Primary hemostasis |
| **Osteoprotegrin** | A1 | Circulation, endothelial cells | Bone re-modelling |
| **$\beta_2$-Glycoprotein I** | A1 | Circulation | Clearance of micro-particles and lipopolysaccharides |
| **P-selectin GP ligand-1** | A1 | Leucocytes | Inflammation |
| **Collagen VI** | A1 | Sub-endothelial matrix | Hemostasis |
| **ADAMTS 13** | A1, A2, A3, D4 | Circulation | Hemostasis |
| **Collagen I** | A3 | Sub-endothelial matrix | Hemostasis |
| **Collagen III** | A3 | Sub-endothelial matrix | Hemostasis |
| **Thrombospondin** | A3 | Circulation | |
| **IGFBP-7** | D4-CK | Circulation, endothelial cells | Angiogenesis |
| **$\alpha_{2b}\beta_3$ (GPIIb/IIIa)** | C4 | Platelets | Hemostasis |
| **$\alpha_5\beta_3$** | C4 | Endothelial cells, tumor cells | Apoptosis, angiogenesis |

| | | | |
|---|---|---|---|
| **Fibrin** | C1-C6 | Thrombus | Hemostasis |
| **CTGF/CCN2** | CK | Endothelial cells | Angiogenesis |
| **Galectin-1** | Glycanes | Circulation, endothelial cells | Angiogenesis |
| **Galectin-3** | Glycanes | Circulation, endothelial cells | Angiogenesis |
| **Siglec-5** | Glycanes | Macrophages | Inflammation |
| **Angiopoietin-2** | Unknown | Circulation, endothelial cells | angiogenesis |
| **Interleukin-8** | Unknown | Endothelial cells | Inflammation, angiogenesis |
| **LRP-1** | Unknown | Macrophages | Clearance |

With regard to hematology, VWF on the one hand promotes primary and secondary hemostasis acting as a linker between platelet receptor glycoproteins GPIb and GPIIb/IIIa and collagen types I, III and VI, and prolonging the half life time of FVIII in the circulation, on the other hand it has thrombogenic potential. The delicate balance between hemostatic and thrombotic effects depends on the regulation of multimeric size. After expression from the Weibel-Pallade bodies (storage granules in endothelial cells) VWF is processed by the cleaving protease ADAMTS13 (a disintegrin and metalloproteinase with a thrombospondin type 1 motif, member 13). The specific cleavage is force dependent as explained later in the biophysics section. This leads to preferential cleavage of the central monomers, which transmit summated hydrodynamic dragging forces of an entire chain, ending up with limited proteolysis. Modulation of VWF´s multimeric size is equivalent with regulation of its hemostatic/thrombogenic activity.

## 4.1. Interaction with ADAMTS13

Cleavage of the A2 domain by ADAMTS13 takes place between residues Y1605 und M1606 and requires previous unfolding [6,12-14]. The metalloprotease domain of ADAMTS13 cuts VWF chain as a result of a sophisticated 7-step, zipper-like interaction mechanism [15-17], shown in Figure 4. The 3 initial recognition steps include interactions of domains TSP 5-8 and CUP with the cross-linked domains CK - D4 of VWF and are therefore not force dependent. Indeed ADAMTS13 can bind to VWF under static conditions as shown in literature [16,17] and in this work. After force-induced elongation, additional recognition sites within the VWF A2 domain meet the steric requirements for the spacer domain and the disintegrin-like domain of ADAMTS13. Next, the metalloprotease domain binds to L1603, immediately next to the final cleavage site, followed by direct binding to the “scissile bond” (Y1605-M1606) which is subsequently cleaved. After cleavage the ADAMTS13 molecule is released, this crucial fact will be discussed later.

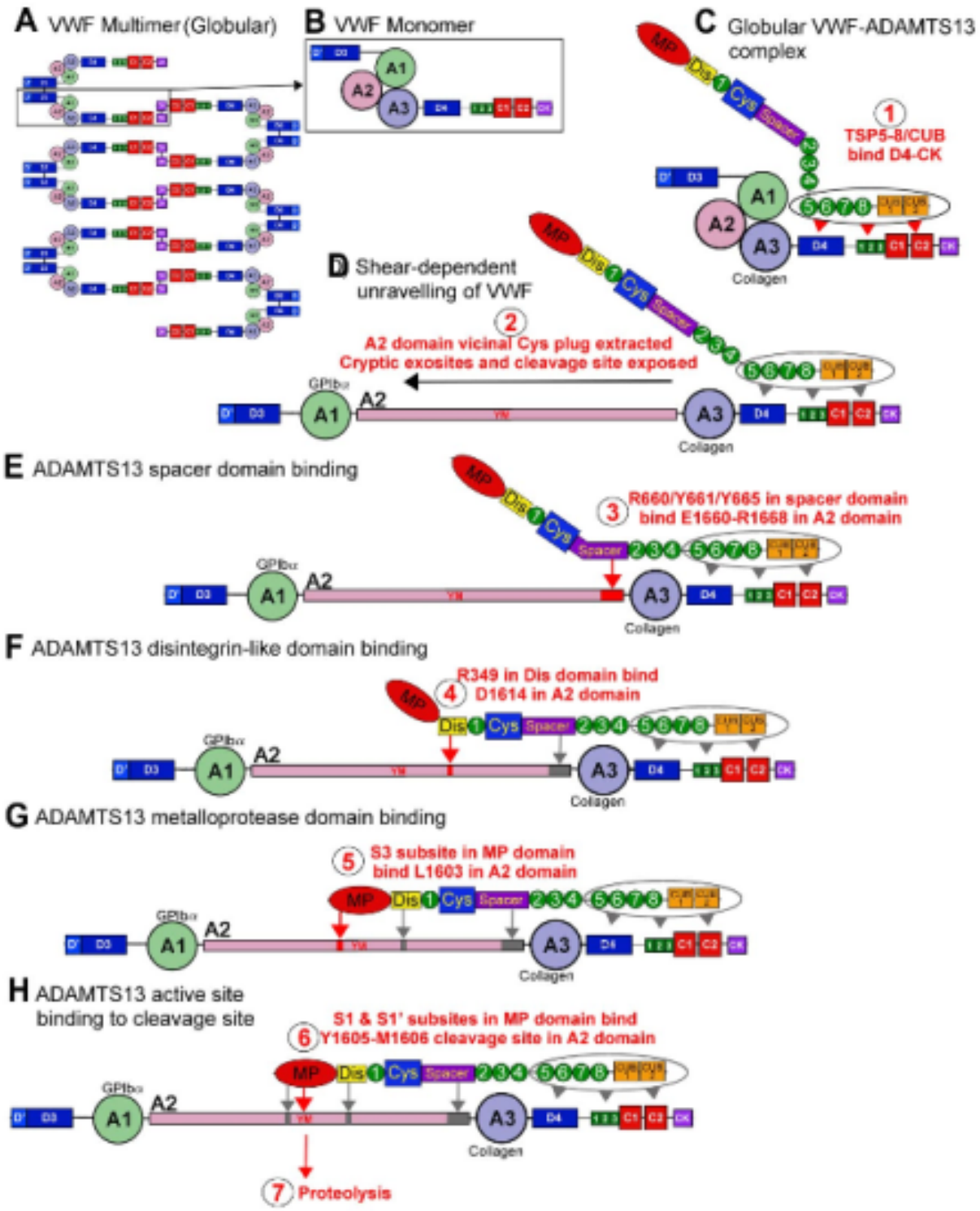


**Figure 4. (Source: Crawley et al.) Mechanism of recognition and cleavage of VWF by the protease ADAMTS13.** (A) head to head, tail to tail concatement of the circulating VWF multimer, (B) VWF monomer, (C) first recognition step via TSP- and CUB-domains, (D) 2nd step, shear dependent A2 unravelling, (E) 3rd step, binding of spacer domain, (F) 4th step, disintegrin domain binding, (G) 5th step, the metalloprotease domain binds A2 at a YM-vicinal position, thereby tightly crabbing the substrate. (H) 6th step, recognition of the YM (Y1605-M1606) scissile bond enabeling the 7th step, the actual proteolysis.

## 4.2. Interaction with Collagen

VWF binds collagen types I and III via its A3-domain and collagen type VI via its A1 domain. At sites of vascular injury, collagen rich surfaces are exposed to the blood flow. VWF then plays its role as an adhesive linker between collagen and platelets, triggering the formation of a white thrombus. Under static conditions the specific A3 binding to the homo-trimer collagen III dominates [18], whereas at higher shear rates the scenario might change, however no data on specific collagen-VWF interactions under flows exists. VWF adhesion to collagen is strongly enhanced by hydrodynamic flow [19] which is not understood on a detailed level as it seems contradictory to the end-to-end cross-linkage of both, A1 and A3 domains.

## 4.3. Interaction with GPIb and GPIIb/IIIa

The receptor GPIb is the most studied specific binding site for VWF on platelets. It interacts with the A1 domain forming the first interaction when platelets are captured from flow, prior to activation. The crystal structure of GPIb shows a hairpin-like conformation with a β-switch close to the C-terminus. In Figure 5 the crystal structure of the GPIb-A1 complex is depicted. The principle of interaction is the formation of a super β-sheet between the A1 β3- and GPIb β14-strands.

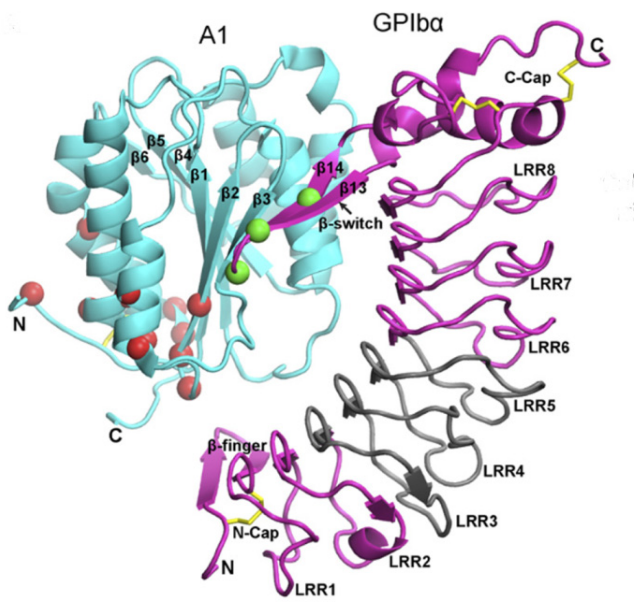


**Figure 5. (Source: Springer et al. [5]) Crystal structure of the A1- GPIb complex.** The interaction is based on the formation of a super ß-sheet, comprising ß1-ß3 strands of VWF A1 domain and the ß14-ß15 switch of GPIb. Red and green spheres are sites of possible mutations that might destabilize or stabilize the complex. The grey part of the GPIb hairpin structure is important for A1-GPIb interactions under shear conditions. Disulfide bridges are colored in yellow.

Although, such a detailed understanding of binding under static conditions is available, it is still unclear how this complex can be formed in-vivo under shear conditions, because the super β-sheet formation requires a precise orientation which is contradictory to VWF´s ability to quickly catch a fast moving platelet (like a fishing line). Therefore, it is probable that the A1 domain assumes a high affinity state under shear flow, which cannot be studied by X-ray crystallography. A recent study that shows a force dependent on/off rate switching of VWF-GPIb binding gives a first experimental indication [20].

After tethering to the vessel wall, platelets get activated, exposing another membrane receptor with VWF binding affinity, namely GPIIb/IIIa, which binds to the VWF C4 domain (RGD motif) and reinforces the primary plug.

## 4.4. Storage, secretion and clearance

To understand VWF´s structure/function relationship, especially the shear-rate modulation of hemostasis, it is essential to consider the special way how VWF is assembled to multimers, stored and secreted into plasma. VWF is expressed as a 2813 amino acids large monomer, consisting of a 22 amino acid signal peptide, an 741 amino acids pro-peptide and the mature subunit with 2050 acids. The free C-termini dimerize covalently in the endo-plasmatic reticulum, whereas at this stage the N-termini are occupied by the pro-peptide, which is cleaved later in the Golgi by furin. The pro-peptide thereby serves as a template for the formation of dimeric bouquets which are then stored in virtually endless strings in tube shaped (crystalline) structures that can be found in Weibel-Pallade inclusion bodies (Figure 6). This is facilitated by an acidic environment in the Golgi and in the Weibel-Pallade bodies (pH 6,2). From there VWF is directly secreted into the blood flow were a neutral pH (7,4) is causing an opening of the dimeric bouquets. There is evidence that also ion concentration plays a role. The secretion process was directly observed using scanning ion conductance microscopy [21]. The ultra-large VWF strings are exposed to shear stress, unravelling there scissile bonds in the A2 domains as described above, and thereby processed to an average size of 20 monomers by the cleaving enzyme ADAMTS13.

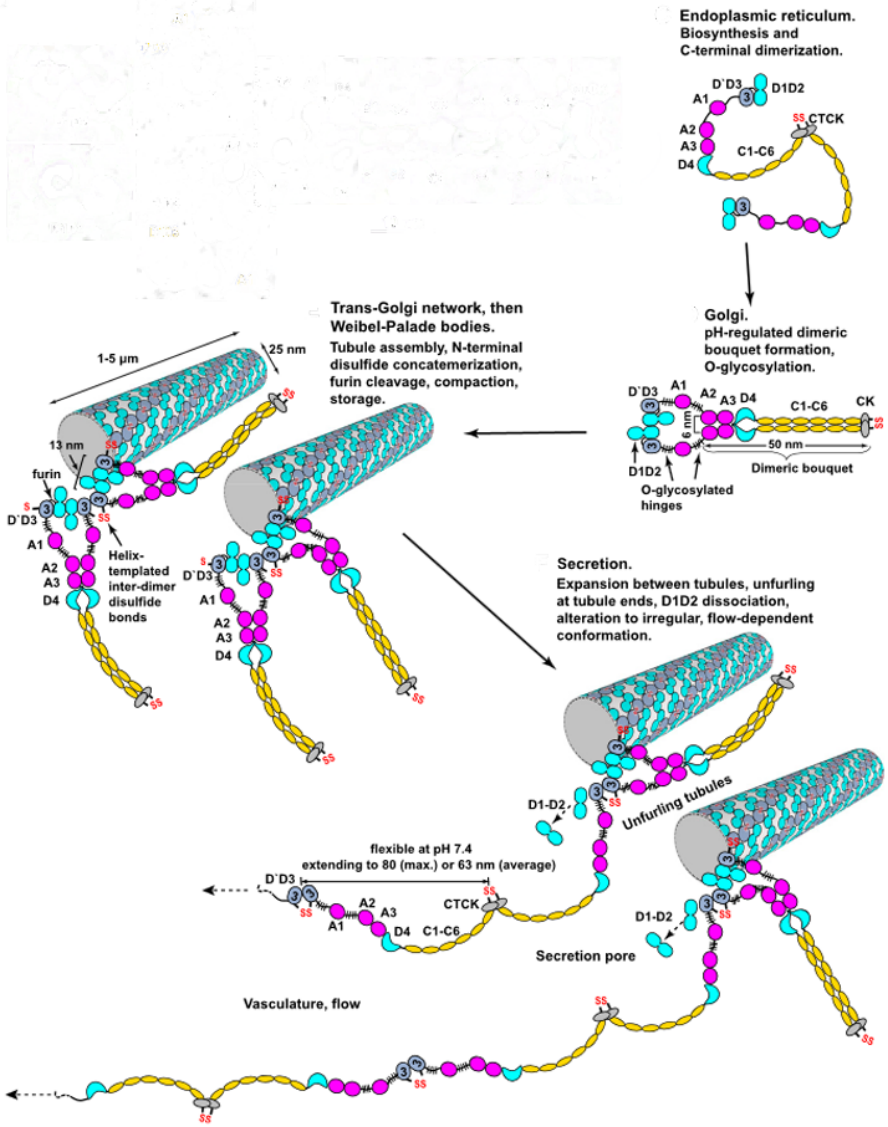


**Figure 6 (Source: Springer et al. [5]) Storage of VWF in the Weibel-Pallade bodies.** Occupation of N-termini by the propeptide domains A1A2 forces selective C-terminal dimerization in the endoplasmatic reticulum. A pH drop in the Golgi assists the formation of a dimeric bouquet, the propeptide thereby serves as a template. "Endless" chains of dimeric bouquets self assemble to tubular structures. Secretion into the circulation is facillitated by the neutral pH of blood which destabilizes the bouquets. The pro-peptide is cleaved by furin. A primary size modulation of VWF chains is part of the secretion process, as their release from the endothelium is induced by enzymatic clevage of the mechanosebnsitive A2 domain.

Secretion of VWF into the bloodstream is flow dependent. The same is true for its clearance. VWF quits its life-cycle through receptor induced endocytosis. The first step is binding of VWF to the membrane receptor LRP1, this was shown to be shear rate dependent [22]. Interestingly, VWF-LRP1 binding is dependent from shear-rate, but not from multimeric size (unpublished observation Lenting) which should be further tested as size dependent VWF clearance would provide a second pathway of VWF size regulation, beside cleavage by ADAMTS13.

## 4.5. VWF Biophysics

### 4.5.1. Influence of flow to VWF

VWF is a force sensitive molecule. Multimer chains have contour lengths of up to 1 µm and circulate in a loosely coiled conformation. Due to its supramolecular dimensions such chains respond to shear-rates (and other elongational flow conditions) by adopting a linear shape, thereby the force fields are translated into tensile forces along the molecular axis. A simulation which treated VWF as a chain composed of rigid globes, each exposed to Stokes friction and flexible, rod-like interconnections gave a theoretical dependence of shear-rate, chain-length and force [19]. The largest forces seamed to appear in the center of a chain. Recently the same authors refined this model and presented 2 force maxima at $\sim\frac{1}{3}$ from each end (unpublished observation A Alexander-Katz). Fluorescence and bright field video microscopy showed the formation of fibrillary structures that subsequently grow to form entire VWF networks [19] and circulating plugs [23]. It was jet unclear if in those experiments an elongation of VWF molecules was observed, however it is evident that the mayor effect leading to long fibers and networks is a flow dependent VWF-VWF crosslinking. The nature of this VWF agglomeration is uncertain. There are speculations that A1 and A2 domains, which exhibit intra-molecular low affinity interactions [24], might also form inter-chain bridges which would explain the reversibility of VWF plug formation in flow.

The wall shear rate can be divided in two contributions, a tumbling motion and an elongational component [14,25], the latter one is characterized by divergent vectors of flow. Such elongational flow fields where addressed experimentally using flow chamber geometries that represent stenotic vessels [26] T-junctions [27] and accelerated flow in general. These experiments were performed using video rate-optical microscopy and yielded collective properties of potentially interacting VWF chains. An attempt to prove single VWF molecule elongation data was published in 1996 [28]. VWF molecules, prior exposed to hydrodynamic shear, were imaged by AFM. Due to the low shear rates that were used in that study no VWF stretching is visible. The first single molecule visualization of VWF stretching is presented in this work. In general Blood is a non-Newtonian liquid and carries cells like macrophargs, red blood cells and platelets (in order of size from large to small). In physiological flow these large “particles” accumulate in the center of a vessel while there is a margination of plasma and small soluble compounds, including VWF. Close to the endothelial vessel wall there is a Newtonian flow regime. Pure VWF responds to flow by elongation, and self-assembly.

### 4.5.2. Flow dependent functions of VWF

In 2007 the first force dependent interaction of VWF was observed. Shear-stress triggered the tethering of VWF to collagen coated surfaces [19]. This counterintuitive behavior of increased adhesion in case of intensive wash-off forces is still not explained on a mechanistic level despite a structural understanding how collagen trimers interact with the VWF A3 and A1 domains [29,30] under static conditions.

When VWF is exposed to elongational force fields most domains of VWF experience tensile forces. The only domain which lacks far distance disulfide bonds is the A2 domain, hence this domain is unfolded as it was shown by optical tweezers [6,14,31] and AFM force spectroscopy [12]. Thereby, the so called scissile bond (Y1605-M1606) gets sterically accessible to the cleaving enzyme ADAMTS13 as explained above. The A2 unfolding takes place at appr. 18-25 pN and is dependent from $Ca^{2+}$ and $Zn^{2+}$ concentrations [31].

The A1 domain interacts with Platelet receptor GPIb as described above. Although the binding principle is now known [5,20], from a biophysical point of view there are plenty of open questions. VWF platelet binding appears to be shear-rate dependent, but due to the strong disulfide cross-linkage of the A1 domain it is not straight forward to assume an unfolding comparable to the A2 domain. There are two schools of thinking which partly explains this paradox: i) The tumbling component of flow causes rotation of platelets, VWF is wrapped around the platelet interacting with multiple GPIb receptors depending from the rotation. ii) A jet unknown, shear dependent high affinity state of the GPIb-VWF complex causes shear dependence on a single molecule scale. Recently a force dependent on/of rate switching has been demonstrated and assigned to the unfolding of a relatively short loop within the A1 domain of VWF [20].

In this thesis a shear-flow dependent binding of FVIII is presented. The FVIII binding D´D3 domain is strongly S-S linked and cannot be unfolded. A general explanation why cross-linked domains like A1, A3 or D´D3 respond to forces by switching affinities to other proteins is currently not available.

## 5. Sources of VWF and FVIII

Recombinant VWF and FVIII products used in this study were co-expressed in Chinese Hamster Ovular (CHO) Cells. FVIII was dissociated from VWF by addition of 500 mM $Ca^{2+}$ and separated by large scale size exclusion chromatography (SEC). This yielded full length FVIII and VWF containing an increased ultra-large fraction compared to plasma derived VWF of healthy donors [32].

FVIII is commercially available as “Advate” (Baxalta). VWF (named “BAX111”) is currently being evaluated as a drug candidate on basis of a phase 3 clinical trial. Both products are plasma and albumin free.

## 6. Interaction between VWF and FVIII

The VWF-FVIII complex is the main focus of this thesis. Free FVIII in the circulation has a short half-life time. Complex formation with VWF is stabilizing it by protecting it from premature activation and from clearance. 90% (in terms of monomers) of VWF is circulating without FVIII, as the FVIII : VWF monomer ratio is appr. 1 : 100 [11,33]. On the one hand the amount of bond FVIII appears to be limited by the availability of FVIII in plasma, as in-vitro experiments showed ratios up to 1 : 1 [34]. On the other hand

deficiency of VWF leads to a lack of FVIII in VWF knockout mice and in patients with von Willebrand disease (VWD) despite the ability of VWF to bind higher amounts of FVIII. FVIII binding to VWF is $Ca^{2+}$ dependent, which is used to purify FVIII after co-expression with VWF in some procedures of recombinant FVIII production. After activation, FVIII loses its binding affinity for VWF.

Despite a number of indirect observations the VWF-FVIII complex formation is still not understood on a mechanistic level. A crystal structure of B domain deleted FVIII is available since 2008 [2]. The B-domain is too flexible to allow crystallization. What the crystal structure ad to the understanding of VWF binding is the flexibility of the C2-domain and the 3D-localization of the acidic a3 region on the A3 domain between domains A2 and A1 which might contribute to both, the assembly of FVIII light and heavy chain and to VWF binding. Some biochemical experiments provide a certain basis for further studies: Potential VWF binding epitopes are located within the light chain as shown by experiments with monoclonal antibodies [34], but the light chain alone is insufficient to bind VWF. The only plausible explanation for this is the dual role of the acidic a3 region (light-heavy chain assembly and VWF binding). Moreover, these historical works reported at least two exosites contributing synergistically to VWF binding. The biggest obstacle in understanding the complex is the lack of structural information on the D´D3 domain of VWF. Early works restricted the FVIII binding region to the first 272 residues of the mature VWF, which, according to the newer nomenclature is the amino-terminal end of the D´D3 domain assembly. In a recent NMR work, a solution structure of the D´ domain was obtained, revealing a mayor FVIII binding area in a flexible loop region of the Til´ sub-domain [3] (Figure 7). This binding area consists of a positively charged surface patch which can interact electrostatically with the acidic a3 region, 8 times more strongly than VWF binds the C2-domain (affinities ~ 72 nM vs 564 nM), disproving the concept of two synergistic binding sites. This dominating electrostatic interaction is competing with ionic strength (explaining the FVIII release at high $Ca^{2+}$ concentrations) and with acidic phospholipid surfaces. However, there is still evidence of additional minor binding sites which might be located on the D3 domain of VWF and on the heavy chain of FVIII. The interplay between them is not jet fully understood.

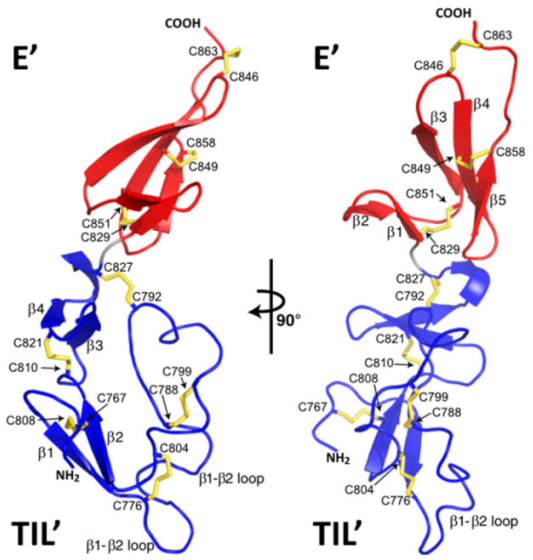


**Figure 7. (Source: Shiltagh et al. [3]) NMR structure of the N-terminal D´domain of VWF, which is responsible for FVIII binding.** The flexible loop region of TIL´ interacts with acidic regions within the FVIII light chain.

# 7. Methods

## 7.1. Atomic force microscopy

### 7.1.1. History and working principle

Atomic Force Microscopy (AFM) was established in 1986 by Gerd Binnig, Calvin Quate and Christoph Gerber [35] , basing on technological advances implemented in the Tunneling Electron Microscope [36] which was honored with the Nobel prize in Physics. The principle of AFM is to collect topographical information by scanning over the sample with a sharp tip. In contact, the dominating forces between tip and sample are repulsive forces which derive from the Pauli Exclusion Principle and decay with the 4$^{th}$ power of the distance. This gives AFM its exceptional sub-angstrom spatial resolution. Either the force (contact mode) or the amplitude (tapping mode) is kept constant by reading out the bending of a flexible cantilever were the tip is mounted on. This is nowadays achieved by the light lever principle. The reflection angle of a laser beam on the backside of the cantilever is very sensitive to its bending, enabling force measurement with pN precision. Scanning of the sample relatively to the tip position is realized with piezoelectric actuators, ether in a tip- or in a sample scanning setup, usually by the use of tubular piezo elements [37]. A scheme of an AFM setup is depicted in

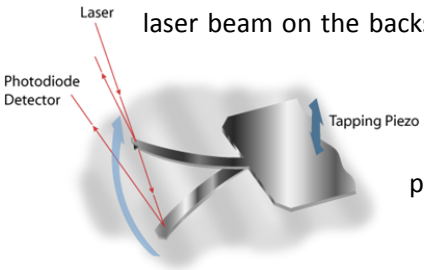


Figure 8.

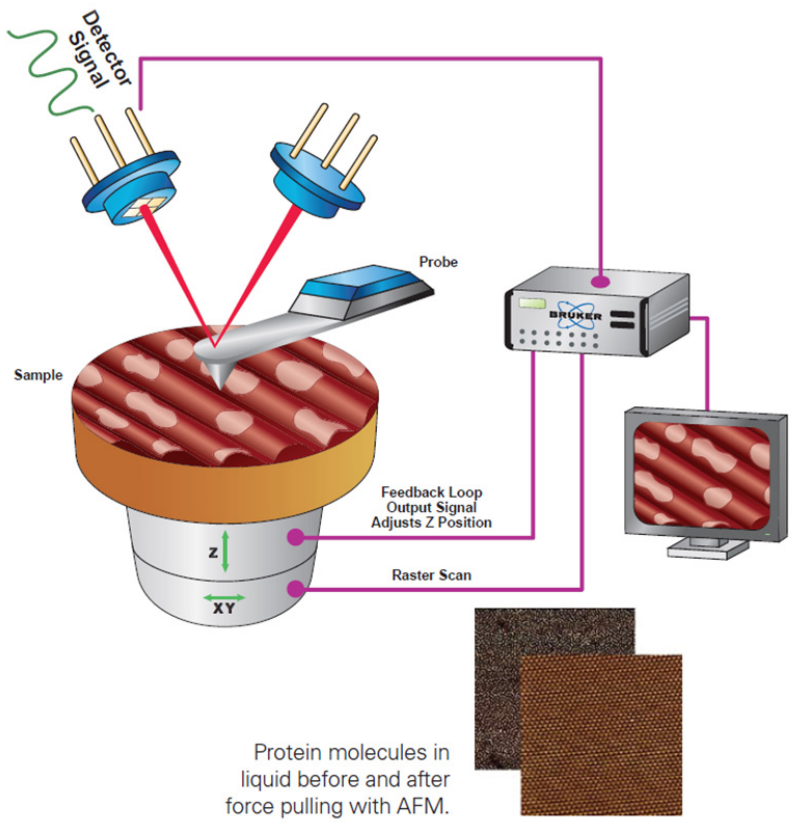


**Figure 8. Working principle of the AFM used for this thesis (Bruker Multimode 5).**

### 7.1.2. Dynamic AFM modes

As mentioned above AFM can be run in contact mode with a static tip or in a dynamic mode, which is also called tapping mode. Contact mode measurements are often invasive due to lateral forces and hence limited in terms of speed. Since the implementation of dynamic modes (invented 1987 [38]) into all commercial AFM microscopes, the use of contact mode is practically limited to special cases such as measuring of friction (lateral) forces and modes where electrical contact is required e.g. conductive AFM and tunneling AFM. Topography imaging is usually performed in dynamic modes. Since the invention of tapping mode [38], AFM has advanced to an efficient tool for biology [39]. It is now widely used for experiments from the cellular scale [40] down to the single molecule scale [41]. Bio-AFM is generally used to discover biology at physical extremes. In the following, some challenges in life-science which are currently affronted by AFM are described and the most crucial advances and new AFM modes are explained.

### 7.1.3. High resolution bio-AFM

In principle, AFM can yield spatial resolutions in the sub-angstrom range due to the extremely abrupt decay of repulsive forces in the Pauli regime. Working in a regime where these short distance forces dominate over electrostatic and van der Waals forces requires high total force levels. In air additional capillary forces from the water surface adsorbate film are unfavorable. Therefore, atomic resolution is achieved only in stable inorganic samples at low amplitude set-points (high forces) in liquids or vacuum. In biological samples, which are usually delicate, there is a tradeoff between invasiveness and resolution. Depending on the mechanical stability of the sample, tapping forces are limiting the resolution. Sub-molecular resolution is feasible in 2-dimentional protein assemblies, where each molecule is laterally fixed [41] and in rigid DNA double helix chains [42,43]. In contrast to this, single isolated molecules are much more mobile and hence more difficult to resolve [44]. Formation of self-assembled layers is therefore a frequently used strategy for enhancing resolution and resolving molecular details. However, tip radius and shape are crucial parameters for obtaining high resolution images. The ideal AFM tip is symmetric and atomically sharp, so theoretically just the first atom of the tip should interact with the sample. In soft, biological samples there is a certain indentation, meaning that at higher forces the interacting area of a cone-shaped or pyramidal tip is increased. In total there is an optimal force, hence a precise force control helps to obtain high resolution [43,44]. In classical tapping mode the actual tip-sample force is unknown, although qualitatively the operator can tune it by increasing or decreasing the amplitude set-point (damping). Several concepts to control the forces were invented and used for enhancing resolution:

a) Peak Force Tapping mode: The cantilever is driven with a fixed frequency below resonance. Both, rectangular (JPK) or sinus shaped (Bruker) actuation profiles are used to record linear or non-linear force distance curves at each pixel. A similar concept but slower and with lower resolution was used before, which was called force-volume mode (force-distance “multiplied” by the area). The knowledge of force distance and force-time curves enables easy force control and imaging at a defined force set-point, which can be used to obtain enhanced resolution [45]. In addition force control is highly desirable also in terms of nano-mechanical mapping. From the force curves, information like Youngs modulus, adhesion forces and peak force can be extracted, which is used for quantitative nano-mechanical imaging [46].
b) Multi-frequency AFM: Higher harmonic oscillations of an excited cantiler are analyzed and the tip-sample interaction forces are extracted by a mathematical model [47].
c) The bandwidth of multi-frequency AFM can be significantly enhanced by special cantilerver designs which cause a secondary oscillation with a different frequency. Such geometries can be seen as a “cantilever on a cantilerver”. The most successful geometry so far is a T-shaped cantilerver (Figure 9). Only the mayor bending oscillation is driven acoustically whereas the minor, torsional oscillation is due to interactions with the substrate [48]. A similar concept was realized in another lab by modifying a cantilever, creating a grid of slotting holes. The very end of the cantilever gets more flexible, like a small cantilerer mounted on the big one allowing a second resonance frequency. When the second cantilever is bent (relatively to the first one) the

diffraction pattern of the reflected laser beam changes and the frequency of the small cantilever can be read out (unpublished data Manish Butte).

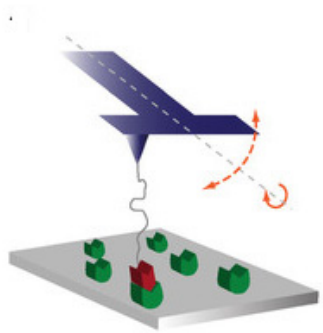

**Figure 9. (Source: Sahin et al. [48]) Working principle of T-shaped, torsional cantilevers.** The red arrows indicate the bending and the torsional motion. The sketch shows a recognition imaging application, the technique can also be applied for conventional stiffness mapping.

As tip-sample forces appear to be an important parameter for high resolution imaging of soft samples, also the duration of these forces, i.e. the force-time profiles, should be discussed. It results that force mapping performed at extremely high speeds yields significantly higher forces (observations O Sahin and M Butte). The same is true for high speed force spectroscopy were higher pulling velocities lead to unusually stiff molecules [49]. An explanation is that every interaction, e.g. between tip and sample, or intramolecular like in force spectroscopy, can be seen as a chemical bond with a certain life-time, meaning that there is an equilibrium between bound and unbound state. Averaging over milliseconds and seen at the length scale of a single bond, an apparently low binding force might mask the coexistence of a strong binding with short life-time and an unbound state with much longer life-time. An AFM tip that touches the sample just very shortly (and thus excluding time-averaging) selectively recognizes the strong interactions and the sample appears much stiffer. This is an issue for accurate force mapping but the effect can be helpful for high resolution imaging. In fact, miniaturized cantilevers which oscillate at higher resonance frequencies were successfully used for enhancing bio-AFM resolution [42,43].

### 7.1.4. High speed AFM

The great advantage of AFM in biology and medicine is the possibility of taking images in liquids, which enables studying processes in near-biological or -physiological environment. At a cellular length scale plenty of breakthroughs were made in the last decades, such as in-situ imaging of cell division [50] and several cases of cells changing their surface morphology or stiffness [39,40,46,47]. Down at the molecular scale, the crux is that most processes are very fast. Therefore, AFM was pushed to striking speed especially in the last 10 years. Some speed limiting factors are discussed in the following, along with the corresponding technical solutions:

a) Resonance frequency of the cantilerver: Self-evidently faster scanning requires faster oscillation of the cantilever. The resonance frequency is correlated with the spring constant. A common and successful way of obtaining high resonance frequencies, and at the same time keeping the spring stiffness low enough for non-destructive imaging, is miniaturization. While conventional cantilevers are ~120 µm long, the newest generation of commercial cantilevers is just 4 µm long. Such ultrashort cantilevers oscillate with frequencies of up to 10 MHz. A further miniaturization is on the one hand limited by the optical readout of cantilever position, on the other hand by the acoustical excitation. State of the art high speed AFMs have a very small laser spot size and special measures to realize fine laser alignment to the small backside area of the cantilever. Reflective metal coating is standard. Cantilevers smaller than ~20 µm by 10 µm, show diffraction patterns in the reflected beam. Heating of the cantilever is also an issue as local temperatures can exceed 100°C. Excitation of cantilevers is generally realized acoustically by a piezo-electric actuator. The complicated oscillating system, which results from indirect drive (cantilever, holder, sealing and fluid are excited) is typically reflected by numerous parasitic peaks in the oscillograph and lower stability of measurement. Therefore, thermal excitation, based on one-sided pulsed laser heating of the bi-metal cantilever, is gaining more importance. This has been implemented in a commercial AFM (Asylium Bluedrive). Recently, laser thermal driving has been used even for peak force tapping with excitation below resonance [G. Fantner submitted].

b) Quality factor: The quality factor describes the decay of amplitude after excitation.

$$Q = 2\pi \frac{stored\ energy}{dissipated\ energy} = \frac{\sqrt{mk}}{D}$$

m... effective mass of the cantilever
k… spring constant
D… damping coefficient

In principle a high Q-factor is desired as it is beneficial for the sensitivity, but the drawback of high Q-factors is that they limit scanning speed. The feedback loop of the AFM relies on damping of the amplitude (in case of amplitude modulation), thus with a high Q-factor, which means low damping coefficient and low energy dissipation per cycle, more oscillations are required until the feedback responds. This means slower feedback at the same oscillation frequency. In liquid the Q-factor is reduced due to the hydrodynamic drag, which is slightly reducing the sensitivity but contributes to high speed scanning. In air Q-factors are higher and thus imaging at high line-rates is very limited. There are attempts to reduce Q by fabricating polymer cantilervers with higher damping coefficients and lower mass [G. Fantner]. In vacuum Q is extremely high. On the one hand scanning speed is actually very limited under vacuum, on the other hand the problem is partially circumvented by using frequency modulation instead of amplitude modulation.

c) Scanners: If high speed AFM is used for scanning small areas with high frame-rates, another challenge appears beside the achievement of high tip velocities, namely the mass inertia of the

scanned (moved) components. There are generally two designs of AFMs, the tip scanning and the sample scanning configuration. Especially for biological applications tip scanning models are favored, because the immobile sample allows implementation of optical microscopes. For the specific case of high speed AFM it is more usual to scan the sample which should be then as small and light as possible. Also the scanner itself is miniaturized to reduce inertia, which leads to maximal scanning areas as small as 0,5 by 1 µm. The classical geometry, used for the vast majority of standard scanners, is a multi-segment piezo tube [37]. In high speed AFM the vertical (z) direction is most critical in terms of fast scanner feedback. Also in z-direction there are usually smaller requirements for the maximal range (for scanning, not for force spectroscopy). Therefore, two different strategies were pursued: The usage of 3 individual linear piezos for x, y, and z direction [51-53] or an upgrade of the tubular scanner by an additional small range z-scanner [Bruker].

### 7.1.5. AFM for protein structures

AFM was invented as a method for analyzing surfaces. A recent development, which uses AFM as a tool for obtaining 3D-structural information of proteins, is loosening this paradigm. The protein is specifically labeled at two distinct positions with different, short (6 base pairs long) single stranded DNA pieces. T-shaped torsional cantilevers [48,54], which were described above, are used for high resolution force mapping. The tip is functionalized with a 12 base pairs long single stranded DNA piece, containing the complementary sequences for both labels. This enables the tip to recognize both labels and to distinguish them by their different force signatures which occur because the label-DNAs bind the tip-DNA at different positions (Figure 10). This procedure yields the distance of two distinct residues within the protein with a precision of 2 Å [54]. Next, this is repeated with different labels until the 3D-structure or at least the features of interest are resolved.

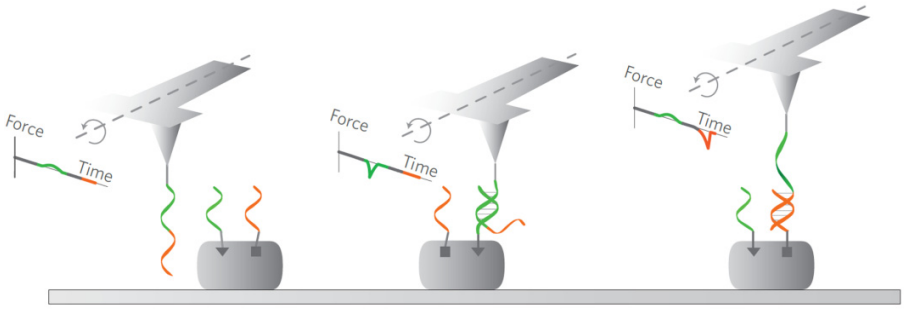


**Figure 10. (Source: Kim et al. [54]) Principle of resolving protein structures by AFM.** Two different sequences of short single-stranded DNA (green and orange) can be distinguished by their different specific signatures in the force-time diagram. The complementary sequences immobilized on the AFM tip are also colored in green and orange respectively. The left image shows a force pattern with minor repulsive forces, typical for the non-binding case. The middle image shows a strong attractive force peak of the green sequence-match which comes earlier than in the right case (orange sequence-match) where the green sequence has to be stretched first, causing a time delay. This is used to measure the distance between the two labels.

It should be pointed out that this method for structure determination is performed in liquid and does not require crystallization. In principle it is not restricted to a certain size of molecules. Furthermore, this has the potential to record time resolved structural changes.

## 7.2. Generation of shear-flow

Simulation of physiological conditions by generating shear-flow was a major key of this thesis. Some techniques that were previously used for shear experiments, particularly for VWF studies, should be presented. In the blood circulation laminar flow is predominant due to the small characteristic length and a relatively moderate flow velocity which typically results in Reynolds numbers below 1000. (Wall-) shear-rates $\gamma$ are reminiscent for laminar flow and are defined as the velocity gradient within the liquid. In order to highlight this, corresponding literature refers to laminar flow as “shear-flow”.

$$\gamma = \frac{dv}{dz}$$

$v$… liquid velocity

z… surface perpendicular distance

The goal of any setup for flow experiments is either to ensure straight forward and precise calculation of the shear-rate (by generating linear or parabolic velocity profiles), or to mimic some patho-physiologically relevant geometries, like stenotic or partially plugged vessels.

The classical way of analyzing stretched VWF is a plate-plate or plate-cone rheometer. It is a standard for shear-rate dependent coagulation essays but does not provide the experimental flexibility to study reversible phenomena or single molecule effects. An easy but qualitative method for investigating hydro-dynamically stressed VWF is the exposure to Vortex flow, which was successfully used to determine the influence of platelets, FVIII and ions on the ADAMTS13 mediated proteolysis of VWF [55-57], thereby distinguishing between a static and a flow-case. Due to the non-laminar flow the actual “shear-rate” is unknown. A first attempt to image stretched VWF multimers by AFM was carried out in 1996 [28], a mica substrate which rotated in a VWF solution was subsequently imaged. The setup was basically a half plate-plate rheometer which lacked the fixed counter-plate. In this way no sufficient shear-rate was generated to significantly elongate VWF. The usage of on-line methods, capable to visualize VWF while the force field was on, finally, lead to the first real visualization of shear-induced formation of fibers and networks. Schneider et.al. used surface acoustic waves to pump a VWF solution through a microfluidic system and detected the reversible formation of VWF fibers and networks in real-time by fluorescence microscopy [19]. Observations of VWF bundle formations with light microscopy was also used to study a) a stenotic geometry, reveling that VWF elongation does not require shear-rate gradients (elongational flow) when the absolute shear-rate is sufficiently high[26], b) a geometry which caused a stagnation point flow [27] and c) the reversible formation of blood clots in whole blood [23]. These online methods showed nicely the dynamics of VWF self-aggregation but they were not able to distinguish between single VWF

multimer-molecules and VWF bundles, therefore the relation between shear-rate, elongation and functional changes remain an open question. In this thesis a microfluidic plate-plate rheometer-like device was used to stretch VWF (Figure 11.). A part of the molecules remain attached to the stationary plate (a mica sheet), which prevented recoiling. These single, stretched VWF molecules were subsequently analyzed by AFM. The micro-rheometer is described in more detail in the attached paper.

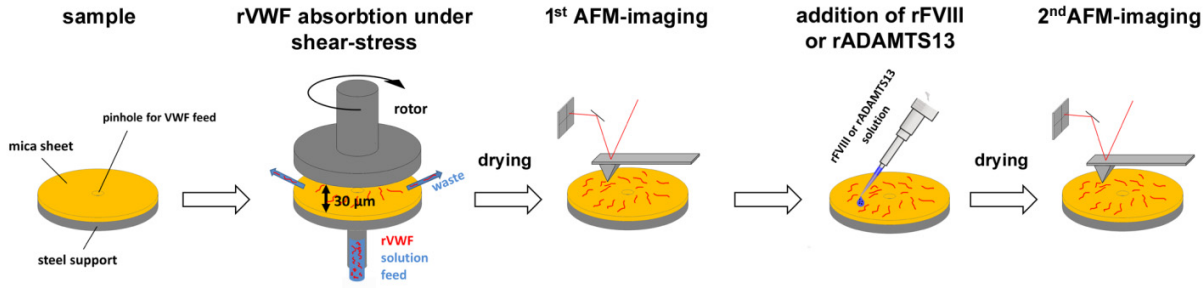


**Figure 11. Experimental scheme.** The VWF solution is pumped into a narrow gap between a mica sheet and a rotating steel plate. Some stretched molecules remain attached to the surface and "frozen" in their elongated conformation which enables subsequent AFM imaging. After addition of either FVIII or ADAMTS13 the same individual molecule is imaged again in order to detect protein binding or proteolysis.

# 8. Aims and Goals of this thesis

This thesis aimed at visualizing the complex formation between von Willebrand factor (VWF) and Factor VIII (FVIII) at single molecule level by atomic force microscopy (AFM). As VWF is a force sensitive molecule, assuming an elongated state under hydrodynamic flow conditions, one mayor goal was to study the FVIII binding affinity of this stretched molecule. Shear-flow induced elongation of VWF, which had previously been studied either theoretically or as a collective phenomenon, was now investigated on a single molecule scale. A further question was the influence of metal ions, especially $Ca^{2+}$, on the 3D conformations of VWF and FVIII and on their specific complex formation.

# 9. Papers

Anal Bioanal Chem (2014) 406:1411–1421
DOI 10.1007/s00216-013-7563-0

RESEARCH PAPER

# Visualization of a protein-protein interaction at a single-molecule level by atomic force microscopy

**Klaus Bonazza · Hanspeter Rottensteiner · Birgit K. Seyfried · Gerald Schrenk · Günter Allmaier · Peter L. Turecek · Gernot Friedbacher**

Received: 30 October 2013 / Revised: 2 December 2013 / Accepted: 6 December 2013 / Published online: 21 December 2013
© Springer-Verlag Berlin Heidelberg 2013

**Abstract** Atomic force microscopy is unmatched in terms of high-resolution imaging under ambient conditions. Over the years, substantial progress has been made using this technique to improve our understanding of biological systems on the nanometer scale, such as visualization of single biomolecules. For monitoring also the interaction between biomolecules, in situ high-speed imaging is making enormous progress. Here, we describe an alternative ex situ imaging method where identical molecules are recorded before and after reaction with a binding partner. Relocation of the identical molecules on the mica surface was thereby achieved by using a nanoscale scratch as marker. The method was successfully applied to study the complex formation between von Willebrand factor (VWF) and factor VIII (FVIII), two essential haemostatic components of human blood. FVIII binding was discernible by an appearance of globular domains appended to the N-terminal large globular domains of VWF. The specificity of the approach could be demonstrated by incubating VWF with FVIII in the presence of a high salt buffer which inhibits the interaction between these two proteins. The results obtained indicate that proteins can maintain their reactivity for subsequent interactions with other molecules when gently immobilized on a solid substrate and subjected to intermittent drying steps. The technique described opens up a new analytical perspective for studying protein-protein interactions as it circumvents some of the obstacles encountered by in situ imaging and other ex situ techniques.

K. Bonazza · G. Allmaier · G. Friedbacher (✉)
Institute of Chemical Technologies and Analytics, Vienna University of Technology, Getreidemarkt 9/164-IAC, 1060 Wien, Austria
e-mail: gernot.friedbacher@tuwien.ac.at

H. Rottensteiner · B. K. Seyfried · G. Schrenk · P. L. Turecek
Baxter Innovations, Industriestraße 67, 1221 Wien, Austria

**Keywords** Atomic force microscopy · Protein morphology · Protein-protein interaction · von Willebrand factor · Factor VIII · Calcium

## Introduction

Almost since its invention, atomic force microscopy (AFM) has been used to study biological systems [1]. First AFM studies of single molecules were carried out on DNA, and also nowadays this biomolecule can still be seen as the benchmark biological sample for improvement of spatial resolution [2, 3]. Although AFM imaging is generally considered as a non-destructive imaging method, delicate samples can still be affected by the tip. Therefore, most studies focusing on the interaction between biomolecules were either limited to the observation of their assembly into larger ordered structures such as monolayers and membranes [4], or recognition imaging has been used for directly assessing binding forces between biomolecules [5], however with limited lateral resolution. Force spectroscopy has been used for instance to study the forces required to unfold a VWF molecule [6].

Recent advances in controlling tip sample forces (peak force tapping, miniaturized cantilevers), often combined with high-speed data collection, have opened up the possibility to observe, e.g., rotation and motion of receptor molecules or molecular motor molecules walking along a filament [7]. Bihan et al. showed telomeric DNA with Rap1 protein attached to it [8]. As the large size of Rap1 made the protein clearly discernible from DNA, monitoring identical DNA molecules before and after reaction with Rap1 was not required. This however appears crucial for studying interactions of biomolecules of similar size. Here, we present such an alternative strategy using complex formation between von Willebrand factor (VWF) and factor VIII (FVIII) as a prototype for a physiologically relevant protein-protein interaction.

VWF and FVIII are two intimately intertwined molecules of human blood that play essential roles in haemostasis [9–12]. In addition, VWF significantly prolongs the half-life time of FVIII by forming a tight non-covalent complex. VWF circulates as multimer of varying size, composed of up to 40 monomeric units with a molecular weight of 256 kDa (for the monomer) [13]. These units are comprised of multiple domains (D′-D3-A1-A2-A3-D4-B-C1-C2-CK) and linked through disulfide bonds [14]. Recombinant VWF (rVWF) as used in the present study has a similar morphology and only a slightly increased overall size distribution compared to plasma-derived VWF [15]. FVIII is a heterodimer consisting of a light chain (domains *a3*-A3-C1-C2) and a heavy chain of variable size (domains A1-*a1*-A2-*a2*-B) held together noncovalently by a metal ion [16]. Due to the heterogeneous nature of the molecule only an average molecular weight of approximately 300 kDa can be assigned to FVIII [17].

Binding of FVIII to VWF occurs with high affinity ($K_D$= 0.2–0.5 nM) [18] and involves multiple sites within the light chain of FVIII [19]. The major VWF binding site is located within the *a3* acidic domain [20], but additional sites within the more C-terminal-located C1 and C2 domains also contribute to high affinity binding [21, 22]. The major if not exclusive binding site for FVIII is located within the first 310 amino acid residues of the mature VWF subunit (D′-D3) [23].

Images of pure VWF were first obtained by electron microscopy [24–26], revealing a morphology for VWF that is characterized by repeating globular structures with interconnecting rod-like regions. This picture was recently significantly refined by Zhou and colleagues who were able to assign specific modules to structures seen in electron micrographs [27]. Various AFM studies on VWF confirmed the basic VWF morphology, but in addition visualized its elongated conformation as occurring under shear stress [15, 28, 29]. The morphology of FVIII has been studied by electron microscopy [30–32] and a crystal structure of a B domain-free variant of FVIII with about 4 Å resolution is available [33].

To follow the reaction between VWF and FVIII on a single-molecule level, we pursued different approaches of AFM imaging. The results obtained indicate that protein binding events can be monitored on a solid substrate, even if intermittent drying steps are included in the procedure. The potential of using this method for studying interactions of biological molecules more generally will be discussed.

## Materials and methods

*Sources of recombinant VWF and FVIII* Recombinant VWF lots used in this study were prepared under identical conditions as described in Seyfried et al. [15]. Full-length rFVIII (ADVATE, Baxter) served as source for FVIII. All AFM studies were conducted with the rVWF lot HN02R00 (101 IU/mL VWF:RCo activity; 87 IU/mL VWF:Ag) and the rFVIII lot LE01L017AA (394 IU/mL FVIII chromogenic activity). For the enzyme-linked immunosorbent assay (ELISA)-based VWF-FVIII interaction assay, the rVWF lot ORVWSEC06003F1WF (16 IU/mL VWF:RCo activity; 14.8 IU/mL VWF:Ag) and the rFVIII lot VNM1K025S1 (374 IU/mL FVIII chromogenic activity) were used.

*Determination of VWF-FVIII complex formation by ELISA* A defined amount of rFVIII (0.2 IU/mL FVIII chromogenic activity) and increasing concentrations of rVWF (0–0.02 IU/mL VWF:Ag) were incubated for 25 min at 37 °C in phosphate-buffered saline (PBS) buffer or, as a negative control, in tris-buffered saline (TBS) buffer containing 150 mM NaCl and 500 mM $CaCl_2$. The buffers additionally contained 0.05 % Tween-20 and 3 % bovine serum albumin to block unspecific binding to the microtiter plate. The VWF-FVIII complex formed was then transferred to a microtiter plate coated with a polyclonal rabbit anti-human VWF antibody (A-0082, DAKO Cytomation, Glostrup, Denmark). Unbound FVIII was removed by a washing step, and bound FVIII was detected by a horseradish peroxidase-labeled antihuman FVIII antibody (Cedarlane Laboratories, Hornby, Ontario, Canada).

*VWF-FVIII complex formation in solution (indirect approach)* Complex formation in solution was performed in PBS buffer or as control in TBS buffer containing 150 mM NaCl and 500 mM $CaCl_2$ for 20 min at 37 ° C using a mixture of 29.6 μg rVWF (molecular weight, 300 kDa) and 5.8 μg rFVIII (molecular weight, 280 kDa) in 900 μL of buffer, achieving a molar ratio of 4.8:1 with respect to the rVWF monomer. Mixing of the solution components was performed by repeated up–down pulling of the solution with a pipette for five times. The formed complex was deposited from solution by pipetting a drop of 200 μL on a freshly cleaved mica sheet with a size of 15×15 $mm^2$ covering the whole area of the sheet. After 5 min of adsorption the solution was rinsed off with ultrapure water (resistance, 0.05 mS/cm) obtained from a Milli-Q apparatus (Millipore, Billerica, MA, USA) and the substrate with the adsorbed complex was blown dry with nitrogen. In some preliminary experiments, the complex was separated from the excess of rFVIII prior to deposition on the mica sheet by centrifugation with microfilter units with a pore size of 0.1 μm (Ultrafree-MC, Millipore), with or without 0.1 % Tween-20 (Sigma Aldrich, Steinheim, Germany). In order to make sure that the observed number of FVIII molecules on the surface is not biased by the position of the AFM measurement, the following experiment has been performed: A solution of FVIII with a fairly high concentration of 0.36 μg/mL (in order to exaggerate a possible artifact) was applied to the mica sheet as described above. Then, 2×2 $\mu m^2$ AFM images were recorded at six different positions ranging from the center of the substrate to a distance of approximately

4 mm from the center. The number of FVIII molecules counted in these images was in a very narrow range of 349 to 384. Given the fact that in our study, the measurement positions were always well within 1 mm from the center of the substrate, artifacts introduced by local changes of the surface coverage can be absolutely excluded.

*VWF-FVIII complex formation on the mica surface (single-molecule approach)* To image identical VWF molecules before and after complex formation with FVIII, a scratch was made on the mica surface with an AFM tip. One end of this scratch was wide enough (approximately 1 μm) to be recognized in a light microscope, whereas the width of the scratch on the opposite end was reduced to nanoscopic sharpness. Then, a 200-μL droplet of a solution containing 0.86 μg/mL VWF was applied on this mica surface. After 5 min, the mica was rinsed with ultrapure water and blown dry with nitrogen. The scratch was then used as a marker to position the AFM tip at a specific sample position for imaging certain VWF molecules. The substrate was removed from the microscope and a droplet of a 0.08 μg/mL FVIII solution in PBS buffer containing 50 mM $MgCl_2$ was applied on the surface. As control, FVIII in TBS buffer containing 150 mM NaCl and 500 mM $CaCl_2$ was applied. The nanometer-width scratch was again used to image the identical VWF molecules after reaction with FVIII. $MgCl_2$ was added to the adsorption solution in these experiments because preliminary experiments have indicated that the adhesion of VWF on mica can be increased by $Mg^{2+}$ ions.

The influence of $Ca^{2+}$ on the morphology of VWF was similarly studied by sequential addition of buffers containing very low (PBS), no (TBS plus 10 mM EDTA), or high (TBS plus 500 mM $Ca^{2+}$) concentrations of calcium.

*AFM measurements* All AFM images where recorded in tapping mode (TM) with a NanoScope V (Bruker, Santa Barbara, CA, USA) using etched single crystal silicon probes (NCH from Nanoworld, Neuchatel, Switzerland) with a spring constant of 42 N/m. Images where taken with setpoints corresponding to a damping of approximately 90 % of the free amplitude.

*Image processing and data analysis* AFM raw images were flattened using the NanoScope Software (Version v7, Bruker, Santa Barbara, CA, USA) or a home-made software [34]. This software was also used for automatic counting of FVIII molecules for some of the images recorded in the "indirect approach".

## Results

*Direct imaging of VWF, FVIII, and VWF-FVIII complexes* AFM images of VWF and FVIII deposited on mica from PBS buffer solution are shown in Fig. 1. The VWF multimers (Fig. 1a) consist of repeating globular units connected by rod-like sections as shown previously [15]. The FVIII molecules exhibit spherical shapes and are of similar size as the globular VWF knots (Fig. 1b). Manual evaluation of 118 VWF knots and 77 FVIII molecules revealed a size distribution for the diameters of the VWF knots between 11 and 32 nm (Fig. 1c) and for the diameters of FVIII between 11 and 34 nm (Fig. 1d), with an average diameter of 18±5 nm for both species.

Next, VWF was mixed with FVIII at a molar ratio of 1:10 (8 ng VWF: 73 ng FVIII in 900 μL PBS buffer) with respect to the VWF monomer and the complexes formed were deposited on mica from PBS buffer solution. Corresponding AFM images showed some vague evidence for complex formation; however, these experiments were not entirely conclusive due to the similar size of the VWF knots and the FVIII molecules as well as the presence of an excess of FVIII molecules that had not bound to VWF (data not shown). In order to improve the interpretability of the images the excess of free FVIII was separated from the complex through microfiltration in the presence of a nonionic surfactant (Tween-20) prior to deposition on mica. This purification step allowed the effective removal of unbound FVIII, but the uncertainty in distinguishing free VWF knots from FVIII-bound VWF knots still remained (data not shown). Therefore, two other concepts, which are described in the following, were pursued.

*Indirect quantification of complex formation between FVIII and VWF* Due to the difficulties in distinguishing FVIII from the globular VWF units an indirect approach for the evaluation of complex formation was pursued. FVIII was incubated with or without VWF, deposited on mica, and complex formation was monitored by quantification of the FVIII molecules that had not bound to VWF. In order to see if concentrations of FVIII in solution can be derived from the surface coverage obtained from AFM images, the concentration of free FVIII molecules per unit area (= areal number concentration) was determined for different concentrations of FVIII. Two AFM images of 5×5 $\mu m^2$ were evaluated for each sample using a custom-made software [34]. A linear relation was observed (Fig. 2a), demonstrating the feasibility of the approach.

VWF-FVIII complex formation was studied with 29.6 μg VWF and 5.8 μg FVIII in 900 μL PBS buffer (molar ratio of 4.8:1 with respect to the VWF monomer). The number of FVIII molecules present on the surface was determined in two independent experiments to be 366 (average of 375 and 357 for the two individual experiments) when FVIII was adsorbed on mica from a pure FVIII solution (i.e., lacking VWF; Fig. 2b). In the presence of VWF, the number of free FVIII molecules was reduced to 151 (average of 158 and 143; Fig. 2c) indicating that the remaining 215 molecules (59 %) had interacted with VWF.

To confirm that the observed loss of FVIII was caused by a specific binding to VWF, VWF and FVIII were mixed in a

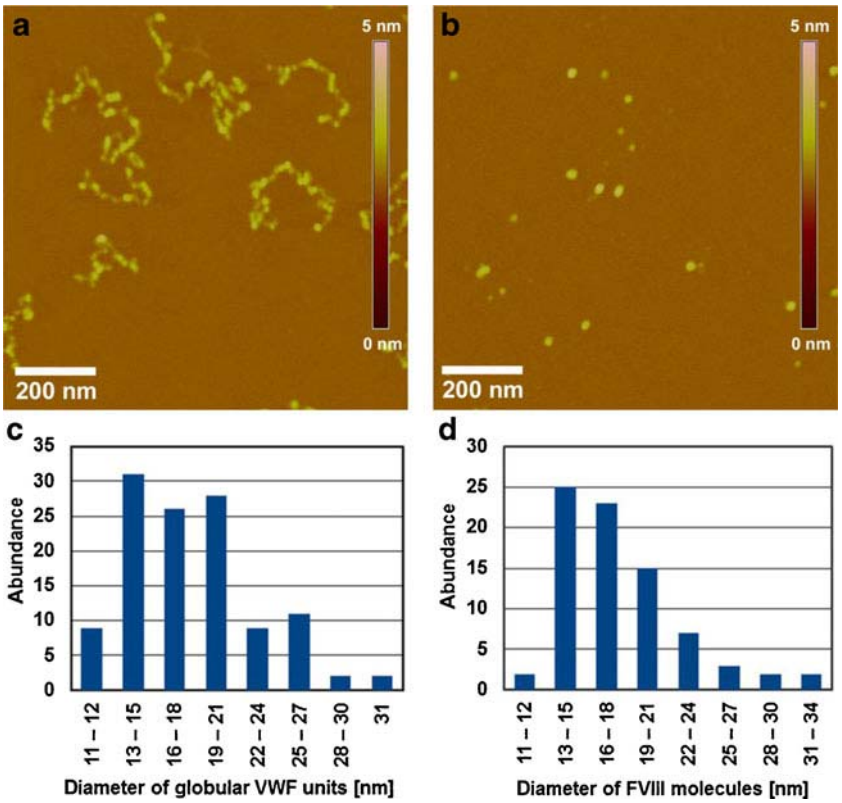


**Fig. 1** TM-AFM images of **a** VWF and **b** FVIII on mica. **a** The VWF molecules consist of globular units and rod-like sections. In the stretched regions of the molecule, the globular units are slightly smaller. Image size, $1 \times 1\ \mu m^2$; height scale, 5 nm from *dark* to *bright*. **c**, **d** Size distributions of **c** globular VWF units as derived from the TM-AFM images by manual evaluation of 118 VWF units and **d** FVIII as derived from the TM-AFM images by manual evaluation of 77 FVIII molecules. The average diameter of both species is 18±5 nm

buffer system of high ionic strength (TBS with 150 mM NaCl and 500 mM $CaCl_2$). In contrast to PBS buffer, this buffer inhibited complex formation as confirmed by an ELISA-based interaction assay (Fig. 2e) in line with a previous report [35]. The number of free FVIII molecules in the respective AFM image was also significantly higher in the presence of the inhibitory buffer (383 (average of 394 and 372); Fig. 2d) indicative for a reduced binding of FVIII to VWF. Since this number is similar to that obtained for the sample lacking VWF (366), we conclude that complex formation is totally inhibited under this condition (Fig. 2f).

*Direct imaging of identical VWF molecules before and after complex formation with FVIII (single-molecule approach)* As outlined above, binding of FVIII molecules to VWF can hardly be monitored by AFM if different individual molecules are compared before and after complex formation. Therefore, a method to trace changes in an individual identical VWF molecule before and after incubation with FVIII was developed. The key to relocate an individual molecule after temporary removal of the mica from the microscope was a scratch that could be used as a marker to position the AFM tip to the same sample spot again. Such a nanosized (in width) scratch (indicated by an arrow) in an AFM image of VWF molecules adsorbed on mica from PBS solution is shown in Fig. 3a. Magnified images of the boxed VWF molecule near the scratch before (Fig. 3b) and after (Fig. 3c) treatment of the surface with PBS buffer for 5 min showed that this molecule largely kept its position and structure; the slight changes visible were likely due to a restricted mobility of VWF while in contact with the solution. Importantly, changes of globular structures which could mimic an association with FVIII were not discernible after buffer treatment of VWF. This was verified evaluating 18 molecules consisting of a total of 361 knots derived from two independent experiments. In order to show this on a more quantitative basis, cross-sectional profiles through individual knots have been prepared. Figure 4 shows the heights of these knots determined from these cross-sectional profiles before and after treatment with PBS buffer. Significant changes of the height of the knots cannot be observed.

Next, AFM images of VWF before and after incubation with FVIII were recorded. After addition of FVIII, globular structures which are clearly increased in size and height could be observed (Fig. 5a, b). Therefore, they were interpreted as FVIII molecules attached to VWF. Altogether, 17 such structural features can be seen in Fig. 5b. In order to guide the eye of the reader, they are marked with an arrow and "C" (C stands for complex). A few globular units in Fig. 5b could not be assigned unequivocally to FVIII molecules (labeled with a question mark). Those structures likely were formed due to rearrangement of VWF when in contact with the FVIII solution. In order to show the differences between reacted and unreacted sites on a more quantitative basis again, cross-

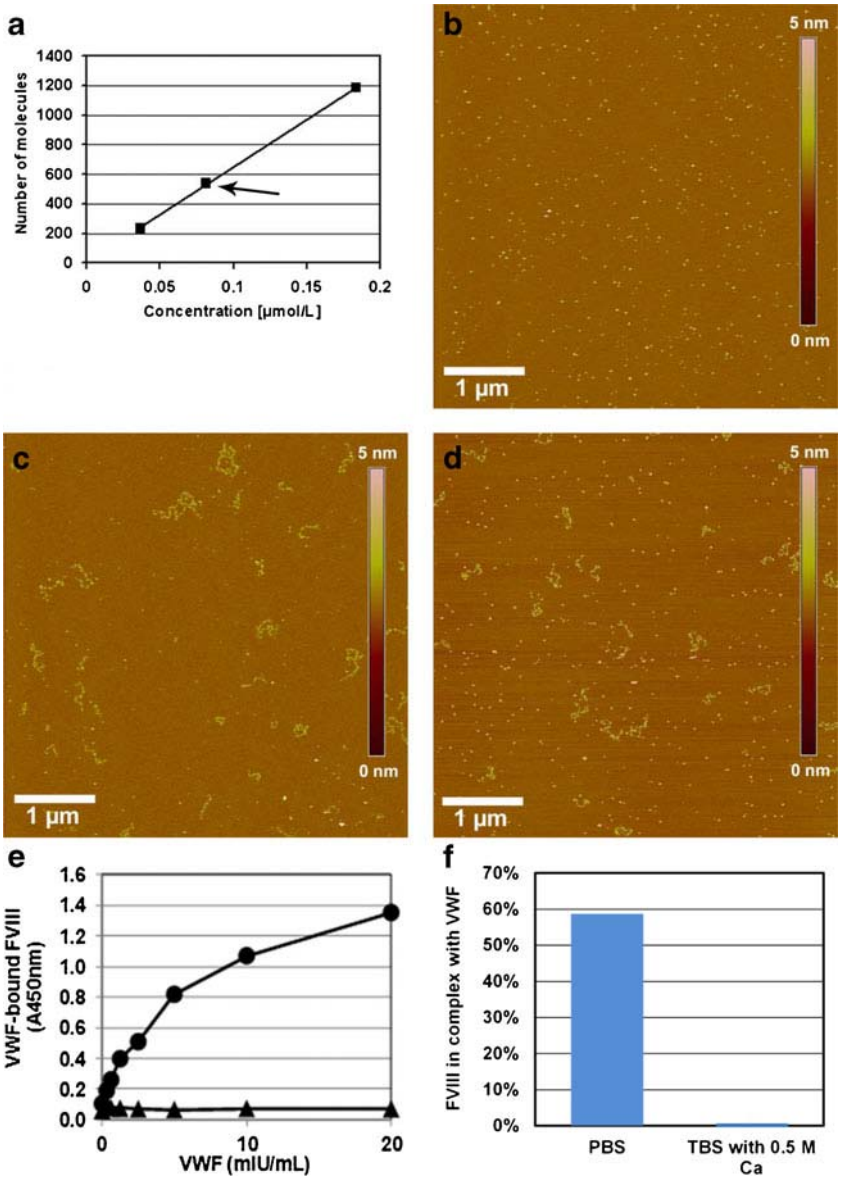


**Fig. 2** Indirect measurement of the binding of FVIII to VWF ("indirect approach"). **a** Number of free FVIII molecules on an imaged mica surface of 5×5 $\mu m^2$ versus its concentration in the deposition solution. The *arrow* indicates the FVIII concentration that had been used for the experiments in **b**–**d** (80 µg/L). The *numbers* shown in the diagram are mean values from two independent measurements (images). The range of scattering is typically 20 molecules. TM-AFM images of **b** pure FVIII adsorbed on mica from PBS buffer, **c** FVIII and VWF adsorbed on mica from PBS buffer, and **d** FVIII and VWF adsorbed on mica from TBS buffer containing 150 mM NaCl and 500 mM $CaCl_2$ (inhibiting conditions). Note that the number of free FVIII molecules is obviously lower in **c** compared to **b** and **d**. Image size, 5×5 $\mu m^2$; height scale, 5 nm from *dark* to *bright*. **e** Detection of VWF-FVIII complex formation by ELISA. FVIII (20 mIU/mL) was incubated with increasing concentrations of VWF (0–20 mIU/mL) in PBS buffer (*circles*) and TBS buffer containing 150 mM NaCl and 500 mM $CaCl_2$ (*triangles*). The amount of VWF-bound FVIII is expressed as absorbance at a wavelength of 450 nm. **f** Summary of the quantitative evaluation of the TM-AFM images shown in **b**–**d**. The numbers are fractions (with respect to the total number introduced to the reaction solution) of FVIII molecules which have reacted with VWF. This fraction has been obtained via determination of the concentration of the free unreacted FVIII from TM-AFM images based on the relation shown in **a**. Binding of VWF and FVIII was observed in PBS whereas it was totally inhibited by increasing the $Ca^{2+}$ concentration. The results are based on mean values from two independent measurements

sectional profiles through individual knots have been prepared. Figure 5c, d show as an example 3 profiles before (Fig. 5c) and after (Fig. 5d) reaction with FVIII. It can be seen that the knots change their heights from typically less than 2 nm to more than 3 up to 4 nm upon reaction with FVIII. In a similar manner, 44 knots were evaluated. Figure 6 shows the heights of these knots before and after reaction with FVIII. Seventeen knots have changed their height from typically 1.5 nm to more than 3 up to 4 nm (green bars). For 23 knots, the heights did not change significantly (red bars). Four knots cannot be assigned unequivocally (yellow bars). This is significantly different from the blind test (treatment with PBS

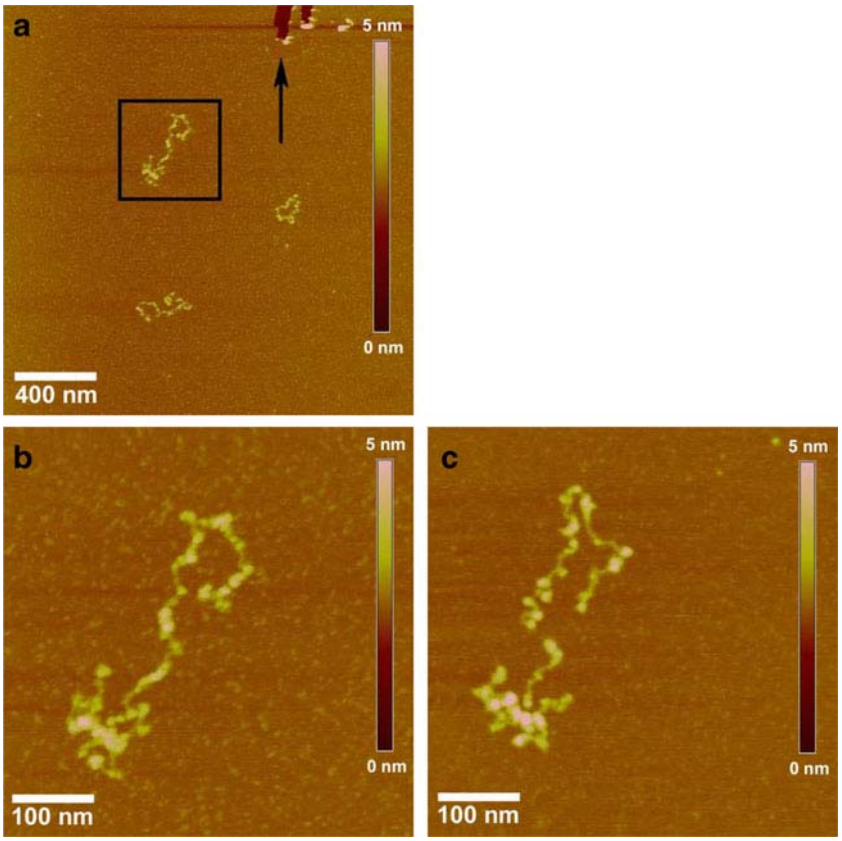


**Fig. 3** TM-AFM images of **a** VWF molecules on mica located adjacent to a nanoscopic scratch mark (the very end of the scratch is marked with an *arrow*). **b** Zoom of the molecule marked in **a**, and **c** the same molecule as in **b** after treatment of the surface with a drop of PBS buffer solution for 5 min. Image size, 2×2 $\mu m^2$ (**a**); 500×500 $nm^2$ (**b**, **c**); height scale, 5 nm from *dark* to *bright*

buffer only) where such changes of the height of the knots cannot be observed (see Fig. 4). Considering only the globular structures which can be unequivocally assigned to attached FVIII molecules, evaluation of a total number of 25 VWF molecules from three independent experiments consisting of a total of 522 globular units (the average number of such units per molecule was approximately 21) revealed that an average number of 5 FVIII molecules were attached to one VWF molecule, thereby occupying 25±4 % of the globular monomeric units of VWF.

It should be emphasized that the average number of FVIII molecules deposited on the same surface area (300×300 $nm^2$) of pure mica (without VWF molecules) is only 2, supporting the hypothesis that the changes described above are indeed due to specific complex formation between FVIII and VWF. Even assuming a random adsorption of 10 FVIII molecules within the considered surface area the probability that at least three of them would randomly rest on a VWF molecule is only 0.3 %. This result is based on a binomial distribution assuming a probability of 3 % (this is the area

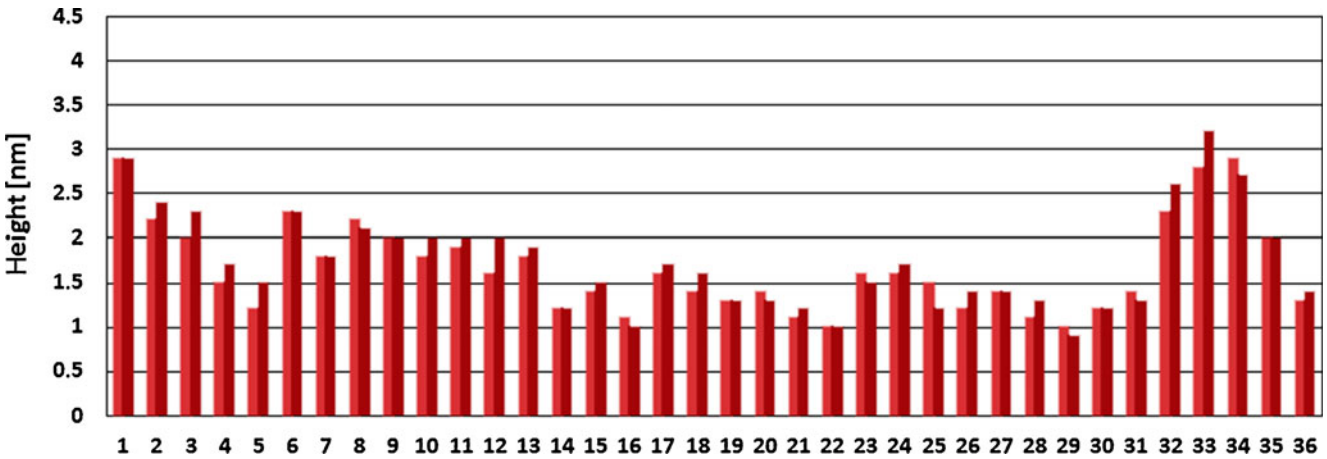


**Fig. 4** Evaluation of heights from 36 cross-sectional profiles through individual VWF knots of the molecule shown in Fig. 3 before (*bright*) and after (*dark*) treatment with PBS buffer (blind test)

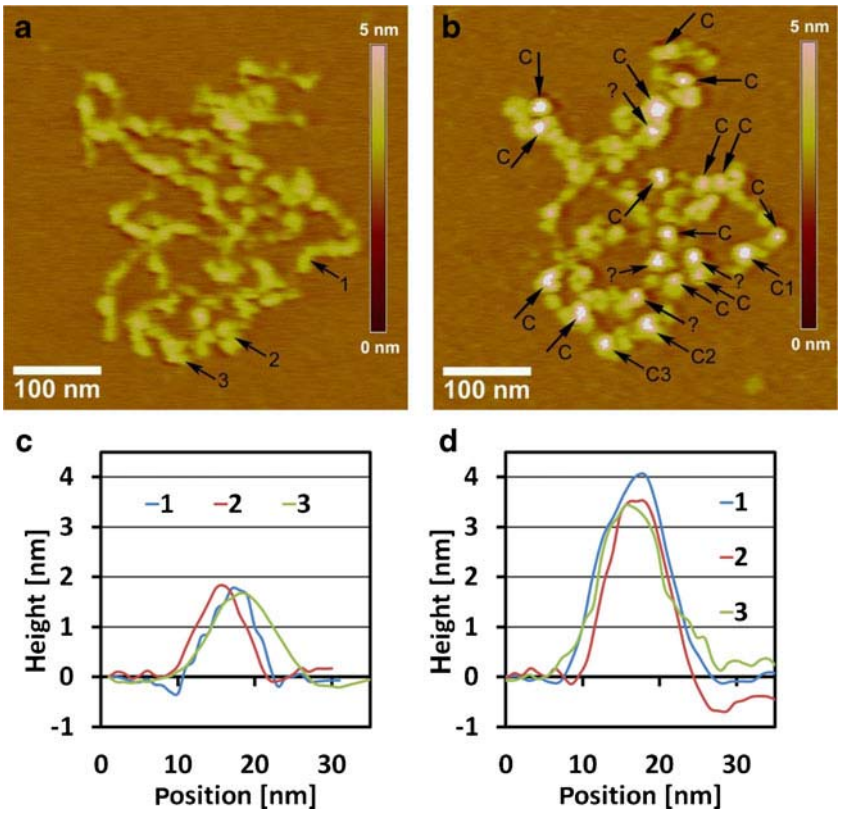


**Fig. 5** Direct demonstration of FVIII binding to VWF (single-molecule approach). Shown are TM-AFM images of the same VWF molecule **a** before and **b** after complex formation with FVIII in the presence of PBS buffer. Bound FVIII molecules are clearly visible as brighter spots (marked with a *C* and an *arrow*). Four dots cannot be assigned unequivocally to attached FVIII (marked with a *question mark* and an *arrow*). Image size, 460×460 nm$^2$; height scale, 5 nm from *dark* to *bright*. **c**, **d** Cross-sectional profiles through three selected knots marked in **a** and **b**, respectively

fraction covered by VWF in the AFM images) for randomly hitting a VWF molecule with a FVIII molecule. In fact, the evaluated VWF molecules showed an average of five FVIII molecules attached, further confirming that random attachment during the adsorption process to achieve such a result is extremely unlikely.

The specificity of the observed interaction was again confirmed by inhibiting FVIII binding to VWF in the presence of a buffer with high ionic strength. Two single VWF molecules adsorbed on mica before and after incubation with FVIII in a buffer with a high $CaCl_2$ concentration are shown in Fig. 7. Although, in this case, two fairly large VWF molecules together consisting of 51 globular units were analyzed, none of these globular domains have significantly changed their morphology upon incubation with FVIII. This was again confirmed by evaluation of the heights through cross-sectional profiles (Fig. 8). Evaluation of 17 molecules from three independent experiments consisting of a total number of 280 globular units revealed that FVIII molecules were attached to less than 2±1 % of the globular monomeric units of VWF (compared to 25±4 %

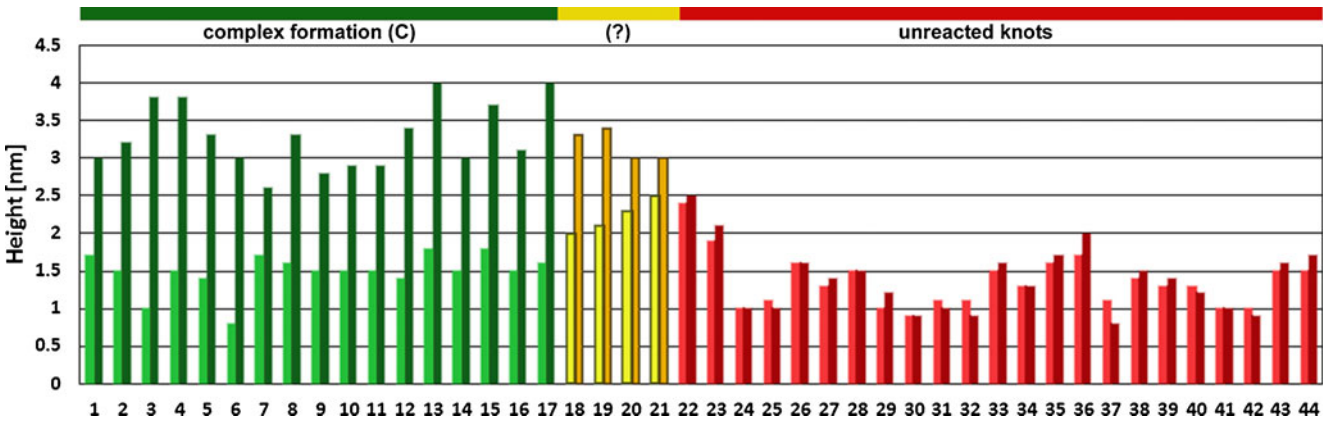


**Fig. 6** Evaluation of heights from 44 cross-sectional profiles through individual VWF knots of the molecule shown in Fig. 5 before (*bright*) and after (*dark*) interaction with FVIII. Knots which changed their height upon reaction with FVIII are marked in *green color*. Knots which have not reacted are marked in *red*. Knots which cannot be assigned unequivocally are shown in *yellow*

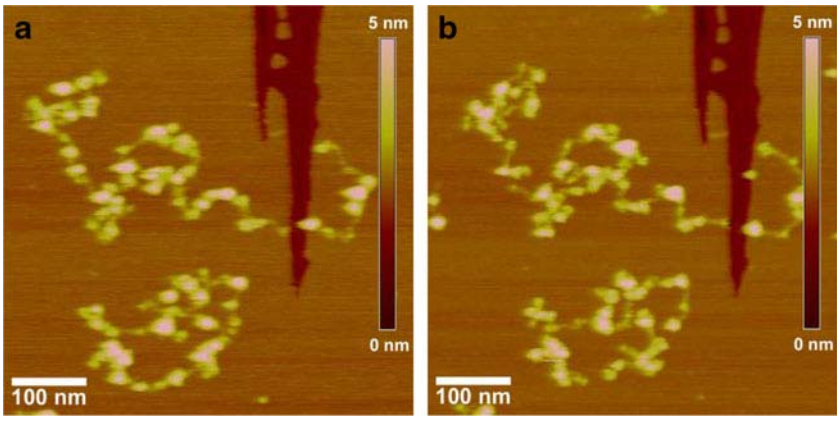


**Fig. 7** Single-molecule approach under inhibiting conditions. Shown are TM-AFM images of the same VWF molecule **a** before and **b** after treatment with FVIII in the presence of TBS buffer containing 500 mM $CaCl_2$. Substantial changes indicative for bound FVIII molecules are not visible. Image size, 550 × 550 $nm^2$; height scale, 5 nm from *dark* to *bright*

in case of a buffer without $Ca^{2+}$). A summary of all data obtained with the single-molecule approach is shown in Fig. 9, clearly demonstrating that VWF-FVIII complex formation could be visualized by AFM.

*$Ca^{2+}$-dependent morphology* Notably, the morphologies of the VWF molecules shown in Figs. 5a and 7a significantly differed, with VWF multimers adsorbed from the $Ca^{2+}$-rich buffer showing larger knots and thinner and longer rod-like interconnections. The influence of $Ca^{2+}$ on the morphology of VWF was therefore studied directly by first adsorbing VWF from PBS buffer (Fig. 10a), then exposing the identical molecules to TBS buffer containing 10 mM EDTA ($Ca^{2+}$ free; Fig. 10b), and finally treating the VWF multimers with the same $Ca^{2+}$-rich TBS buffer as used in Fig. 7 for blocking the binding of FVIII to VWF (Fig. 10c). Evidently, in the presence of calcium, the knots had a higher tendency to constrict thereby adopting a tighter and more globular structure.

## Discussion

The similar dimensions and shapes of FVIII and the globular domain of VWF made the analysis of VWF-FVIII complexes challenging. Deposition of such complexes on the mica surface from solution revealed structures suggestive of complex formation but did not allow an unequivocal assignment of FVIII molecules that had associated with VWF. Furthermore, a background of free FVIII molecules that had not bound to VWF was discernible. Nonetheless, by counting the number of free FVIII molecules in the presence or absence of VWF, binding of FVIII to VWF could be estimated indirectly. The specificity of this approach was shown by a negative control, as complex formation could be inhibited in the presence of a buffer with a high calcium concentration (Fig. 2).

A new strategy was presented to follow the binding reaction on the single molecule level (i.e., single-molecule approach): The same immobilized VWF molecule was imaged before and after complex formation with FVIII. A FVIII binding event was recorded when the height and size of a VWF globular domain was substantially increased. Notably, no FVIII binding to rod-like sections of VWF was observed. This is in agreement with the major FVIII binding site being located in the N-terminal D′-D3 domain of VWF [23, 36–38]. The residual flexibility of the VWF molecule was determined by treating VWF with buffer instead of FVIII (Fig. 3). Overall, the geometry of the VWF molecules on the mica surface was stable but slightly changed in some regions leading to new globular knots which may not be distinguished unequivocally

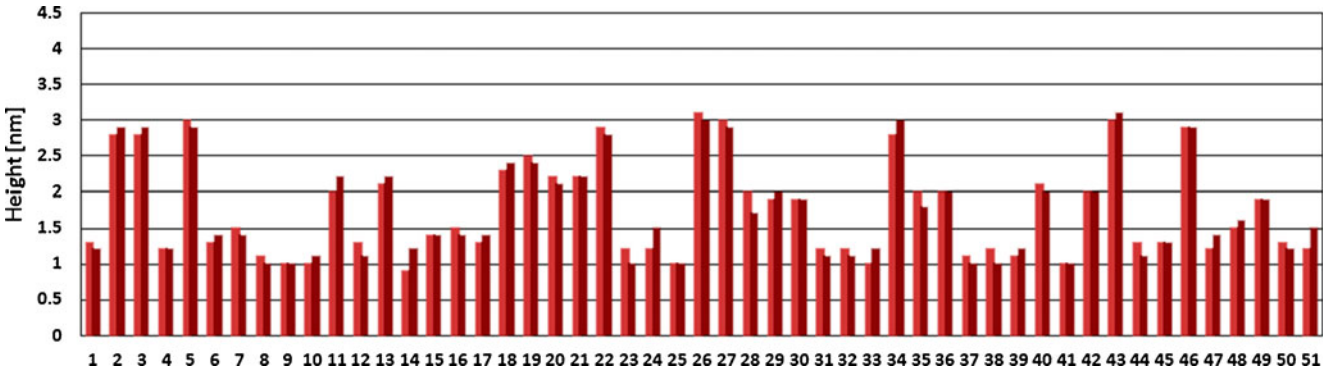


**Fig. 8** Evaluation of heights from 51 cross-sectional profiles through individual VWF knots of the molecule shown in Fig. 7 before (*bright*) and after (*dark*) treatment with FVIII under inhibiting conditions ($Ca^{2+}$)

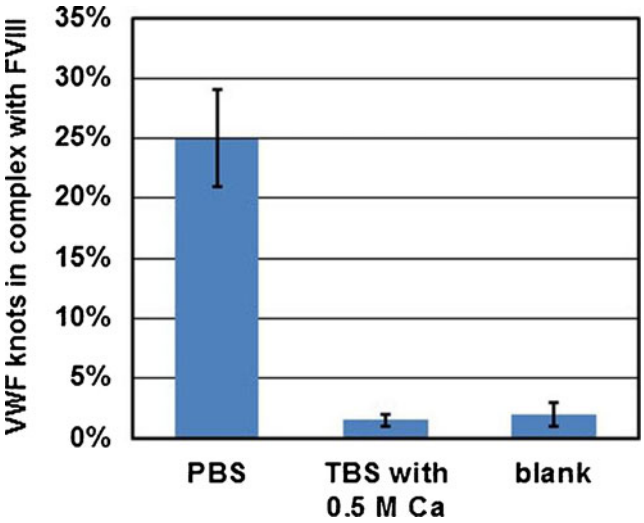


**Fig. 9** Summary of the single-molecule approach results. Shown is the fraction of VWF globular units that exhibited changes due to attachment of FVIII molecules under different experimental conditions. In contrast to the numbers given in Fig. 2e, the percentages in this diagram have been determined by directly imaging identical VWF molecules before and after exposure to FVIII on the mica surface. Binding of FVIII to VWF was observed in PBS buffer whereas it was almost totally inhibited in a high ionic strength buffer. Blank denotes a control experiment performed with PBS buffer in the absence of FVIII

from attached FVIII molecules. This fraction which accounted for approximately 2 % of all VWF knots was considered when images were quantified. The fraction of VWF knots that had bound FVIII was 25±4 % and declined to 2±1 %, when complex formation was performed in the presence of a high salt buffer containing 500 mM $Ca^{2+}$.

It should be pointed out that VWF molecules showed significantly different morphologies depending on the presence of calcium in the buffer. Since a high $Ca^{2+}$ concentration gave rise to increased knot sizes (Fig. 10), the morphology of the VWF molecule shown in the control experiment (high calcium concentration) before FVIII exposure (Fig. 7a) somewhat mimicked the morphology of VWF when complexed with FVIII (Fig. 5b). Therefore, to avoid misinterpretation of data with regard to complex formation, only molecules that have been exposed to the same buffer should be compared. The $Ca^{2+}$-dependent structural change can probably be explained by the shielding of repulsive negative charges, which causes a tighter coiled structure. Although one may dispute the physiological relevance of a VWF morphology in the presence of 500 mM $Ca^{2+}$ (in fact it has been used to interfere with FVIII binding), it is worth noting that the conformation of the VWF A2 domain has recently been demonstrated to be stabilized and protected from premature unfolding (and exerts a restoring force on the elongated conformation) by physiological $Ca^{2+}$ concentrations [39].

The half-life time of FVIII is critically dependent on its ability to form a complex with VWF in the blood circulation

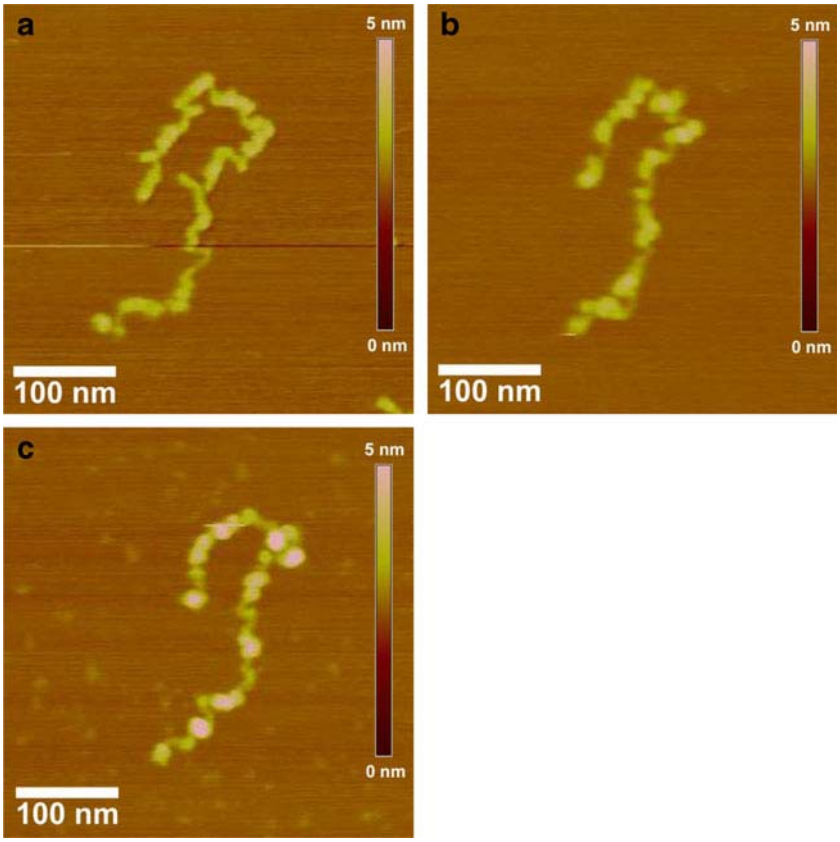


**Fig. 10** Calcium dependence of VWF morphology. TM-AFM images of identical VWF molecules **a** adsorbed from a PBS buffer solution (almost $Ca^{2+}$ free), **b** after subsequent exposure to TBS buffer containing EDTA ($Ca^{2+}$ free), and **c** after addition of 500 mM $CaCl_2$. A significant increase in knot size was discernible in the presence of a high $Ca^{2+}$ concentration. Image size, 400×400 $nm^2$; height scale, 5 nm from *dark* to *bright*

system, yet the actual binding capacity of VWF for FVIII is still not known. In plasma, a ratio of 1 molecule FVIII to 50 monomers of VWF seems to be maintained [11, 40]. Likewise, ELISA-based in vitro studies employing VWF immobilized on a polymer surface have revealed similar stoichiometries of 1:50 to 1:100. On the other hand, when complex formation was analyzed in solution using, for instance, gel filtration chromatography, stoichiometries close to 1:1 were obtained [18]. In our setup, the FVIII binding capacity of VWF despite being immobilized reached a FVIII:VWF monomer ratio of 1:4. This ratio was significantly higher than that obtained with ELISA-based assays even though the VWF molecules were also adsorbed on a surface. This might be due to the hydrophilic nature of the mica substrate surface where VWF molecules retained some flexibility, thereby exposing more FVIII binding sites. Our data thus seem to support a binding capacity of VWF to FVIII that is higher than the physiological VWF:FVIII ratio in plasma might predict. Notably, however, our single-molecule approach led to a substantial shift of the molar concentration ratio towards FVIII, because a fixed limited number of VWF molecules on the surface were faced with a large excess of FVIII molecules in the solution on top of the mica surface.

## Conclusion

Pursuing different approaches of AFM imaging, we were able to follow up the reaction between VWF and FVIII on the single-molecule level. Although attachment of biomolecules to a surface may change their properties, our results show that reactions of such molecules with binding partners can still be monitored by imaging them on a solid substrate, even if intermittent drying steps are included in the procedure. The data open up the perspective for studying a variety of biological molecules and systems. Furthermore, the results show that TM-AFM imaging can significantly contribute to the understanding of the interaction between VWF and FVIII supplementing the results of other well-established non-imaging techniques such as ELISA-based interaction assays, gel filtration, and ultracentrifugation [40].

**Acknowledgments** We thank Manfred Billwein (Baxter Bioscience) for performing the ELISA assay.

## References

1. Hansma P, Elings V, Marti O, Bracker C (1988) Scanning tunneling microscopy and atomic force microscopy: application to biology and technology. Science 242:209–216
2. Ido S, Kimura K, Oyabu N, Kobayashi K, Tsukada M, Matsushige K, Yamada H (2013) Beyond the helix pitch: direct visualization of native DNA in aqueous solution. ACS Nano 7:1817–1822
3. Leung C, Bestembayeva A, Thorogate R, Stinson J, Pyne A, Marcovich C, Yang J, Drechsler U, Despont M, Jankowski T (2012) Atomic force microscopy with nanoscale cantilevers resolves different structural conformations of the DNA double helix. Nano letters 12:3846–3850
4. Müller DJ, Janovjak H, Lehto T, Kuerschner L, Anderson K (2002) Observing structure, function and assembly of single proteins by AFM. Prog Biophys Mol Biol 79:1–43
5. Kienberger F, Ebner A, Gruber HJ, Hinterdorfer P (2006) Molecular recognition imaging and force spectroscopy of single biomolecules. Acc Chem Res 39:29–36
6. Wu T, Lin J, Cruz MA, Dong J-F, Zhu C (2010) Force-induced cleavage of single VWFA1A2A3 tridomains by ADAMTS-13. Blood 114:370–378
7. Katan AJ, Dekker C (2011) High-speed AFM reveals the dynamics of single biomolecules at the nanometer scale. Cell 147:979–982
8. Le Bihan Y-V, Matot B, Pietrement O, Giraud-Panis M-J, Gasparini S, Le Cam E, Gilson E, Sclavi B, Miron S, Le Du M-H (2013) Effect of Rap1 binding on DNA distortion and potassium permanganate hypersensitivity. Acta Crystallogr Sect D: Biol Crystallogr 69:409–419
9. Sadler JE (1991) von Willebrand factor. J Biol Chem 266:22777–22780
10. Terraube V, O'Donnell J, Jenkins P (2010) Factor VIII and von Willebrand factor interaction: biological, clinical and therapeutic importance. Haemophilia 16:3–13
11. Weiss HJ (1991) von Willebrand factor and platelet function. Ann N Y Acad Sci 614:125–137
12. Sakariassen KS, Nievelstein PFEM, Coller BS, Sixma JJ (1986) The role of platelet membrane glycoproteins Ib and IIb-IIIa in platelet adherence to human artery subendothelium. Br J Haematol 63:681–691
13. Kemptner J, Marchetti-Deschmann M, Müller R, Ivens A, Turecek P, Schwarz H-P, Allmaier G (2010) A comparison of nano electrospray gas-phase electrophoretic mobility macromolecular analysis and matrix-assisted laser desorption ionization linear time-of-flight mass spectrometry for the characterization of the recombinant coagulation glycoprotein von Willebrand factor. Rapid Commun Mass Spectrom 24:761–767
14. Sadler J (1998) Biochemistry and genetics of von Willebrand factor. Annu Rev Biochem 67:395–424
15. Seyfried BK, Friedbacher G, Rottensteiner H, Schwarz HP, Ehrlich H, Allmaier G, Turecek PL (2010) Comparison of plasma-derived and recombinant von Willebrand factor by atomic force microscopy. J Thromb Haemost 104:523–530
16. Lenting PJ, Van Mourik JA, Mertens K (1998) The life cycle of coagulation factor VIII in view of its structure and function. Blood 92:3983–3996
17. Eaton D, Hass P, Riddle L, Mather J, Wiebe M, Gregory T, Vehar G (1987) Characterization of recombinant human factor VIII. J Biol Chem 262:3285–3290
18. Vlot A, Koppelman S, van den Berg M, Bouma B, Sixma J (1995) The affinity and stoichiometry of binding of human factor VIII to von Willebrand factor. Blood 85:3150–3157
19. Hamer R, Koedam J, Beeser-Visser N, Bertina R, Van Mourik J, Sixma J (1987) Factor VIII binds to von Willebrand factor via its Mr-80,000 light chain. Eur J Biochem 166:37–43
20. Leyte A, van Schijndel H, Niehrs C, Huttner W, Verbeet M, Mertens K, van Mourik J (1991) Sulfation of Tyr1680 of human blood coagulation factor VIII is essential for the interaction of factor VIII with von Willebrand factor. J Biol Chem 266:740–746
21. Saenko E, Shima M, Rajalakshmi K, Scandella D (1994) A role for the C2 domain of factor VIII in binding to von Willebrand factor. J Biol Chem 269:11601–11605
22. Jaquemin M, Lavend'homme R, Benhida A (2000) A novel cause of mild/moderate haemophilia A: mutations acattered in the factor VIII C1 domain reduce factor VIII binding von Willebrand factor. Blood 96:968–975

23. Bahou W, Ginsburg D, Sikkink R, Litwiller R, Fass D (1989) A monoclonal antibody to von Willebrand factor (vWF) inhibits factor VIII binding. Localization of its antigenic determinant to a nonadecapeptide at the amino terminus of the mature vWF polypeptide. J Clin Investig 84:56–61
24. Ohmori K, Fretto L, Harrison R, Switzer M, Erickson H, McKee P (1982) Electron microscopy of human factor VIII/von Willebrand glycoprotein: effect of reducing reagents on structure and function. J Cell Biol 95:632–640
25. Fretto L, Fowler W, McCaslin D, Erickson H, McKee P (1986) Substructure of human von Willebrand factor. Proteolysis by V8 and characterization of two functional domains. J Biol Chem 261: 15679–15689
26. Fowler W, Fretto L, Hamilton K, Erickson H, McKee P (1985) Substructure of human von Willebrand factor. J Clin Investig 76: 1491–1500
27. Zhou Y, Eng E, Zhu J, Lu C, Walz T, Springer T (2012) Sequence and structure relationships within von Willebrand factor. Blood 120:449–458
28. Marchant RE, Lea AS, Andrade JD, Bockenstedt P (1992) Interactions of von Willebrand factor on mica studied by atomic force microscopy. J Colloid Interface Sci 148:261–272
29. Raghavachari M, Tsai H-M, Kottke-Marchant K, Marchant RE (2000) Surface dependent structures of von Willebrand factor observed by AFM under aqueous conditions. Colloids Surf B: Biointerfaces 19:315–324
30. Fowler WE, Fay PJ, Arvan DS, Marder VJ (1990) Electron microscopy of human factor V and factor VIII: correlation of morphology with domain structure and localization of factor V activation fragments. Proc Natl Acad Sci 87:7648–7652
31. Mosesson MW, Fass DN, Lollar P, DiOrio JP, Parker CG, Knutson GJ, Hainfeld JF, Wall JS (1990) Structural model of porcine factor VIII and factor VIIIa molecules based on scanning transmission electron microscope (STEM) images and STEM mass analysis. J Clin Investig 85:1983–1990
32. Parmenter C, Cane M, Zhang R, Stoilova-McPhie S (2008) Cryo-electron microscopy of coagulation factor VIII bound to lipid nanotubes. Biochem Biophys Res Commun 366:288–293
33. Shen B, Spiegel P, Chang C, Huh J, Lee J, Kim J, Kim Y, Stoddard B (2008) The tertiary structure and domain organization of coagulation factor VIII. Blood 111:1240–1247
34. Müller C (2003) Digital processing and evaluation of AFM images. Master thesis. Vienna University of Technology, Vienna, Austria
35. Owen W, Wagner R (1972) Antihemophilic factor: separation of an active fragment following dissociation by salts or detergents. Thrombosis et Diathesis Haemorrhagica 27:502–515
36. Castro-Nunez L, Bloem E, Boon-Spijker M, van der Zwaan C, van den Biggelaar M, Mertens K, Meijer A (2013) Distinct roles of Ser764 and Lys773 at the N-terminus of von Willebrand factor for complex assembly with coagulation factor VIII. J Biol Chem 288: 393–400
37. Foster P, Fulcher C, Marti T, Titani K, Zimmerman T (1987) A major factor VIII binding domain resides within the amino-terminal 272 amino acid residues of von Willebrand factor. J Biol Chem 262: 8443–8446
38. Takahashi Y, Kalafatis M, Girma J, Sewerin K, Andersson L, Meyer D (1987) Localization of a factor VIII binding domain on a 34 kilodalton fragment of the N-terminal portion of von Willebrand factor. Blood 70:1679–1682
39. Jakobi AJ, Mashaghi A, Tans SJ, Huizinga EG (2011) Calcium modulates force sensing by the von Willebrand factor A2 domain. Nat Commun 2:385–394
40. Vlot A, Koppelman S, Bouma B, Sixma J (1998) Factor VIII and von Willebrand factor. J Thromb Haemost 79:456–465

analytical chemistry

Article

pubs.acs.org/ac

# Shear-Dependent Interactions of von Willebrand Factor with Factor VIII and Protease ADAMTS 13 Demonstrated at a Single Molecule Level by Atomic Force Microscopy

Klaus Bonazza,[†] Hanspeter Rottensteiner,[‡] Gerald Schrenk,[‡] Johannes Frank,[§] Günter Allmaier,[†] Peter L. Turecek,[‡] Friedrich Scheiflinger,[‡] and Gernot Friedbacher*,[†]

[†]Institute of Chemical Technologies and Analytics, Vienna University of Technology, Getreidemarkt 9/164, A-1060 Vienna, Austria

[‡]Baxalta Innovations, Industriestrasse 67, A-1221 Vienna, Austria

[§]Central Machine Shop of the Faculty Technical Chemistry, Vienna University of Technology, Getreidemarkt 9/174, A-1060 Vienna, Austria

*Supporting Information*

**ABSTRACT:** Vital functions of mammals are only possible due to the behavior of blood to coagulate most efficiently in vessels with particularly high wall shear rates. This is caused by the functional changes of the von Willebrand Factor (VWF), which mediates coagulation of blood platelets (primary hemostasis) especially when it is stretched under shear stress. Our data show that shear stretching also affects other functions of VWF: Using a customized device to simulate shear conditions and to conserve the VWF molecules in their unstable, elongated conformation, we visualize at single molecule level by AFM that VWF is preferentially cleaved by the protease ADAMTS13 at higher shear rates. In contrast to this high shear-rate-selective behavior, VWF binds FVIII more effectively only below a critical shear rate of ~30.000 $s^{-1}$, indicating that under harsh shear conditions FVIII is released from its carrier protein. This may be required to facilitate delivery of FVIII locally to promote secondary hemostasis.

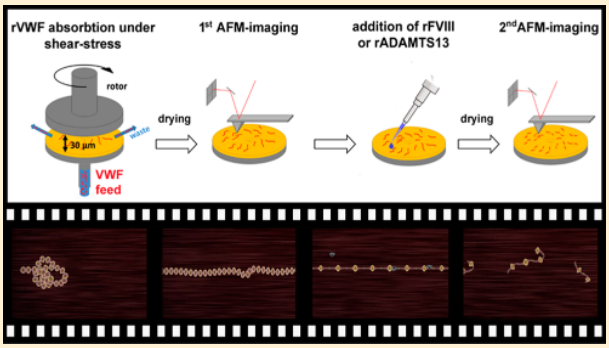


Blood coagulation is a vitally important, highly efficient, and a precisely controlled as well as very selective repair mechanism. There is an enormous variety of diseases associated with bleeding disorders, and hence a lot of research is performed in this field. However, the macromolecular basis of blood coagulation is still not fully understood. Von Willebrand Factor (VWF) is a large glycoprotein which is essential in blood coagulation and has also been found to play multiple roles in inflammation, apoptosis, cancer propagation, and other physiological and pathological processes.[1] From a hemostasis point of view, on the one hand VWF mediates adhesion of platelets to injured endothelial cells, facilitating platelet recruitment especially at high wall shear stress,[2] and on the other hand it acts as a carrier for Factor VIII (FVIII), thereby essentially prolonging its half-life in the circulation.[3] VWF circulates as long, loosely coiled multimer chain (also termed concatemer[4]) which abruptly forms large fibers if shear rates exceed a certain threshold value of yet unclear order of magnitude. Depending on the experimental setup, critical shear rates between 3.000 $s^{-1}$[5] and 40.000 $s^{-1}$[6] have been reported and lengths of VWF chains ranged from 300 nm[5] to 100 $\mu$m.[6a] One aim of this study was to provide more clarity by an experimental setup which is, from a fluid dynamic point of view, simple and highly defined, and at the same time allows the study of elongation of VWF at a single molecular scale.

As a consequence of the addressed elongation, VWF gets "sticky", meaning that it increases binding activity toward collagen, platelets, and as shown recently also toward itself.[2,6b] Therefore, VWF is the component which like a glue causes blood clotting more efficiently under high shear stress despite higher hydrodynamic forces dragging platelets.[7] Another functional change, which VWF undergoes upon stretching, is its susceptibility to highly specific cleavage by the protease ADAMTS13.[8] Cleavage occurs between residues Tyr-1605 and Met-1606 which is buried inside the VWF A2-domain and becomes accessible only upon stretching of this domain.[9] Recognition of ADAMTS13 by VWF has been studied under static conditions without flow, revealing a zipper-like multistep interaction and a $K_D$ around 80 nM for globular VWF.[9,10] ADAMTS13 contains two $Ca^{2+}$ and $Zn^{2+}$ ions in its N-terminal metalloprotease domain, which recognizes the cleavage site, whereas the following domains including Dis, Cys, Spacer, TSP 1−8, and CUP1−2 contain no structural metal ions. Actually, it

**Received:** June 2, 2015
**Accepted:** September 14, 2015
**Published:** September 14, 2015

 © 2015 American Chemical Society 

DOI: 10.1021/acs.analchem.5b02078
*Anal. Chem.* 2015, 87, 10299−10305

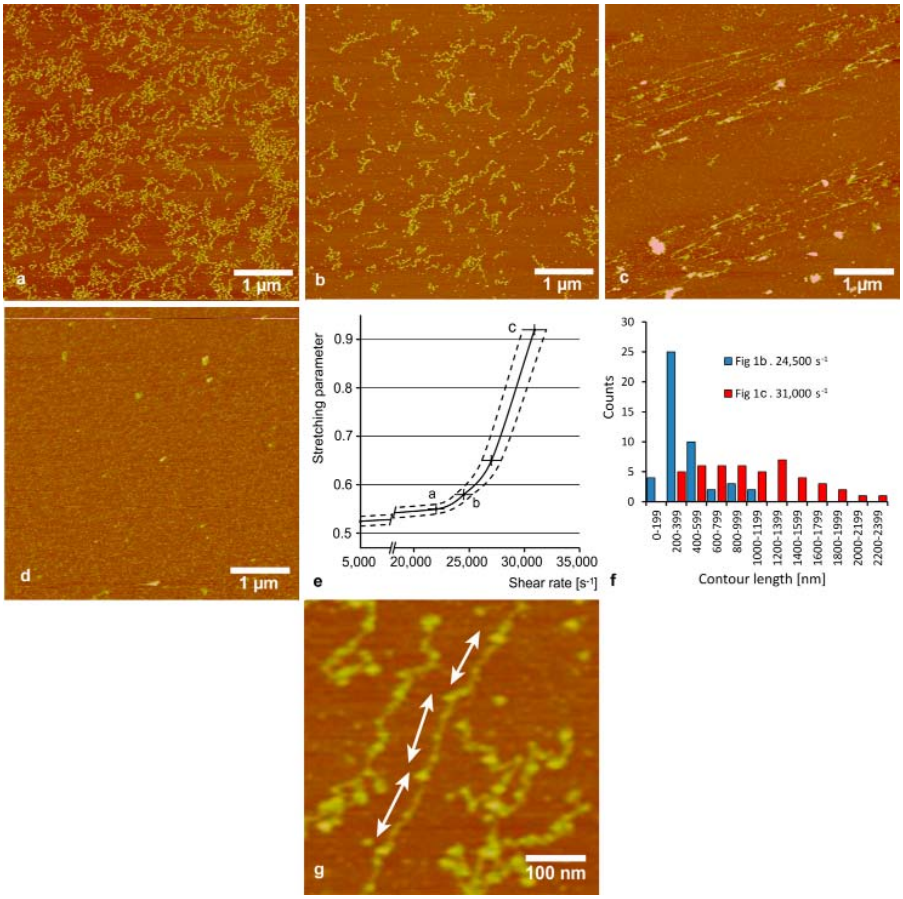


**Figure 1.** VWF stretched at increasing shear rates. Characteristic AFM images from one of three independent experiments. (a) Molecules at a shear rate of 22.000 $s^{-1}$. (b) At 24.500 $s^{-1}$, molecules are partially unraveled and oriented. (c) At 31.000 $s^{-1}$, an almost quantitative stretching of VWF was evident. (d) At 32.000 $s^{-1}$, molecules were broken and displaced from the surface. All images show a certain background of small dots which could be VWF fragments. (e) A plot of the shear rate dependence of the stretching parameter (ratio between the maximum one-dimensional length and the contour length). This is indicative for the linearity and therefore a measure for stretching of VWF. A total of 429 molecules were evaluated, and each data point was derived from three independent experiments. The vertical error range represents the scattering of the three mean values of the stretching parameter derived from these independent experiments. Horizontal errors are determined by the tolerance of the gap width in the stretching device. (f) Length histograms of the partly unraveled VWF chains taken from b and the elongated chains from c. (g) Molecules stretched at 30.000 $s^{-1}$. The linear parts of chains show dimer lengths of 80−100 nm as indicated by two-headed arrows. Height scale: 5 nm from dark to bright.

is known that VWF cleavage by ADAMTS13 requires $Ca^{2+}$,[11] but it remains unclear whether binding to globular VWF (involving domains TSP 5−8 and CUP1−2) is $Ca^{2+}$-dependent. Our experiments provide experimental evidence for the widely believed hypothesis that VWF serves as molecular bus, not only for FVIII but also for ADAMTS13, like a cleaving tool that is ready to become active when VWF is elongated.[9]

In the context of these conformation-dependent functions, a further key function of VWF merits to be elucidated: namely, the ability to bind FVIII, which has not been investigated in terms of shear rate dependence at a macromolecular level. For this mechanobiological study, a microfluidic device was constructed, which will be described elsewhere in more detail, able to stretch single VWF molecules and to immobilize them on a substrate in their elongated conformation. The gentle adhesion of VWF molecules to the substrate is sufficient to avoid recoiling but keeps them functional as shown previously.[12] Recently, we were able to visualize the binding of recombinant (r) FVIII to rVWF on a single molecule level by taking AFM images of the identical rVWF molecule, which was localized by a nanoscale scratch, before and after exposure to rFVIII.[12] Here the same method was applied to VWF molecules which were previously exposed to shear rates up to 32.000 $s^{-1}$, showing that binding of VWF to FVIII is suppressed when it is elongated. This may explain why FVIII is released from its tight complex with VWF in favor of weaker interactions during the activation process. Similar experiments were performed, adding ADAMTS13 to stretched VWF to visualize its cleavage. This should be more comparable to the in vivo situation than the established method of using the monomeric 350-kDa fragment as an indicator for cleavage,[13] because ADAMTS13 is modulating the chain length of VWF multimers rather than quantitatively cleaving VWF and producing 350-kDa pieces (a 350-kDa fragment results exclusively from cleaving the scissile bonds between Tyr-1605 and Met-1606 of two neighboring monomer units in a VWF chain).


DOI: 10.1021/acs.analchem.5b02078
Anal. Chem. 2015, 87, 10299−10305

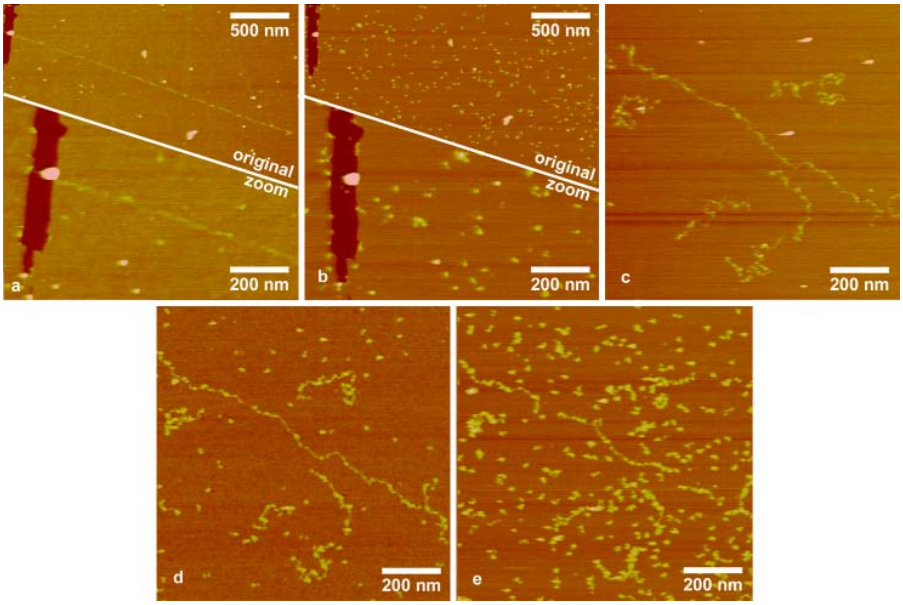


**Figure 2.** Proteolysis of stretched VWF by ADAMTS13. AFM images show exemplarily one of over 20 evaluated molecules from at least two independent experiments. (a and b) One individual VWF molecule with a stretching parameter of ∼1 before and after addition of an ADAMTS13 solution. After 22 s, the totally stretched molecule was quantitatively cleaved into small pieces. The following images demonstrate a stepwise partial cleavage of a VWF with a stretching parameter of 0.7, recorded (c) before addition of ADAMTS13, (d) after 22 s of ADAMTS13 exposure, and (e) after another 38 s of exposure to ADAMTS13 (and thus a total reaction time of 1 min). Cleavage of the VWF chain can be observed at several sites, while the number of free ADAMTS13 molecules expectedly increased. Height scale: 5 nm from dark to bright.

## MATERIALS AND METHODS

**Sources of Recombinant VWF and FVIII.** Recombinant VWF lots used in this study were prepared under identical conditions as described in Seyfried et al.[14] Full-length recombinant FVIII (ADVATE, Baxter) served as source for FVIII. All AFM studies were conducted with rVWF lot HN02R00 (101 IU/mL VWF:RCo activity; 87 IU/mL VWF:Ag) and rFVIII lot LE01L017AA (394 IU/mL chromogenic activity).

**VWF−FVIII Complex Formation on the Mica Surface.** To image identical VWF molecules before and after complex formation with FVIII, a scratch was made on the mica surface by means of an AFM tip. One end of this scratch was wide enough (approximately 1 $\mu$m) to be recognized with a light microscope, whereas the width of the scratch on the opposite end was reduced to nanoscopic sharpness. Then a 200 $\mu$L droplet of a solution containing 0.86 $\mu$g/mL VWF in Tris-buffered saline (TBS, 50 mM Tris, 150 mM NaCl, 0.4 $\mu$M $MgCl_2$, pH 7.4) was applied onto this mica surface for 5 min to adsorb nonstretched chains. To obtain stretched VWF, the mica sheet was treated with VWF solution in a custom-made microfluidic device described below. The mica was rinsed with both buffer and ultrapure water (resistance 0.05 mS/cm) obtained from a Milli-Q apparatus (Millipore, Billerica, MA) and blown dry with nitrogen. The scratch was then used as a marker to position the AFM tip at a specific sample position for imaging individual VWF molecules. The substrate was removed from the microscope, and a droplet of FVIII or ADAMTS13 solution was applied on the surface and incubated between 22 s and 3 min. Afterward the surface was rinsed with ultrapure water and blown dry again. The nanometer-wide scratch was again used to localize and subsequently image the identical VWF molecules after reaction with FVIII or ADAMTS13.

**Stretching VWF.** A device was developed to achieve defined shear rates in a narrow gap (adjustable to single-digit micrometers) between a rotating plate and a mica sheet. A sketch of this device along with an experimental scheme can be found in the Supporting Information. The shear rate could be adjusted by regulating the rotation speed of the plate and the gap width with a precision of less than $\pm 1.000\ s^{-1}$. A 100 mL amount of a solution containing 0.11 $\mu$g/mL VWF was fed to this apparatus for a period of 10 min. The residence time of a molecule in the active gap region is approximately 10 $\mu$s. At the end, ultrapure water was introduced into the stretching device to remove soluble contaminants. The sample was immediately blown dry with nitrogen for subsequent AFM imaging in air.

**AFM Measurements.** All AFM images where recorded in tapping mode (TM) with a NanoScope V (Bruker, Santa Barbara, CA) using etched single crystal silicon probes (NCH from Nanoworld, Neuchatel, Switzerland) with a spring constant of 42 N/m. Images where taken with set points corresponding to a damping of approximately 90% of the free amplitude.

**Image Processing and Data Analysis.** AFM raw images were flattened using the NanoScope Software (Version v7.1.30, Bruker).

**Determination of the Stretching Parameters.** The contour lengths of molecules were determined by redrawing them with a line of segments using Datalab version 3.5.30 (Epina, Pressbaum, Austria, http://datalab.epina.at). This software was also used to measure the maximum one-dimensional lengths of the (coiled) molecules. The stretching parameter was calculated as the quotient of this length and the contour length. The stretching parameters plotted in Figure 1e are the mean values of over 300 molecules derived from three independent experiments.


DOI: 10.1021/acs.analchem.5b02078
Anal. Chem. 2015, 87, 10299−10305

## RESULTS

**Critical Shear Rate for Stretching of VWF.** A new device was developed, which is able to stretch VWF at defined shear rates and immediately adsorb it on a substrate to conserve its stretched conformation, i.e., to freeze it. Figure 1 shows images of VWF molecules observed by AFM at increasing shear rates ranging from 22.000 $s^{-1}$ to 32.000 $s^{-1}$. This results in orientation and disentangling. An increase of the shear rate is accompanied by a rising number of affected molecules. Between 27.000 and 31.000 $s^{-1}$ an (apparently sharp) transition into a significantly elongated state with chain lengths of several micrometers can be observed (Figure 1e). Figure 1d shows the effect of shearing VWF at 32.000 $s^{-1}$. The coverage of the surface with proteins is considerably decreased, and the observable objects are presumably fragments of broken chains. To quantify the degree of stretching, we introduce a "stretching parameter" which is calculated by the ratio between the largest dimension of the molecule and its contour length (described in Materials and Methods). The average stretching parameter reflects the degree of linearization of each molecule and the fraction of affected molecules. In Figure 1e the dependence of the average stretching parameter on the shear rate is depicted. An average stretching parameter of 1 would mean that all evaluated molecules are totally linear. This linearization is a precondition for elongation; therefore, a significant elongation (3-fold increase of contour length) is only occurring at stretching parameters close to 1 (Figure 1f). The length of each dimeric unit at shear rates below 30.000 $s^{-1}$ is typically in the range of the knot diameter (~10−20 nm), whereas above ~30.000 $s^{-1}$ some chains or parts of chains are elongated, resulting in dimeric unit lengths of ~80−120 nm (arrows, Figure 1g). In the molecule in Figure 2a, the knots (D- and A-domains as discussed later) appear to be much smaller or even disappear, suggesting that they undergo some force-induced deformations. Due to the extensive disulfide cross-linkage, these domains cannot be totally unfolded (like A2-domains). A recent optical tweezer experiment revealed a force-induced loop opening within the A1-domain,[15] demonstrating that even a cross-linked VWF domain can respond to forces, with minor elongation but still dramatic three-dimensional rearrangements.

**Proteolytic Cleavage of Shear-Stretched VWF.** When totally stretched VWF chains (stretching parameter ~1; shear rate ~30.000 $s^{-1}$) were exposed to an ADAMTS13 solution in TBS, containing 25 mM $Ca^{2+}$, they were immediately cleaved. In Figure 2a,b the quantitative degradation of a chain after only 22 s is visualized. The molecule was retrieved after exposure to ADAMTS13 by marking the surface position with a nanoscale scratch as published previously.[12] The remaining fragments (most probably the 350-kDa fragments) are not discernible from the excess of ADAMTS13 molecules strewn about the surface. This fragmentation goes in accordance with existing data.[8−10,13] Next, similar experiments were made with partly stretched VWF molecules (Figure 2c), with stretching parameters of 0.7, at which FVIII binding still occurs as shown in the last section. Proteolysis was interrupted after 22 s by rinsing the sample with ultrapure water and blowing it dry with nitrogen (Figure 2d). After AFM analysis of the partly cleaved VWF chains, the sample was exposed to the ADAMTS13 solution again for another 38 s and subsequently imaged for a third time (Figure 2e). In Figure 2d no significant cleavage can be observed after 22 s and cleavage is still not quantitative after 1 min. From this we conclude that VWF is already susceptible for cleavage at a lower degree at medium shear conditions with no significant elongation, although proteolysis is further enhanced in the case of fully stretched molecules.[3,16]

**Binding of ADAMTS13 to VWF.** The observation that ADAMTS13 readily cleaves VWF at moderate stretching opens up the question whether VWF molecules absorbed under static conditions (no shear) can be cleaved. In the literature it is described that coiled VWF is not cleaved due to the poor accessibility of the "scissile bond" but it is able to bind ADAMTS13.[9,11] However, VWF molecules absorbed onto a surface do not show a globular shape but look more extended. To clarify this question, our single molecule approach for binding experiments was again applied.[12] Comparing parts a and b of Figure 3, the binding of ADAMTS13 to the multimeric VWF backbone is evident, but no cleavage can be observed. This experiment was performed in a buffer containing 25 mM $CaCl_2$ to stabilize ADAMTS13. Following the model of Crawley et al.,[9] and assuming that only the $Ca^{2+}$- and $Zn^{2+}$-containing metalloprotease domain acts $Ca^{2+}$-dependently, ADAMTS13 is expected to bind VWF also under exclusion of $Ca^{2+}$. An ADAMTS13 binding experiment performed without $Ca^{2+}$ is shown in Figure 3c,d. Evaluation of over 30 molecules, containing approximately 600 knots however showed that with $Ca^{2+}$, 13% of all VWF monomers bound ADAMTS13, whereas without $Ca^{2+}$, binding was reduced to 4%. Interestingly, this $Ca^{2+}$ dependency of activity toward VWF is converse to that of FVIII which is losing its VWF affinity at increased $Ca^{2+}$ concentrations.[12]

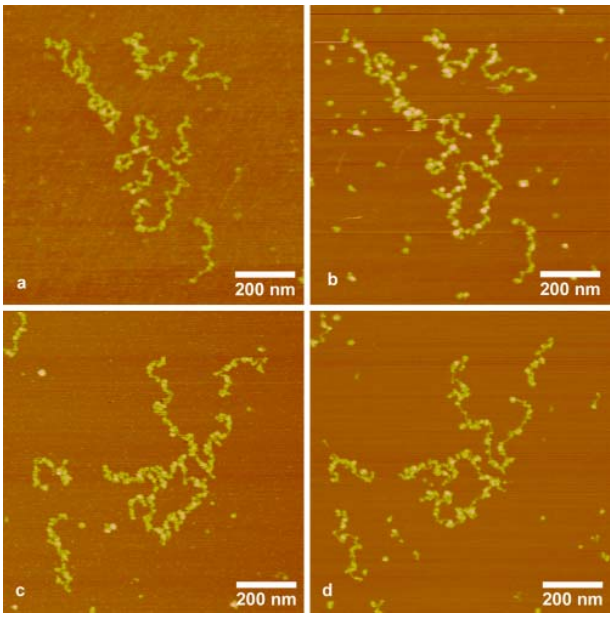


**Figure 3.** ADAMTS13 binding to VWF. Images a and b show VWF multimers before and after reaction with ADAMTS13 in the presence of $Ca^{2+}$. Binding of ADAMTS13 to VWF is clearly visible as brighter spots. In c and d the identical experiment was performed under exclusion of $Ca^{2+}$. Few binding events can be observed. Height scale: 5 nm from dark to bright.

**FVIII Binding Activity of Shear-Stretched VWF.** Single shear-stretched VWF molecules were imaged before exposure to FVIII and thereafter using a nanoscale scratch as marker following a recently published procedure.[12] In Figure 4a a VWF


DOI: 10.1021/acs.analchem.5b02078
Anal. Chem. 2015, 87, 10299−10305

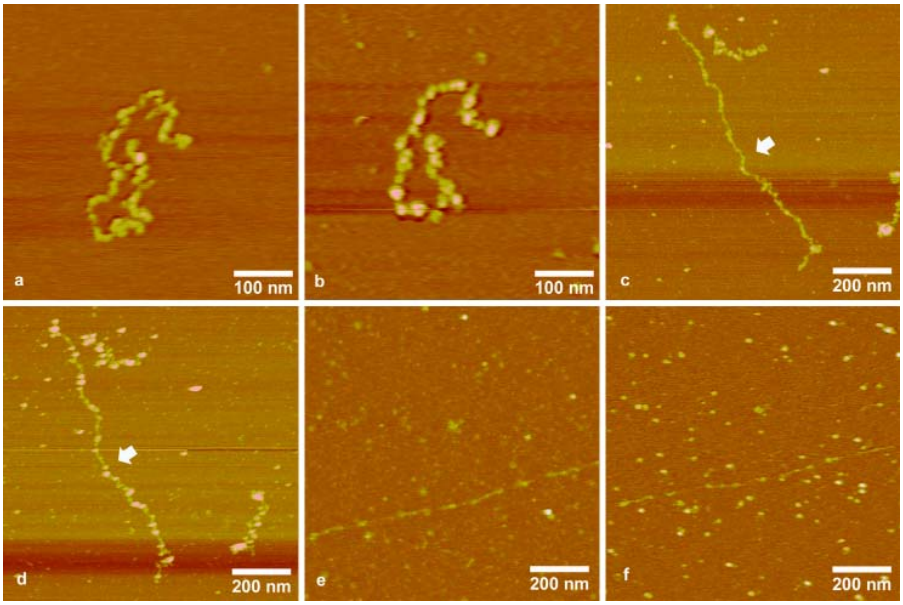


**Figure 4.** Shear-dependent interaction between VWF and FVIII. AFM images show exemplarily 1 of over 20 evaluated molecules from at least two independent experiments. The VWF molecule shown in image a was deposited without shear stress (stretching parameter ~0.5). In image b this molecule is shown after reaction with FVIII. Numerous larger knots along the VWF chain can be seen, indicating complex formation with FVIII. The VWF chain in image c has a stretching parameter of 0.8. Unraveling but no contour length elongation can be observed. (d) The molecule was imaged after reaction with FVIII still resulting in distinct complex formation. (e) Fully stretched VWF with a stretching parameter of ~1. The same molecule after exposure to a FVIII solution is depicted in image f. Numerous free FVIII molecules can be discerned as small spots. No FVIII has bound to the VWF chain. Height scale: 5 nm from dark to bright.

molecule absorbed under static conditions (no flow) is depicted. Figure 4b shows the identical molecule after interaction with FVIII. The large and bright knots can be assigned to bound FVIII. A VWF molecule with a stretching parameter of 0.8, comparable to that of Figure 2c, is shown in Figure 4c (marked with an arrow). The molecule is disentangled, showing no loops or hitches, but it is not totally linear and therefore not elongated fully in terms of contour length. After interaction with FVIII (Figure 4d), many new globular structures of larger size than the globular units of VWF alone are evident, indicating that at this degree of stretching VWF is still binding FVIII. Moreover, the number density of FVIII molecules along the VWF chain is rather high (also closely adjacent FVIII molecules can be observed). This is consistent with a recent electron microscopy observation[17] that each D′D3 dimer is able to bind two FVIII molecules. Figure 4e,f shows a fully stretched VWF molecule (at a shear rate of ~30.000 $s^{-1}$, stretching parameter ~1) before and after exposure to FVIII. The VWF chain looks more or less identical before and after FVIII treatment, and there is no indication of FVIII molecules attached to the VWF chain.

## DISCUSSION

We showed in a semiquantitative manner that single isolated VWF molecules begin to undergo shear-rate-dependent disentangling and orientation at shear rates above ~20.000 $s^{-1}$ before sharply changing into an elongated conformation around 30.000 $s^{-1}$. There are data, derived from single molecule force spectroscopy and optical tweezers experiments of the VWF A2-domain and the VWF A1A2A3-tridomain construct, addressing the required forces for unfolding and elongation.[18] Those investigations concordantly show nonlinear force distance curves with a sudden elongation to the 3-fold length at approximately 20−30 pN. The correlation of stretching forces obtained in a two-point pulling experiment with the corresponding shear rate is not trivial. However, our experiments show such a sharp elongation at around 30.000 $s^{-1}$. At first sight, this high value may seem contradictory to those published previously, which found shear-stretched VWF fibers over a critical shear rate of 5.000 $s^{-1}$.[7] However, a recent publication reports that VWF fibers were almost absent at 12.500 $s^{-1}$ and readily formed at 125.000 $s^{-1}$,[19] which approximately corresponds to our results. There might be two major reasons for these conflicting results: (i) So far, "stretching" of VWF has been visualized solely with light microscopy-based methods (maximum resolution of several 100 nm) which can not distinguish between fibers and single VWF molecules. Therefore, it is not clear whether in those experiments the single VWF molecules are elongated and/or assembled to long fibers. Actually, recent works sustain the formation of even macroscopic fibers by VWF−VWF bridges.[2,6a] The formation of such fibers is supposed to be quite a slow process. It should be considered that a low critical shear rate of 5000 $s^{-1}$[17] was found in an experimental setup which exposes the VWF solution to the shear rate for several minutes, whereas in our experiment, as well as in the mentioned high shear rate case,[19] the exposure is on the order of milliseconds. (ii) In light microscopy-based experiments VWF is only detected in case of elongation and/or fiber formation, whereas a potentially dominating fraction of unaffected VWF remains unexplored. The situation is substantially different in our AFM-based experiments: Here all molecules are detected, stretched, and nonstretched. This might shift the observed critical shear rate to higher values. Our rheometer-type device should bring more clarity, as it is on the one hand very close to the technological standard of rheological experiments (two-plate


DOI: 10.1021/acs.analchem.5b02078
Anal. Chem. 2015, 87, 10299−10305

rheometer) and on the other hand it mimics pathophysiological flow situations due to the short exposure time (which is also the case in pathophysiological conditions, e.g., stenosis). Experiments with sophisticated flow chambers of different geometries suggest that under physiological conditions shear rates in the range of tens of thousands $s^{-1}$ are typical in Y-shaped vessels with a stagnation point flow.[6] Moreover, extremely high shear rates can occur in pathological conditions such as stenosis or in patients with cardiac valves.[20] Under physiological conditions, the situation might be more complicated, because of the presence of platelets and, at sites of injury, also collagen surfaces, both binding VWF and potentially shifting the threshold shear rates for partial and total stretching of VWF. Therefore, it should be emphasized that the shear-rate-dependent stretching described here represents the specific case of VWF elongated by the influence of the surrounding flowing liquid, not considering adhesive vessel walls or platelets. In the following considerations we will use the already described stretching parameter (ratio between overall length and contour length) to discuss the effect of FVIII and ADAMTS13 with regard to the degree of stretching of VWF.

The metalloprotease ADAMTS13 is known to interact especially with stretched VWF, thereby cleaving the unfolded VWF A2-domain at Tyr-1605 and Met-1606. Recent studies have revealed a seven-step zipper-like binding and cleaving process which begins with the recognition of the C2 domain of VWF by the CUB2 domain of ADAMTS13 and can be understood as a successive positioning of a series of exosites on the flexible VWF chain, which is then cleaved by a single proteolytic site in the metalloprotease domain of ADAMTS13.[9] The smallest possible fragment, that can occur when the "scissile bonds" of two neighboring VWF monomer units are cleaved, has a size of 350 kDa. In the circulation ADAMTS13 is modulating the chain length of VWF. The formation of this characteristic smallest fragment is largely improbable because VWF, once it is cleaved, has a higher tendency to recoil and to bury the "scissile bonds" inside the A2-domains. In our experiments VWF multimers are immobilized in their fully or partly stretched conformation and cannot spontaneously relax. Furthermore, we visually detected cleaved, i.e., shortened objects as such, independently from their length, whereas in the literature the proof for cleavage basically relies on the formation of the smallest possible fragment (350 kDa) and detection by SDS-PAGE. Therefore, this approach reflects the modulation of chain length by a preferential cleavage of particularly long multimers into smaller ones. Interestingly, a partial cleavage is observable at shear rates of moderate stretching, with largely unchanged distances between monomeric knots. This could explain why large VWF bundles are readily degraded by ADAMTS13[21] at much lower shear rates. Because immobilized VWF, even in its coiled form, adsorbed without shear forces, assuming a rather loosely packed shape with discernible rod-like sections between the knots, it is remarkable that in this case our experiments showed no cleavage, suggesting that the A-domains are part of the large knots. In fact the assumption that the rod-like sections between those knots represent the domains C1-CK (according to the newer nomenclature) while the A-domains are integrated into the knots, agrees well with the EM images recently provided by Zhou et al.[16] The VWF A2 cleaving activity of ADAMTS13 is regulated by $Ca^{2+}$ and $Zn^{2+}$,[22] but far less is known about the metal ion dependency of ADAMTS13 binding to VWF. Our results show that ADAMTS13 binding to VWF can be strongly reduced under exclusion of $Ca^{2+}$.

Shear-induced stretching of VWF is known to be essential for the formation of white thrombus (primary hemostasis), mediating enhanced adhesion of platelets to endothelial cells under flow conditions.[7] Here the VWF−FVIII interaction, which is relevant for the activation cascade of the secondary hemostasis, is also shown to be shear-dependent. The finding that fully stretched VWF (stretching parameter ∼1) has a strongly reduced binding affinity to FVIII, most likely means that VWF−FVIII complexes disassemble if they are stretched, because this noncovalent complex formation is fully reversible. The biological relevance of the complex formation between VWF and FVIII consists of prolonging the short half-life of free FVIII in the circulation by protecting it from proteolytic attack and from premature reaction with factor IXa and uptake by receptors. It should be noted that FVIII's affinity to VWF is much higher (100-fold) than to FIX.[3] The mechanism, how FVIII is released from its complex with VWF to be further processed in the FX activation complex, includes activation by thrombin and requires a phospholipid surface.[3] Furthermore, it has been shown that the complex formation to VWF inhibits the FIXa binding site.[3] Another study revealed that the FVIII affinity of VWF decreases by a factor of 5 when it is bound to immobilized collagen.[23] We assume that the shear force-induced decomposition of the VWF−FVIII complex plays an unexpected role in enhancing the secondary hemostasis at shear rates of full VWF stretching, by triggering the release of FVIII from its carrier. It would be interesting to study whether a strong local increase of shear rates, e.g., occurring at cardiac valves, known to cause acquired von Willebrand syndrome (AVWS),[24] may also cause temporary FVIII deficiency.

So far it is believed that elongation of VWF is just a matter of unfolding the A1,A2,A3-tridomains.[1] Considering, on the one hand, that the attack of ADAMTS13 requires an unfolded A2-domain which already occurs at stretching parameters of 0.7 but, on the other hand, that the most impressive elongation of the entire chain is observed at stretching parameters close to 1, we suggest that other domains might also undergo similar unfolding processes. This is supported by Zhou et al.,[16] who report hinges between the D′D3 and the A1-domains (and between A1 and A2) which should allow a certain flexibility to the entire globular N-terminal head region. Previous works, based on two point-pulling experiments, showed that the A2-domain can be elongated up to approximately 50−60 nm,[18a,c] which is just slightly sufficient to explain the dimeric length of 80−120 nm observed for fully stretched molecules in this study (Figure 1 g); hence, the elasticity buffer is exhausted, and the stiffer, disulfide-cross-linked domains see an undamped force load. It should be mentioned that the interaction between VWF and FVIII is based on at least two synergistically acting exosites[3] (although a recent work upvalued one major binding site within the FVIII C1 domain, at the same time highlighting the importance of unexplored conformational changes induced by D′D3 binding[17a]) with a defined separation and low tolerance for elongation. Finally, the typical knots, which have recently been identified as the N-terminal head regions,[16] become smaller or even disappear at stretching parameters close to 1. The site of covalent multimerization of VWF is located within the D′D3 domain construct close to the A1-domain (C1099−C1099 and C1142−C1142). It is not resolved on a structural level, which parts of this VWF subunit contribute to force transmission in a stretched chain. The


DOI: 10.1021/acs.analchem.5b02078
Anal. Chem. 2015, 87, 10299−10305

absence of knot structures in stretched VWF strongly indicates a massive structural change. Taken together, this deformation of D-domain knots, which contain the binding sites, could explain the shear rate dependence of FVIII binding. Anyhow, this FVIII release can be seen as a kind of inversion of the scenario where FVIII impairs the shear-dependent cleavage of VWF A2-domain:[13] Seen in the light of our experiments, shear stress impairs FVIII binding.

The force-induced release of FVIII completes the puzzle of how VWF participates in hemostasis. The known puzzle pieces illustrate the force-dependent adhesion of VWF on the vessel walls and the transport of FVIII ("molecular bus"). Adding our results, we see a targeting mechanism for FVIII to sites of vascular injury: VWF circulating at moderate or medium shear rates docks to collagen or alpha(IIb)beta(3) receptor of immobile platelets. This promotes further (full) elongation, which triggers release of FVIII. The "passenger" FVIII might then still have to "walk" a short distance to the phospholipid membrane to start secondary hemostasis which is facilitated by a recently published $Ca^{2+}$-dependent self-stabilizing mechanism of FVIII.[25]

## ASSOCIATED CONTENT

### Supporting Information

The Supporting Information is available free of charge on the ACS Publications website at DOI: 10.1021/acs.analchem.5b02078.

Experimental scheme with a sketch of the device used for exposing VWF molecules to shear stress (PDF)

## AUTHOR INFORMATION

### Corresponding Author

*Fax: +43 1 58801915110. E-mail: gernot.friedbacher@tuwien.ac.at.

### Notes

The authors declare the following competing financial interest(s): H. Rottensteiner, G. Schrenk, F. Scheiflinger, and P. L. Turecek are full time employees at Baxalta Innovations. K. Bonazza, F. Frank, G. Allmaier, and G. Friedbacher declare that they have no conflict of interest.

## REFERENCES

(1) Lenting, P.; Casari, C.; Christophe, O.; Denis, C. *J. Thromb. Haemostasis* **2012**, *10*, 2428−2437.
(2) Chen, H.; Fallah, M. A.; Huck, V.; Angerer, J. I.; Reininger, A. J.; Schneider, S. W.; Schneider, M. F.; Alexander-Katz, A. *Nat. Commun.* **2013**, *4*, 1333.
(3) Lenting, P. J.; Van Mourik, J. A.; Mertens, K. *Blood* **1998**, *92*, 3983−3996.
(4) Springer, T. A. *Blood* **2014**, *124*, 1412−1425.
(5) Siedlecki, C. A.; Lestini, B. J.; Kottke-Marchant, K.; Eppell, S. J.; Wilson, D. L.; Marchant, R. E. *Blood* **1996**, *88*, 2939−2950.
(6) (a) Kragh, T.; Napoleone, M.; Fallah, M. A.; Gritsch, H.; Schneider, M. F.; Reininger, A. J. *Thromb. Res.* **2014**, *133*, 1079−1087. (b) Reininger, A. J.; Heijnen, H. F.; Schumann, H.; Specht, H. M.; Schramm, W.; Ruggeri, Z. M. *Blood* **2006**, *107*, 3537−3545.
(7) Schneider, S.; Nuschele, S.; Wixforth, A.; Gorzelanny, C.; Alexander-Katz, A.; Netz, R.; Schneider, M. *Proc. Natl. Acad. Sci. U. S. A.* **2007**, *104*, 7899−7903.
(8) Shim, K.; Anderson, P. J.; Tuley, E. A.; Wiswall, E.; Sadler, J. E. *Blood* **2008**, *111*, 651−657.
(9) Crawley, J. T.; de Groot, R.; Xiang, Y.; Luken, B. M.; Lane, D. A. *Blood* **2011**, *118*, 3212−3221.
(10) (a) Feys, H.; Anderson, P.; Vanhoorelbeke, K.; Majerus, E.; Sadler, J. *J. Thromb. Haemostasis* **2009**, *7*, 2088−2095. (b) Zanardelli, S.; Chion, A. C.; Groot, E.; Lenting, P. J.; McKinnon, T. A.; Laffan, M. A.; Tseng, M.; Lane, D. A. *Blood* **2009**, *114*, 2819−2828.
(11) Tsai, H.-M. *Blood* **1996**, *87*, 4235−4244.
(12) Bonazza, K.; Rottensteiner, H.; Seyfried, B. K.; Schrenk, G.; Allmaier, G.; Turecek, P. L.; Friedbacher, G. *Anal. Bioanal. Chem.* **2014**, *406*, 1411−1421.
(13) (a) Cao, W.; Krishnaswamy, S.; Camire, R. M.; Lenting, P. J.; Zheng, X. L. *Proc. Natl. Acad. Sci. U. S. A.* **2008**, *105*, 7416−7421. (b) Cao, W.; Sabatino, D. E.; Altynova, E.; Lange, A. M.; Casina, V. C.; Camire, R. M.; Zheng, X. L. *J. Biol. Chem.* **2012**, *287*, 32459−32466. (c) Skipwith, C. G.; Cao, W.; Zheng, X. L. *J. Biol. Chem.* **2010**, *285*, 28596−28603.
(14) Seyfried, B. K.; Friedbacher, G.; Rottensteiner, H.; Schwarz, H. P.; Ehrlich, H.; Allmaier, G.; Turecek, P. L. *Thromb. Haemostasis* **2010**, *104*, 523−530.
(15) Kim, J.; Hudson, N. E.; Springer, T. A. *Proc. Natl. Acad. Sci. U. S. A.* **2015**, *112*, 4648−4653.
(16) (a) Zhou, Y.; Eng, E.; Nishida, N.; Lu, C.; Walz, T.; Springer, T. *EMBO J.* **2011**, *30*, 4098−4111. (b) Zhou, Y.; Eng, E.; Zhu, J.; Lu, C.; Walz, T.; Springer, T. *Blood* **2012**, *120*, 449−458.
(17) (a) Chiu, P.-L.; Bou-Assaf, G. M.; Chhabra, E. S.; Chambers, M. G.; Peters, R. T.; Kulman, J. D.; Walz, T. *Blood* **2015**, *126*, 935−938. (b) Yee, A.; Oleskie, A. N.; Dosey, A. M.; Kretz, C. A.; Gildersleeve, R. D.; Dutta, S.; Su, M.; Ginsburg, D.; Skiniotis, G. *Blood* **2015**, *126*, 939−942.
(18) (a) Jakobi, A. J.; Mashaghi, A.; Tans, S. J.; Huizinga, E. G. *Nat. Commun.* **2011**, *2*, 385−394. (b) Wu, T.; Lin, J.; Cruz, M. A.; Dong, J.-F.; Zhu, C. *Blood* **2010**, *115*, 370−378. (c) Xu, A. J.; Springer, T. A. *Proc. Natl. Acad. Sci. U. S. A.* **2012**, *109*, 3742−3747.
(19) Colace, T. V.; Diamond, S. L. *Arterioscler., Thromb., Vasc. Biol.* **2013**, *33*, 105−113.
(20) (a) Haruguchi, H.; Teraoka, S. *J. Artif. Organs* **2003**, *6*, 227−235. (b) Sharma, S. K.; Sweeny, J.; Kini, A. S. *Cardiol. Clin.* **2010**, *28*, 55−70.
(21) Pappelbaum, K. I.; Gorzelanny, C.; Grässle, S.; Suckau, J.; Laschke, M. W.; Bischoff, M.; Bauer, C.; Schorpp-Kistner, M.; Weidenmaier, C.; Schneppenheim, R.; Obser, T.; Sinha, B.; Schneider, S. W. *Circulation* **2013**, *128*, 50−59.
(22) Anderson, P. J.; Kokame, K.; Sadler, J. E. *J. Biol. Chem.* **2006**, *281*, 850−857.
(23) Bendetowicz, A. V.; Wise, R. J.; Gilbert, G. E. *J. Biol. Chem.* **1999**, *274*, 12300−12307.
(24) Casonato, A.; Sponga, S.; Pontara, E.; Cattini, M. G.; Basso, C.; Thiene, G.; Cella, G.; Daidone, V.; Gerosa, G.; Pagnan, A. *Thromb. Haemostasis* **2011**, *106*, 58−66.
(25) Bonazza, K.; Rottensteiner, H.; Schrenk, G.; Fiedler, C.; Scheiflinger, F.; Allmaier, G.; Turecek, P. L.; Friedbacher, G. *Anal. Bioanal. Chem.* **2015**, *407*, 6051−6057.



DOI: 10.1021/acs.analchem.5b02078
*Anal. Chem.* 2015, 87, 10299−10305

Biomicrofluidics, to be submitted (2016)

# A bio-inspired method for direct measurement of local wall shear rates with micrometer localization using the multimeric protein von Willebrand factor as sensor molecule

Klaus Bonazza [1], Bernhard Scheichl [2,3], Johannes Frank [4], Hanspeter Rottensteiner [5], Gerald Schrenk [5], Gernot Friedbacher [1], Peter L. Turecek [5], Günter Allmaier [1a)]

[1] *Institute of Chemical Technologies and Analytics, Vienna University of Technology, Getreidemarkt 9, A-1060 Vienna, Austria*

[2] *Institute of Fluid Mechanics and Heat Transfer, Vienna University of Technology, Getreidemarkt 9, A-1060 Vienna, Austria*

[3] *AC²T research GmbH (Austrian Center of Competence for Tribology), Viktor-Kaplan-Straße 2C, A-2700 Wiener Neustadt, Austria*

[4] *Joint Workshop Technical Chemistry, Getreidemarkt 9, A-1060 Vienna, Austria*

[5] *Baxalta Innovations, Industriestraße 67, A-1221 Vienna, Austria*

Wall shear rates are critical for a broad variety of fluidic phenomena and are taken into account in nearly every experimental or simulation study. Generally, the shear rate is not observable directly but rather derived from other parameters like pressure and flow, often assuming somehow idealized systems. However, there is a biological system which is able to constantly measure the wall shear as a part of a regulatory circuit: The blood circulation system takes advantage of shear rate sensor (protein-)molecules (multimeric forms of von Willebrand Factor, VWF), which are dissolved in the blood plasma and dramatically change their conformation under shear conditions. The conformational changes are accompanied by several functional variations and therefore interplay with the regulation of the coagulation system. In this study we use a recombinantly produced, and therefore well-defined multimeric form of VWF as sensor which directly responds to shear-rates. Shear rates, up to 32.000 $s^{-1}$, were obtained in a kind of micro plate-to-plate rheometer, capable to adsorb shear-stretched VWF oligomeric molecules on a surface to conserve their differently stretched conformation and so allowing detection of their elongation by Atomic Force Microscopy. The laminar flow in this geometrically simple device has been characterized using classical fluid dynamical models, in order to ensure well-known, stable shear rates which could be correlated quantitatively to an observed stretching of sensor molecules.[1]

a) Author to whom correspondence should be addressed. Electronic mail: guenter.allmaier@tuwien.ac.at

## I. INTRODUCTION

Boundary conditions at solid/fluid-interfaces are critical for various fields and applications like mass transport [1], energy transport [1, 2], surface cleaning in food hygiene and medicine [3, 4], aerodynamics [1], hydrodynamics, blood coagulation [5, 6], etc. The wall shear rate is an often inaccessible parameter. Lots of efforts have been made in the past to measure local wall shear rates or shear stress. The first approaches were inspired from aerospace engineering and based on static hole pairs with separations in the mm or cm range [1, 7]. A more recent work which uses porous elements can be seen as an improvement and miniaturization of this ideas [8]. Shear stress has also been determined by detection of the stress transferred to the solid, either by using deformable gels [9] or the optical stress response of liquid crystals [10]. Tracer particles have been used successfully to gain information about the local shear conditions in combination with sophisticated optical detection strategies [11] and finally diffusion controlled electrochemical reactions on the surface of small platinum electrodes revealed to be shear rate dependent [12]. From all these methods the two latter ones have probably the largest potential for downscaling given the latest progresses in high resolution optical microscopy (Nobel price for chemisty 2014) and the fact that microelectronics has reached the nano-scale [13].. The rise of microfluidics requires more and more direct detection and quantification of local wall shear rates with spatial resolution preferably in the micrometer or even sub-micrometer range. Due to the limitations in measuring such data most studies rely on calculated wall shear rates [14]. CFD simulations depend on such new experimental data [3, 15] especially when applied to micro- or nano-fluidic systems.

Here, a bio-inspired approach for local shear rate detection is presented. Blood platelets in the circulation have the unique tendency to adhere on the surface of blood vessels and form stable plugs most efficiently in high shear conditions. The blood plasma contains shear rate sensor molecules (von Willebrand Factor, VWF) which are long multimeric (2 up to 40 covalently linked monomeric units) glycoprotein chains. At low shear rates they circulate as loosely coiled globular structures with diameters of~90 nm [16] as shown in the cartoon in Figure 1, left side. At increasing shear rates VWF gets uncoiled (Figure 1, center), forms fibrils (Figure 1, right side) and becomes able to bind both, blood platelets and injured vessel walls acting as a linker and binding the platelets to the injured tissue.

In this study it is demonstrated that VWF can be used for detection of local shear rates also in an artificial system. Instead of detecting functional changes of the molecule [17], like nature does, here the morphological transition is directly detected by atomic force microscopy (AFM). Shear rates were generated in a home-built device which can be understood as an upgrade and a miniaturization of a high precision plate-to-plate rheometer (Figure 2). These experiments can be seen as a progress to understand stretching of VWF which is essential for physiological function of blood coagulation[18-20]. This system represents also a new strategy for local shear rate sensing which is the focus of the present work.

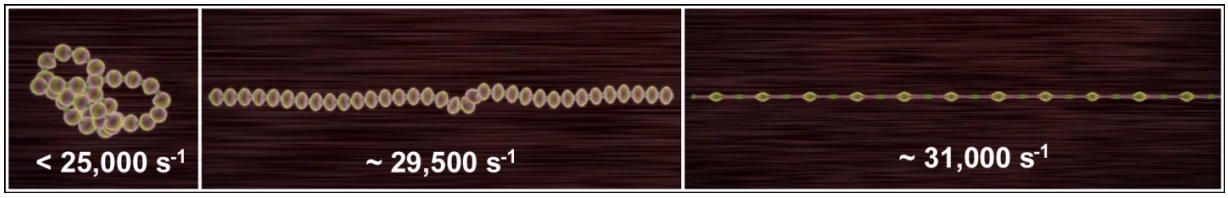


FIG. 1. Cartoon of the sensor molecule (von Willebrand Factor multimer) in solution at different shear-rates based on AFM data. The chain-like molecule consists of periodically repeating mayor (yellow) and minor (green) globes and flexible (pink) interconnects. At low shear rates it is loosely coiled (< 25,000 $s^{-1}$), between ~ 25,000 $s^{-1}$ and ~ 30,000 $s^{-1}$ there is a stochastic unravelling and at ~ 31,000 $s^{-1}$ chains get strongly elongated and the diameter of globes start to decrease strongly.

## II. EXPERIMENTAL

An aqueous buffer solution (Tris-buffered saline, TBS, containing 50 mM Tris, 150 nM NaCl and 0.4 µM MgCl2) was fed to the device described below thereby applying defined shear rates to the liquid. The buffer solution contained the chain-like shear force sensor molecules (von Willebrand Factor, VWF) in low concentration (0.11 µg/mL) which could be stretched at high shear conditions. The immobilization of these molecules on an appropriate surface (freshly cleaved mica) allowed a subsequent AFM imaging which was used to determine the effect of shear rates to the sensor molecules. This experiment was performed at 5 different shear rates (Table I). Three independent mica samples were analyzed for every shear rate.

TABLE I. Parameters used for samples shown in Figure 2 a to e. The error range for tangential shear rate is given by the tolerance of gap width (± 1 µm), the error of radial shear rate is the gap width tolerance plus the time and volume errors of flow measurement.

| Sample | a | b | c | d | e |
|---|---|---|---|---|---|
| Rotational speed of rotor [RPM] | 2100 | 2341 | 2578 | 2817 | 3054 |
| Liquid flow [mL/min] | 5,9 | 6,6 | 7,3 | 8,0 | 8,6 |
| Shear rate tangential [$s^{-1}$] | 21.991 | 24.511 | 27.003 | 29.495 | 31.986 |
| Shear rate error [$s^{-1}$] | 709 | 791 | 871 | 951 | 1.032 |

The shear stress device: The centerpiece of the device (Figure 2) is a plane rotating plate arranged parallel to the sample (Figure 2 d). The cone shape at the margins should minimize turbulences. TBS buffer solution containing the protein is fed to the system through a hole in the middle of the sample plate, which consists of a mica plate glued to a polished, plane steel sample holder with epoxy resin. After drilling the central hole, mica sheets were cleaved using adhesive tape, resulting in

atomically flat surfaces with occasional steps of some nanometers height (checked by AFM). The precision of the gap in terms of distance and planarity is crucial for obtaining accurate shear rates. Therefore the rotor is mounted with a spindle bearing arrangement (Figures 2 b and c) and all parts were fabricated from the same steel (X2CrNiMo17-12-2) to prevent differences in thermal dilatation. Furthermore the geometry (Figure 2 d) was optimized to reduce the distance between the fix bearing and the rotor surface with respect to possible thermal disequilibrium caused by friction. Cleaved mica sheets vary in thickness and therefore an O-ring was used as a spring to press the sample towards the tapered case with a force of ~ 50 N. The cap, which is holding the sample and the spring O-ring and is connected with the feed tubing, is mounted by a toggle lever for quick removal of the sample. Rotation of a DC-motor is transmitted to the rotor by a timing belt drive (gear ratio 1 : 1,66) shown in Figures 2 b and c.

In order to permit adjusting of the gap size, the steel case is composed of two telescopically fitting parts: the inner one containing the bearing- and sealing-unit and the outer, inverted cone shaped one, which determines the sample position (Fig 2 d). These two parts are moved parallel to each other by 3 differential pitch spindles synchronized by a special timing belt with a zero-play tooth engagement. Each spindle has two different threads, 0.2 mm and 0.25 mm, resulting in a translation of 50 µm per full turn (Figures 2 c and d).

The setup: The whole setup is depicted in Figure 2 a. The buffer solution containing VWF is pumped into the device by a gas overpressure in the reservoir. The setup consists of a nitrogen bottle (containing nitrogen quality 5.0), a ball valve and a manometer with a scale splitting of 0.1 atmospheres which is connected by 3 mm diameter PE tubes to the pressure resistant reservoir (100 mL PTFE bottle, max 5 atmospheres). A ~ 20 cm long PTFE tube with an inner diameter of 1 mm connects the reservoir with the plate-to-plate rotor device. The outlet consists of another identical PTFE tube.

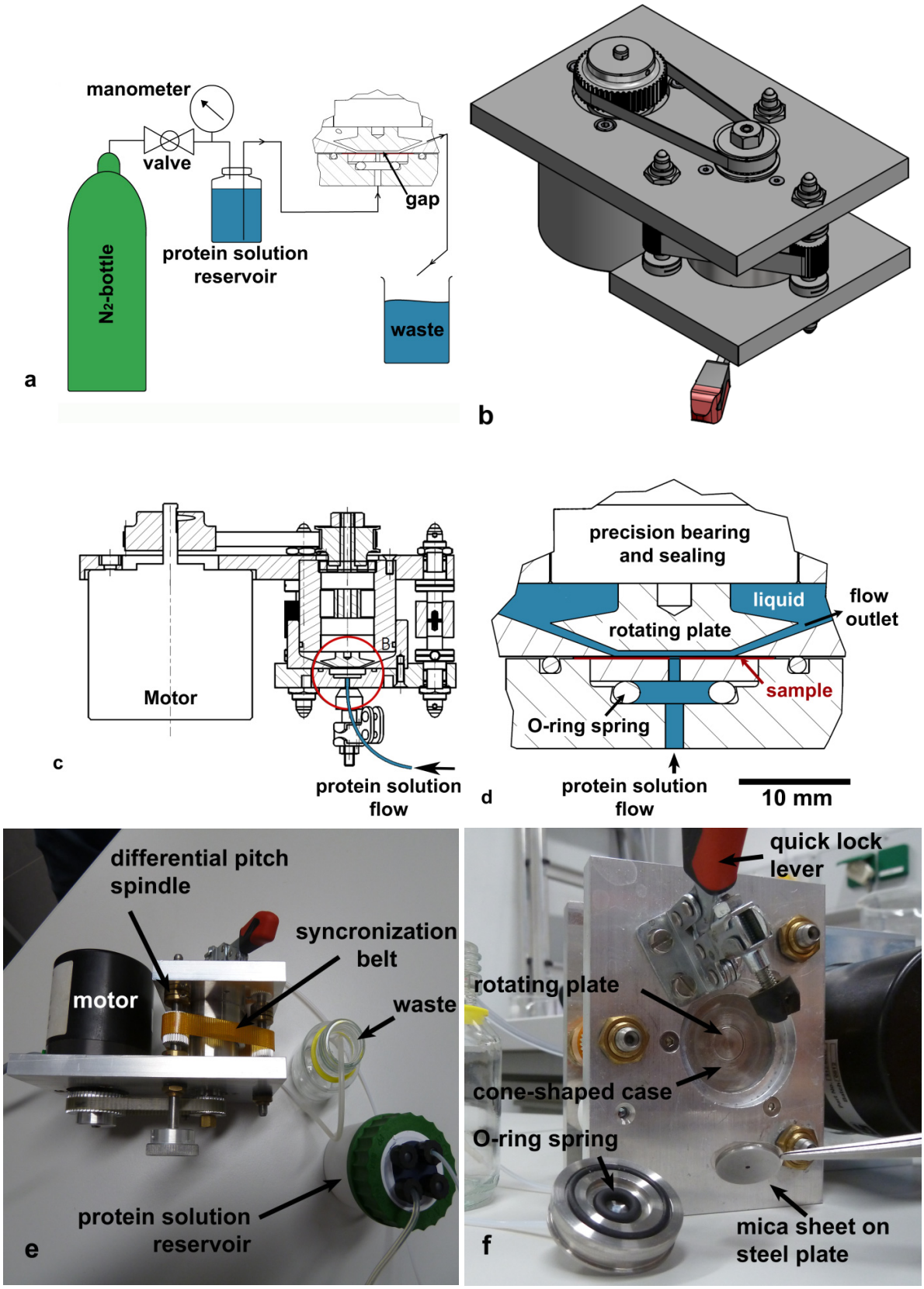
manometer
valve
gap
N2-bottle
protein solution
reservoir
waste
a
b
Motor
c
protein solution
flow
precision bearing
and sealing
liquid
flow
outlet
rotating plate
sample
O-ring spring
protein solution
flow
d
10 mm
differential pitch
spindle
syncronization
belt
motor
waste
protein solution
reservoir
e
quick lock
lever
rotating plate
cone-shaped case
O-ring spring
mica sheet on
steel plate
f

FIG. 2. a) Experimental setup (schematic). (b) View of the device, showing the gap-width adjusting system. The 3 differential pitch spindles are driven by a precision synchronous belt to permit a parallel movement of the sample relative to the rotating plate. The red lever is a quick lock for removing the mica sample. (c) Cross-section, the red circle denotes detail (d) of the geometry of the plate-to-plate rheometer unit. The sample surface (freshly cleaved mica sheet) is colored in red, the volume filled with VWF solution is blue. The gap width is not to scale. (e) Foto of the experimental setup. (f) shows in detail the rotating plate which is planar and vertically adjustable relatively to the cone-shaped steel case (gap width adjustment). The mica sheet, mounted on a steel plate, is pressed to this steel case by an O-ring spring and a steel cap using the quick lock lever.

Determination of the gap size $\widetilde{H}$: The gap size was measured off-line using a digital gauge with a precision of ± 0.5 µm (Digital, Mitutoyo, Kawasaki, Japan), mounted on a swinging arm capable to pivot with a plane precision of ± 1 µm in a range of ~ 2 cm (tested with a precision parallel block of hardened steel (Norelem, Markgröningen, Germany)). The immersion of the rotor under the level of the barrel body plane was thereby measured on 4 different positions with intermediate manual rotation. Planarity of the rotor was less than ±1 µm, parallelism between rotor and the conical steel body (and therefore rotor and sample) was ±1 µm measured at the margins of the rotor. Dry rotation showed that the spindle bearing arrangement and the sealing produced heat, causing a thermal elongation of the rotor of ~ 5 µm after 1 min of rotation at full speed. In contrast, 10 min of rotation at full speed (5400 RPM) in TBS-buffer solution at room temperature without liquid exchange lead to a tolerable thermal drift of gap size smaller than 2 µm.

Rotating speed $\widetilde{\Omega}$: The rotating speed could be adjusted between ~ 80 RPM and 5400 RPM. The used motor (BLDC 58, Mclennan servo supplies, Surrey, UK) is equipped with a 36 pulses per round sensor system. Rotating speed was displayed on a pulse counter and could be adjusted with a precision of less than 2 RPM.

Volume flux $\widetilde{Q}$: Radial flow was controlled by the gas pressure measured before the liquid reservoir, which was approximately 0.2 atmospheres. Given the diameter of tubing (3 mm for gas and 1 mm for liquid tubes) the pressure loss between the manometer and the active region of the shear device is negligible. The volume flux was measured manually at the outlet using a pipette. This radial contribution to the shear rate is negligible (see section "Fluid dynamics in the gap")

Quantification of stretching: When VWF is adsorbed on the surface under shear conditions various phenomena can be observed, including orientation, disentangling of the chains and elongation. As a parameter to describe all this effects the quotient of maximum one-dimensional length and contour length is used, in the following referred to as "stretching parameter". Figure 3 shows exemplary the determination of the stretching parameter of one individual oligomeric VWF molecule. The stretching parameter essentially describes the linearity of such a chain like molecule, although it also contains indirect information concerning the elongation insofar as linearity is a precondition for stretching and therefore an increase of contour length was observed only in cases with stretching parameters near to 1. Although elongation could be interesting for biological considerations concerning functionality of VWF, linearity was identified as a more reproducible parameter for semi quantitative analysis of wall shear rates.

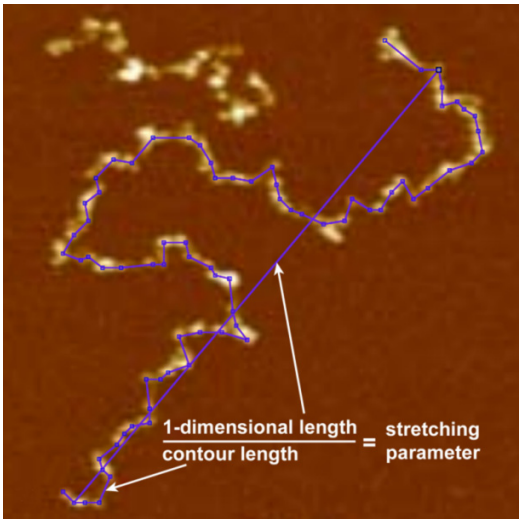


FIG. 3. The image shows exemplary the determination of contour length and maximal 1-dimensional length of a sensor molecule. The quotient of the lengths of the straight line and the contour line is the stretching parameter. This is indicative for the linearity and therefore a measure for stretching of VWF.

AFM-imaging: All AFM images where recorded in tapping mode (TM) with a NanoScope V (Bruker, Santa Barbara, CA, USA) using etched single crystal silicon probes (NCH from Nanoworld, Neuchatel, Switzerland) with a spring constant of 42 N/m. Images where taken with setpoints corresponding to a damping of approximately 90% of the free amplitude. Images were recorded at 3 mm distance from the rotation center. Image size was 10 µm x 10 µm, each image showed a minimum of 120 molecules. For determination of an average local stretching parameter all molecules which were totally inside a 5 µm x 5 µm square (centered on the image) were taken into account.Three independent samples for each shear rate were analyzed.

Sources of recombinant VWF. Recombinant VWF lots used in this study were prepared under identical conditions as described in Bonazza et al. 21. All AFM studies were conducted with the rVWF lot HN02R00

## III. THEORETICAL PART - FLUID DYNAMICS IN THE GAP

For targeting the scope of this study it is crucial to maintain well-defined and fully understood flow conditions in the active region of the gap lumen were shear-force-indicating stretching of sensor molecules takes place. The following classical fluid dynamical considerations make clear that, within a certain range of parameters, the situation in the gap can be nicely approximated as an ideal coquette flow and therefore, the shear rate can be calculated as velocity divided by the gap width. At the parameters which have been chose for the experiments no turbulence, flow inversion or significant heating is expected.

### A. Reference and dimensionless quantities

The fluid feeding the gap is a highly diluted aqueous buffer solution of sensor molecules. The flow can be handled as incompressible and isoviscous, justified by the almost constant temperature. Hence, the region of fully developed flow is governed by seven input parameters: gap height $\tilde{H}$ and rotational speed $\tilde{\Omega}$ of the top plate (Figure 2b), pressure controlled volume flux $\tilde{Q}$ and the ambient temperature Ta. Characteristic values of these quantities as well as the linear thermal expansion coefficient of the steel (alpha) and the diameter d of the hose, are shown in Table I. It should be mentioned that the atomically flat mica surface of the stationary (top) disc can be viewed as perfectly smooth and the polished one of the rotating (bottom) disc having grooves of several μm in width and depth as sufficiently ( i.e. hydraulically) smooth. The effect of the twisting-tumbling motion of the upper disc due any small but unavoidable horizontal misalignment of the discs, perturbing their nominal distance $\tilde{H}$, on the flow then can be ignored. Moreover, as a consequence of the reasonable neglect of any swirl motion in the feed flow, this is treated as axisymmetric as long as the potential onset of turbulence is delayed far enough downstream from the observed surface area.

Both points are confirmed below. Having chosen an appropriate reference radius $\tilde{R}$, the characteristic value of the radial flow speed (U) near $\tilde{r} = \tilde{R}$ and the mean flow speed in the hose (Uh) are given by the imposed volume flux $\tilde{Q}$

$$\tilde{Q} := 2\pi\tilde{R}\tilde{H}\tilde{U} = \pi\tilde{d}^2\tilde{U}_h/4. \tag{1}$$

By dimensional analysis, the relevant dimensional input parameters $\tilde{Q}, \tilde{\Omega}, \tilde{R}, \tilde{H}, \tilde{\nu}$ are converted in the equivalent four non-dimensional groups: aspect ratio Є, Reynolds number ReЄ (reduced by $\epsilon^2$), Rossby number Ro, Eckert number Ec,

$$\epsilon := \tilde{H}/\tilde{R}\,,\ \mathrm{Re}_\epsilon := (\epsilon^2\,\tilde{U}\tilde{R})/\tilde{\nu}\ ,\ \mathrm{Ro} := \tilde{U}/(\tilde{\Omega}\,\tilde{R}),\ \mathrm{Ec} := (\tilde{\Omega}\tilde{R})^2/\tilde{c}\mathrm{T_a}. \tag{2}$$

Let $\tilde{t}$, $\tilde{r}$, $\tilde{z}$ , $\tilde{u}$ , $\tilde{t}$, $\tilde{w}$, $\tilde{T}$ (in the specific order) denote the time, coordinates in radial and vertical directions, the components of the fluid velocity in the r-, the circumferential, and the z-direction and the fluid temperature. We introduce the non-dimensional variables

$$\mathrm{t} := \tilde{t}\,\tilde{\Omega}\,,\ \mathrm{r} := \frac{\tilde{r}}{\tilde{R}},\ \mathrm{z} := \frac{\tilde{z}}{\tilde{H}},\ [\mathrm{u},\mathrm{w}] := \frac{[\tilde{u},\tilde{w}]}{\tilde{U}},\ \mathrm{v} := \frac{\tilde{v}}{\tilde{\Omega}\tilde{R}},\ \mathrm{p} := \frac{\tilde{p}}{\tilde{\rho}\tilde{U}^2}, \Theta := \frac{\tilde{T}}{\tilde{T}_a}. \tag{3}$$

### B. Problem formulation and order-of-magnitude estimates

We fix the reference radius $\widetilde{R}$ by setting

$$\mathrm{Re}_{\epsilon} = \mathrm{Ro}^2 \quad \widetilde{R} = \sqrt{\tilde{\nu}\widetilde{Q}/(2\pi\widetilde{H}^3\widetilde{\Omega}^2)} \tag{4 a,b}$$

then follows from (1) and (2). Considering $\widetilde{R}$ as function of $\widetilde{Q}$ and $\widetilde{\Omega}$ yields the potential range of its reference values. These are added to Table II together with its effective radius used in the experiments (highlighted); the resulting ones for the dimensionless groups given in (2) are $\in, \mathrm{Re}_{\in}, \mathrm{Ro}, \mathrm{Ec}$. It is found that at a distance from the center measured by $\widetilde{R}$ the basic assumptions for a fully developed flow in a thin gap

$$\epsilon \ll 1, \ \mathrm{Re}_{\epsilon} \ll 1, \tag{5 a,b}$$

i.e. negligibly small pressure variations across the gap, and vanishingly small inertial effects (Stokes or creeping flow), are perfectly met. Hence, the specific definition (4b) suitably fixes the section of measurements and so provides the basis for the proposed design of the apparatus.

TABLE II. Constant experimental parameters.

| Thermal coef. steel<br>α<br>[10-6 K-1] | Diameter of tubings<br>d<br>[mm] | Gap width<br>H<br>[μm] | Temperature<br>Ta<br>[°C] | Prantl number<br>Pr<br>[ ] | Radius of sampling<br>R<br>[mm] |
|---|---|---|---|---|---|
| 11.5 | 1 | 30 | 20 | 6.99 | 3 |

This scenario holds indeed if, simultaneously, laminar–turbulent transition is safely avoided for $\tilde{r} < \widetilde{R}$. We note that in a fully developed slender shear layer the, this process controlling, Reynolds number is formed with the typical layer thickness, thus here given by $\mathrm{Re}_{\mathrm{H}} := (\widetilde{U}\widetilde{H})/\tilde{\nu} \ = \mathrm{Re}_{\in}/\epsilon$, and has to be kept distinctly below a critical threshold, typically of order 103. In this sense, transition is suppressed in the feed hose if there the corresponding Reynolds number $\mathrm{Re}_{\mathrm{d}} := \widetilde{U}_{\mathrm{h}}\tilde{d}/\tilde{\nu}$ stays markedly below its well-known critical value of about 2250. From (1) then follows

$$\mathrm{Re}_{\mathrm{d}} = 4\widetilde{Q}/(\pi\tilde{d}\tilde{\nu}) \ < 2250, \ \mathrm{Re}_{\mathrm{H}} \ = \mathrm{Re}_{\mathrm{d}}\tilde{d}/(8\widetilde{R}) \ \ll \mathrm{Re}\,. \tag{6}$$

which justifies issue (i) above.

Governing equations: Inspection of the Navier-Stokes equations shows that in the limits indicated by (5), these equations reduce to those describing an axisymmetric radial Poiseuille flow which, due to the choice (4b) of $\widetilde{R}$, is subjected to a pronounced centrifugal force as it is one-sidedly coupled with a Couette flow in the azimuthal direction. It is practically of great value that varying $\widetilde{Q}$ and $\widetilde{\Omega}^2$ proportionally means mechanical similarity of the flow for a given kinematic configuration. Specifically, substitution of the leading order approximations $[u, v, w] \sim [U, V, \in W](r, z), p \sim Re_{\in} P_{(r)}$ yields the (parameter-free) simplified momentum equations

$$U_{zz} = P' - V^2/r,\ V_{zz} = 0. \tag{7 a,b}$$

These are supplemented with the boundary conditions

$$U(r, 0) = U(r, 1) = 0,\ V(r, 0) = 0,\ V(r, 1) = r \tag{8}$$

and the requirement of mass conservation in the radial direction according to (1),

$$\int_0^1 rU(r, z)dz = 1 \tag{9}$$

which determines P(r). The w-component of the flow velocity follows from the solution of (7) – (9) by integration of the continuity equation

$$(rU)r + rW_z = 0. \tag{10}$$

### C. Wall shear rates and radial flow

From (7) and (8), we have

$$U = -P'(r)z(1 - z)/2 + rz(1 - z^3)/12,\ V = rz. \tag{11a,b}$$

The asymmetry of U in z with respect to $z = 1/2$ becomes explicit when the flow is considered in a frame of reference rotating with $\widetilde{\Omega}/2$: there the skew-symmetric contribution $rz(1-z)(2z-1)/12$ to U originates in the r-component of the Coriolis acceleration $-r(z-1/2)$ then entering the right-hand side of (7a). By (9), we obtain $1 \sim -[p'(r) - 3r/10]\ r/12$ whence

$$P(r) - P(1) = 3(r^2 - 1)/20 - 12\ln r. \tag{12}$$

Therein and consequently in (11a) and the subsequent depending results two contributions relevant for small and large values of r, respectively, are recognized; the latter reflecting the, with r increasing impact, of the centrifugal force in (7a).

Although the concept of this stretching device is to achieve a Couette flow, for practical reasons a certain feed flow was necessary, resulting in a small radial flow component. It was crucial to keep the flow in a suitable range. The lower limit of radial flow is given by the indispensable cooling function of the liquid and the short desired residence time of sensor molecules in the gap, while the upper limit is marked by flow reversal and a substantial aberration from the Couette flow.

The possibility of backflow can be estimated taking into account the non-dimensional wall shear rates in r-direction, $\tau_o \coloneqq U_z(r,0)$ and $\tau_0 \coloneqq U_z(r,1)$, follow from (10a) and (11) as

$$\tau_0 = -P'(r)/2 + r/12 = 6/r - r/15, \quad \tau_1 = P'(r)/2 - r/4 = -6/r - r/10. \tag{13}$$

Hence, the flow is strictly forward upstream of flow reversal at the stationary (lower) wall as typical of creeping slender-gap flows and occurring for

$$\tilde{r} \gtrsim \tilde{r}_c \coloneqq \sqrt{90}\widetilde{R}. \tag{14}$$

As a crucial finding, the operation can be taken as reliable only for values of $\tilde{r}$ considerably smaller than the critical radius $\tilde{r}_{crit}$. This was considered in the experimental setup by collecting images at $\tilde{r}$ = 3 mm, which is 5 times smaller than the radius of beginning asymmetry (Figure 4). Moreover, the resulting ratios of the wall shear rates in the r- and in the azimuthal direction given by $Ro\ \tau_0/r, Ro\ \tau_1/r$, according to (2), are in the order of $(Re_\epsilon^{1/2})$ and thus small owing to (4a) and (5b).

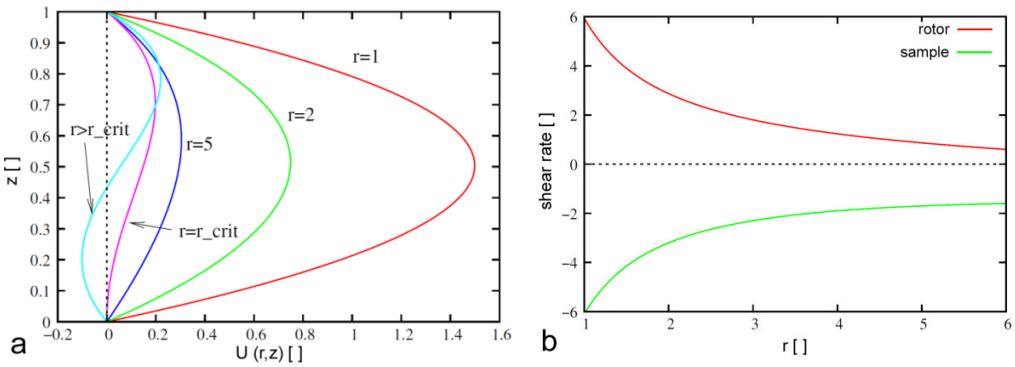


FIG. 4. Symmetry of flow. a) The dimensionless flow profile reveals the upper limit of possible radii for data collection. Notable asymmetry and flow reversal (at r > rcrit) is solely occurring at radii 5 times larger than the reference radius of 3 mm used for our experiments. b) Dimensionless shear rate at the boundaries of rotor and sample, plotted as a function of the radius r. The slight asymmetry derives from the influence of radial flow.

## IV. Results and Discussion

Figure 5a shows VWF chains adsorbed at a shear rate of 22,000 $s^{-1}$. They were just slightly affected from shear forces showing a stretching parameter of 0.55, which is very close to that of sensor molecules adsorbed under static conditions (shear rate 0 $s^{-1}$, stretching parameter 0.5). By stepwise increasing the shear rate to 29,500 $s^{-1}$ (Figures 5 b-d) more and more molecules were stretched, resulting in stretching parameters up to 0.73. A further stressing of the sensor molecules at 32,000 $s^{-1}$ led to nearly uncovered mica surfaces, probably due to a rupture of molecules, representing the upper limit of shear rates detectable with this method. It should be mentioned that sensor molecules, once they are disentangled can undergo a real elongation, meaning that they increase their contour length. Although, this elongation seems very interesting in terms of their biomechanical properties, in the context of shear rate sensing we focus on the linearity and the degree of disentangling of chains which are described by the stretching parameter. The dependence of the stretching parameter from the shear-rate is depicted in Figure 5f.

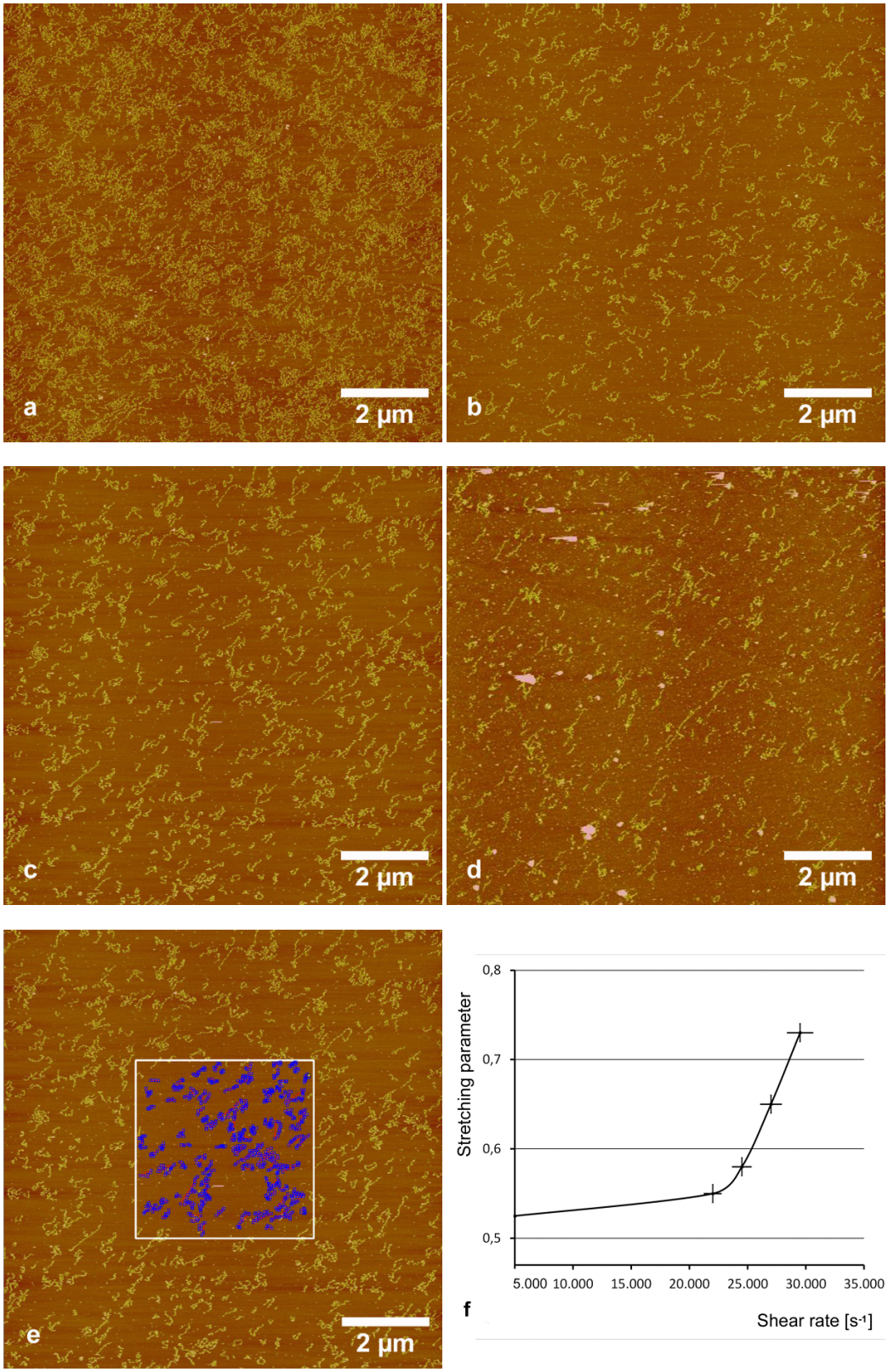


FIG. 5. VWF stretched at increasing shear rates. Characteristic AFM-images from one of 3 independent experiments. Molecules in a) 22,000 $s^{-1}$ are just slightly affected by the sheared liquid, in b) (24,500 $s^{-1}$) and c) (27,000 $s^{-1}$) molecules are unravelled and oriented in flux

direction. An increase to 29,500 $s^{-1}$, shown in d) caused linearization and elongation. e) In order to demonstrate the 5 µm localization of shear rate measurement, 5 µm x 5 µm spots were used to determine an average stretching parameter as shown here exemplary. Contour lengths and maximal one-dimensional extensions of molecules was determined using datalab (see also experimental, Figure 3). All images show a certain background of small dots which are VWF fragments. In f) the shear rate dependence of the stretching parameter (ratio between the maximum dimension and the contour length) is plotted. For each data point at least 90 molecules were evaluated, which derived from 3 independent experiments, giving the vertical error range. Horizontal errors are determined by the tolerance of gap width. Height scale: 5 nm from dark to bright.

The theoretical fluid dynamical considerations results in a nearly azimuthal flow direction (small Rossby numbers, small tilting angle θ) and proves the applicability of the Couette flow approximation, which was used for calculating shear rates (Table I). However, sensor molecules shown in Figure 5 have much higher θ indicating that they are not totally aligned to the flow trajectories. This can be explained by the short residence time of molecules in the active gap region and the small aspect ratio $\tilde{H}/\tilde{R}$ of the µm-scaled gap ($\tilde{H}$ is just 10 times the length of a sensor molecule), both allowing just a partial re-orientation of chains which were exposed to radial acceleration forces in the center/feed region some milliseconds before. Moreover, the orientation of images relatively to the azimuthal axis was just roughly adjusted with a precision of ± 15° and therefore, the shear rates should be interpreted as scalars, tentatively a raw and qualitative, directional information could be extracted. From a nano-mechanical point of view, the question may arise, where deformation of sensor molecules takes place, at the surface or in free flowing liquid and at which z-Position? Regarding the first option it should be mentioned that adhesion of sensor molecules to the mica surface is too weak for proper AFM scanning in liquid, even by the use of tapping mode with the less invasive parameters (displacement of molecules). This problem has been affronted in numerous studies and is usually circumvented by chemical surface modifications 22, 23 or imaging in air 21, hence, the lack of strong attractive forces between untreated mica and protein molecules is well known. Therefore, our model considers stretching of passively transported sensor molecules by the velocity gradient in the carrying liquid followed by a subsequent deposition on the surface. It is worth noting that an infinitely small particle/molecule, once in contact with the surface, would be trapped due to the boundary condition and therefore virtually adhered to the surface for a diffusion controlled time. In contrast to that, sensor molecules used in this study circulate in liquid as loosely coiled chains with an average sphere-diameter of ~90 nm as shown by dynamic light scattering 16. The question at which z-distance from the surface the deformation occurs cannot be answered experimentally in this context, however, the variation of shear rate in z-direction is negligible as it is solely caused by the very small radial component of flow. Figure 6 shows the distribution of shear rate (as a scalar) in the gap with strongly overscaled (by factor of 10) radial component. Due to this almost linear velocity profile (nearly perfect Couette flow) the z-origin of deposited, stretched molecules is uncritical.

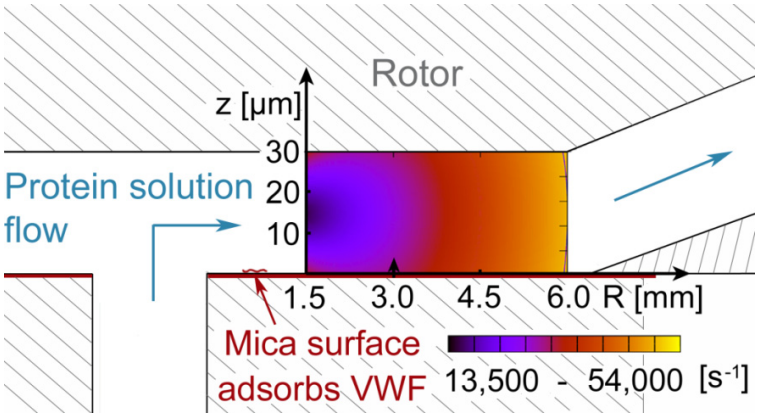


FIG. 6. Calculated distribution of shear-rates in the gap shown exemplary for sample shown in Figure 5 c. The radial component is exaggerated for visibility by setting the Rossby number to 0.1. Despite this overdrawn influence of radial motion, the variation of shear rate in z-direction at the relevant radius of 3 mm (used for taking images, marked by an arrow) is small. At this radius the wall shear rate is 27,000 $s^{-1}$.

The image sections used for the determination of the stretching parameter had a size of 5 µm x 5 µm and still showed a minimum of ~ 30 molecules which was necessary for a statistical evaluation. On the one hand reliability of shear rate measurements depends on the number of evaluated molecules, and on the other hand an exaggerated aerial density of molecules would create interpretation problems due to frequently overlapping chains and thus a certain minimal size of analyzed images is indispensable. Our results show that the image-size / localization-precision of 5 µm is sufficient for a reproducibility corresponding to a stretching parameter variation of ± 0,01.

## V. Outlook

This prove of principle study for shear rate measurement with sensor molecules can now be applied to more complicated geometries with less known flow conditions, always using the described, or an equally simple geometry, as a calibration reference for the stretching-parameter / shear-rate dependence. In the actual version, this method is limited to a certain range of shear rates, suitable for the used sensor molecules. The use of other types of either biological or synthetic macromolecules as well as a more adhesive coating of the surface could be possible ways to adept this concept to any desired shear rate range.

## VI. Acknowledgments

We acknowledge Alfredo Alexander-Katz (MIT) for fruitful discussions.

## VII. References


1. G. Onsrud, L. Persen and L. Saetran, Experiments in Fluids **5**, 11 (1986).
2. H. H. Winter, Advanced Heat Transfer **13**, 205 (1977).
3. C. Lelièvre, P. Legentilhomme, C. Gaucher, J. Legrand, C. Faille and T. Bénézech, Chemical Engineering Science **57**, 1287 (2002).
4. C. Gillham, P. Fryer, A. Hasting and D. Wilson, Journal of Food Engineering **46**, 199 (2000).
5. A. J. Reininger, H. F. Heijnen, H. Schumann, H. M. Specht, W. Schramm and Z. M. Ruggeri, Blood **107**, 3537 (2006).
6. C. E. Sing and A. Alexander-Katz, Biophysical Journal **98**, L35 (2010).
7. N. Rajaratnam, Water and Energy International **23**, 137 (1966).
8. Z. Wang, Experiments in Fluids **14**, 153 (1993).
9. F. Gijsen, A. Goijaerts, F. Van de Vosse and J. Janssen, Journal of Rheology **41**, 995 (1997).
10. P. Ireland and T. Jones, Measurement Science and Technology **11**, 969 (2000).
11. K. Shirai, presented at the 20th International Congress on Instrumentation in Aerospace Simulation Facilities, (2003).
12. B. B. B. Jensen, A. Friis, T. Bénézech, P. Legentilhomme and C. Lelievre, Food and Bioproducts Processing **83**, 53 (2005).
13. R. Waser, Nanoelectronics and Information Technology, Wiley (2012).
14. U. Ulmanella and C.-M. Ho, Physics of Fluids **20**, 101512 (2008).
15. M. Harrison, W. Batten, L. Myers and A. Bahaj, IET Renewable Power Generation **4**, 613 (2010).
16. E. Di Stasio, F. Romitelli, S. Lancellotti, A. Arcovito, B. Giardina and R. De Cristofaro, Biophysical Chemistry **144**, 101 (2009).
17. K. Bonazza, H. Rottensteiner, G. Schrenk, C. Fiedler, F. Scheiflinger, G. Allmaier, P. L. Turecek and G. Friedbacher, Analytical and Bioanalytical Chemistry **407**, 6051 (2015).
18. S. Schneider, S. Nuschele, A. Wixforth, C. Gorzelanny, A. Alexander-Katz, R. Netz and M. Schneider, Proceedings of the National Academy of Sciences of USA **104**, 7899 (2007).
19. T. A. Springer, Blood **124**, 1412 (2014).
20. K. Bonazza, H. Rottensteiner, G. Schrenk, J. Frank, G. Allmaier, P. L. Turecek, F. Scheiflinger and G. Friedbacher, Analytical Chemistry **87**, 10299 (2015).

21. K. Bonazza, H. Rottensteiner, B. K. Seyfried, G. Schrenk, G. Allmaier, P. L. Turecek and G. Friedbacher, Analytical and Bioanalytical Chemistry **406**, 1411 (2014).

22. M. Raghavachari, H.-M. Tsai, K. Kottke-Marchant and R. E. Marchant, Colloids and Surfaces B: Biointerfaces **19**, 315 (2000).

23. J. Adamcik, D. V. Klinov, G. Witz, S. K. Sekatskii and G. Dietler, FEBS Letters **580**, 5671 (2006).

Anal Bioanal Chem (2015) 407:6051–6056
DOI 10.1007/s00216-015-8778-z

RESEARCH PAPER

# $Ca^{2+}$ concentration-dependent conformational change of FVIII B-domain observed by atomic force microscopy

**Klaus Bonazza[1] · Hanspeter Rottensteiner[2] · Gerald Schrenk[2] · Christian Fiedler[2] · Friedrich Scheiflinger[2] · Günter Allmaier[1] · Peter L. Turecek[2] · Gernot Friedbacher[1]**

Received: 9 April 2015 / Revised: 7 May 2015 / Accepted: 8 May 2015 / Published online: 23 May 2015
© Springer-Verlag Berlin Heidelberg 2015

**Abstract** FVIII is a multi-domain protein organized in a heavy and a light chain, and a B-domain whose biological function is still a matter of debate. The 3D structure of a B-domain-deleted FVIII variant has been determined by X-ray crystallography, leaving unexplained the functional nature of the flexible B-domain which could play an important role in the structure-function relationship since it is removed during the activation process. To obtain clues on the function of the B-domain, the morphology of full-length FVIII and its isolated domains was determined in the absence or presence of $Ca^{2+}$. Recombinant full-length FVIII, the purified heavy chain, light chain and B-domain as well as B-domain-deleted rFVIII were analysed in buffers of different $Ca^{2+}$ concentrations by atomic force microscopy. In the absence of $Ca^{2+}$, FVIII appeared as a globular molecule, whereas at high amounts of $Ca^{2+}$ up to 50-nm long tail structures emerged. These tails could be identified as unravelled B-domains, as images of isolated B-domains showed the same morphology and heavy chains which include the B-domain were also rich of tails, whereas the isolated light chains and B-domain-deleted FVIII lacked any deviation from a globular shape. The images further suggested that the B-domain interacts with the light chain particularly at low $Ca^{2+}$ concentrations. Our results show a $Ca^{2+}$-regulated conformational change of the B-domain in the context of full-length rFVIII. As the B-domain tightly associated with the core of the FVIII molecule under low $Ca^{2+}$-concentrations, a stabilizing function on FVII I under non-activating conditions may be proposed.

**Keywords** Atomic force microscopy · Blood · Factor VIII · Thrombosis · Structure-function relationship · $Ca^{2+}$ dependence

**Electronic supplementary material** The online version of this article (doi:10.1007/s00216-015-8778-z) contains supplementary material, which is available to authorized users.

✉ Gernot Friedbacher
gernot.friedbacher@tuwien.ac.at

[1] Institute of Chemical Technologies and Analytics, Vienna University of Technology, Getreidemarkt 9/164-IAC, 1060 Vienna, Austria

[2] Baxter Innovations, Industriestraße 67, 1221 Vienna, Austria

## Introduction

Factor VIII (FVIII) is an essential compound in the activation cascade of secondary haemostasis and therefore critical for blood clotting. The sequence and posttranslational modifications of FVIII are well-defined [1] and an X-ray structure of a B-domain-deleted (BDD)-FVIII product at a resolution of 3.7 Å is available [2]. FVIII is a glycoprotein with a discrete domain structure of A1-a1-A2-a2-B-a3-A3-C1-C2. It is composed of a heavy chain (HC) consisting of the domains A1-a1-A2-a2-B, which is connected by a copper ($Cu^{+}$) bridge to a light chain (LC), containing domains a3-A3-C1-C2. While $Cu^{+}$ primarily enhances the intersubunit affinity, calcium ($Ca^{2+}$) appears essential to promote the active conformation of factor VIII [3] by playing a role in the maintenance of the C2-A1 domain interface [4]. The B-domain carries the majority of glycosylations (mainly N-linked). The B-domain is not directly necessary for the central procoagulant activity of FVIII [5, 6] as BDD variants of FVIII fully serve their role in the tenase complex [5]. More recently, the B-domain has been shown to play a major role in the intracellular processing and trafficking of FVIII. Moreover, there is emerging evidence that portions of the B-domain may have functional influences throughout the life cycle of FVIII [7]. The B-domain may affect receptor-linked endocytosis [8], the affinity of

FVIII to activated platelets [9], and it may render FVIII-decorated phospholipid surfaces less hydrophobic, thereby preventing aggregation of vesicles [10]. More insights into the role of the B-domain would not only be important for our understanding of FVIII biochemistry but also to learn more about potential differences between recombinant (r) BDD-rFVIII and full-length rFVIII products, including B-domain-functionalized long-acting FVIII variants [11, 12].

While the structure of BDD-FVIII is largely resolved [2], much less is known about the B-domain. Our understanding of FVIII functionality goes back to Mosesson et al. who investigated porcine FVIII to prove that FVIII exhibits its co-factor activity only after being activated by thrombin. This process includes cleavage of the heavy chain at residues 372 and 740 and the light chain at position 1689, which is accompanied by an elimination of the B-domain [13]. The authors detected by means of transmission electron microscopy (TEM) that in some cases the negatively stained (uranyl sulphate) porcine FVIII specimen contained a vaguely visible short (14 nm) tail structure, which they assigned to be the B-domain. This was confirmed by Fowler et al. who presented images of human plasma-derived FVIII with slightly discernible, 50-nm long tails using a positive staining preparation (platinum grains) for contrast generation in TEM [14]. Both studies mainly focussed on the large sequence homology between FVIII and Factor V (FV). Based on the single chain nature of non-activated FV and the high homology between FV and FVIII, the latter work suggested a double stranded rod-like shape of the B-domain.

Here, the image of FVIII's B-domain was further elucidated by atomic force microscopy (AFM) using full-length rFVIII, isolated fragments thereof (heavy and light chains, B-domain) and as a control BDD-rFVIII. In contrast to TEM, molecules were not treated with any staining agents and gently deposited on an inert mica surface in order to keep the substrate's influence as low as possible. Our previous studies indeed confirmed that protein molecules such as FVIII and VWF largely keep their specific properties (e.g. reactivity between VWF and FVIII) under such mild imaging conditions [15]. The high resolution and low invasiveness at atmospheric pressure of AFM allowed clear imaging of FVIII molecules and isolated fragments. A calcium-dependent transition from a coiled to an unravelled tail structure of the FVIII B-domain could be observed.

## Experimental

**Sources of proteins and fragments** Two different, commercially available rFVIII products were investigated: a full-length rFVIII, ADVATE® (Baxter, Vienna, Austria) and a B-domain-deleted rFVIII, Refacto AF® (Pfizer, Kent, UK). The FVIII B-domain was prepared by thrombin cleavage of full-length rFVIII and subsequent isolation by size exclusion chromatography. The heavy and light chains were isolated by dissociation of the FVIII heterodimer and subsequent purification by conventional chromatography.

SDS–PAGE and Western blot analysis under non-reducing conditions were used to check for the purity of the fragments. Polyclonal sheep anti-human FVIII antibodies (Cedarlane, Burlington, CA) were used for the detection of all FVIII fragments, whereas monoclonal mouse antibodies were used to specifically identify the heavy chain (AbD Serotec, Puchheim, Germany), the light chain (QED Bioscience, San Diego, CA) and the B-domain (AbD Serotec). Visualization of fragments was achieved with alkaline phosphatase staining and employing appropriate secondary antibodies (see Electronic Supplementary Material (ESM) Fig. S1).

**Sample preparation** All proteins were immobilized on untreated, freshly cleaved mica by 5-min adsorption from Tris-buffered saline (TBS) buffer containing 150 mM NaCl (Sigma-Aldrich, St. Louis, MO, USA) and subsequent short rinsing with water. In some experiments, $CaCl_2$ ($CaCl_2 \times 2\ H_2O$, 99 %, Sigma-Aldrich) was added as indicated in the text. In those cases where no $CaCl_2$ was used, 50 μM ethylenediaminetetraacetic acid (EDTA; p.a., Merck, Darmstadt, Germany) was added in order to complex traces of $Ca^{2+}$ from the production process. Incubation of the rFVIII light chain with the B-domain was performed in a thermostatic bath at 30 °C for 7 min.

**AFM imaging** All AFM images where recorded in tapping mode (TM) with a NanoScope V (Bruker, Santa Barbara, CA, USA) using etched single crystal silicon probes (NCH from Nanoworld, Neuchatel, Switzerland) with a spring constant of 42 N/m, driven by small amplitudes of 50–120 mV. The images were flattened using the Nanoscope software version v7.1.30. The contour lengths of the B-domains were determined by manually drawing tracking points along the contour using Datalab version 3.5.30 (Epina, Pressbaum, Austria, http://datalab.epina.at).

## Results and discussion

Recently, we described in a different context that full-length rFVIII molecules are generally spherical [15]. However, a more detailed view revealed that some molecules are composed of core globular units with serpentine tail structures with contour lengths of approximately 50 nm and containing a series of small knots (Fig. 1a). Figure 1b shows isolated B-domains. They appear either globular or unravelled with contour lengths of up to 50 nm and a texture very similar to that of the rFVIII tails. In Fig. 1c, rFVIII heavy chains are shown. A majority of them has attached tail structures indicative for B-

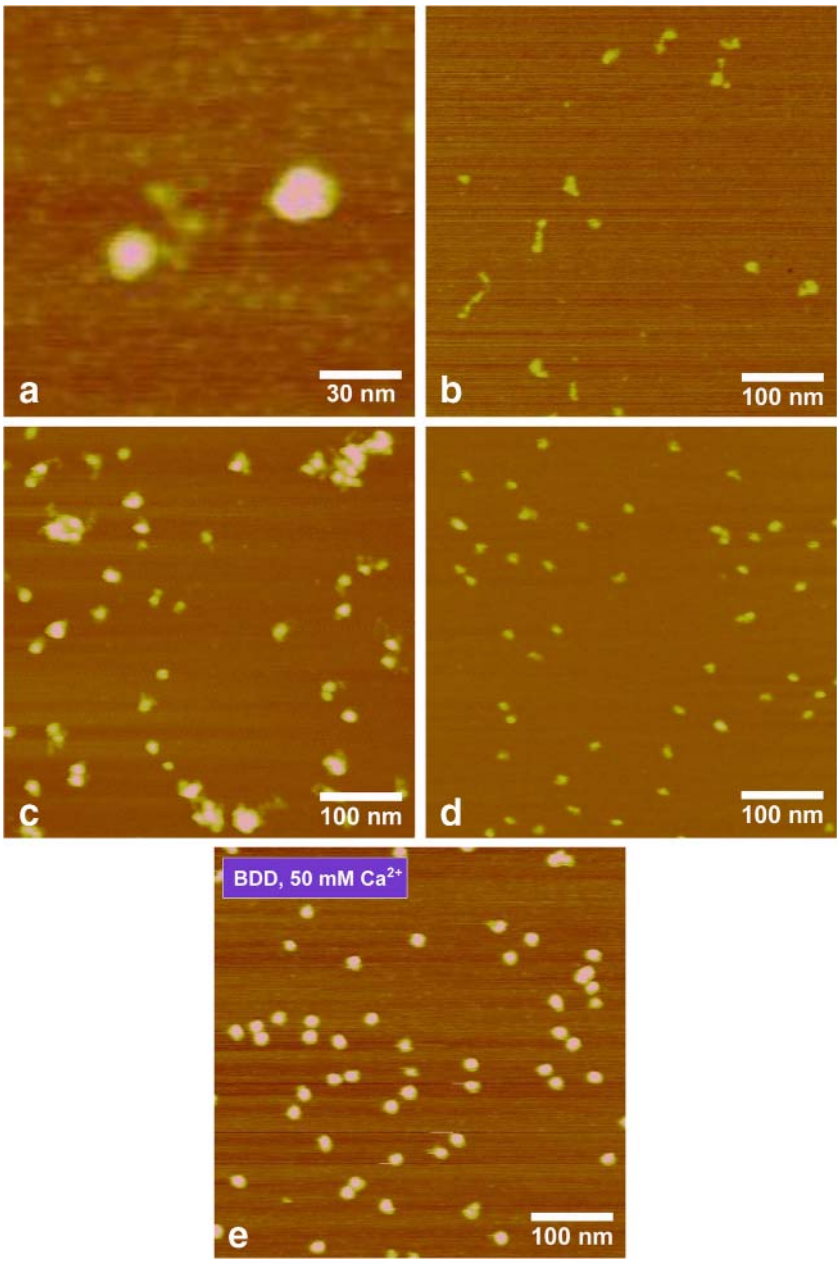


**Fig. 1** Morphology of full-length FVIII and its fragments. **a** Full-length FVIII molecules can be either globular or consist of a core globular unit with an attached tail-like structure which can be assigned to the B-domain. **b** Isolated FVIII B-domains. **c** Isolated heavy chains. A certain size distribution due to some agglomeration can be observed. The tail-like, variable B-domain appears unrolled in a great number of molecules. **d** Isolated light chains. Here, the shape is largely spherical, and all molecules have approximately the same size. **e** BDD-FVIII has a globular shape and a narrow size distribution with virtually no tail structures. In very few cases, agglomeration can be observed. **a**, **b** and **c** were absorbed from a $Ca^{2+}$-free buffer. **d** and **e** were previously exposed to 50 mM $Ca^{2+}$, confirming that the topography of the isolated light chains and the BDD-FVIII did not change compared to absorption from $Ca^{2+}$-free solution (data not shown). Height scale: 3 nm from dark to bright

domains, whereas the isolated light chains, visualized in Fig. 1d, do not show any significant deviations from a globular structure. Finally, Fig. 1e shows the B-domain-free rFVIII variant which is used as a control as it entirely lacks the B-domain; again, no tail structures are visible. From these observations, we conclude that the tail structures are indeed B-domains.

Since $Ca^{2+}$ is a crucial factor in the activation of coagulation, its effect on the morphology of FVIII was studied by exposure of full-length rFVIII to buffers with increasing $Ca^{2+}$ concentrations (Fig. 2). Under exclusion of $Ca^{2+}$ (even traces of $Ca^{2+}$ from the formulation were eliminated using a sixfold excess of EDTA), only 6±3 % of full-length rFVIII showed tail-like structures (Fig. 2a). The number of tails increased to 14±5 % in the presence of 5 mM calcium (Fig. 2b) and even further to 42±8 % at 50 mM $Ca^{2+}$ (Fig. 2c) and 46±8 % at 500 mM $Ca^{2+}$ (see summarized data in Fig. 2d). These data clearly demonstrate that the conformation of the B-domain transitions from a tightly associated to a tail-like form upon increasing concentrations of $Ca^{2+}$. For comparison, we have also performed such an experiment with 50 mM $Mg^{2+}$ instead of $Ca^{2+}$, which indicates that the effect of $Mg^{2+}$ on unravelling of the B-domain is significantly weaker (see also Fig. 2d), thereby supporting the prominent role of $Ca^{2+}$.

Notably, in the presence of high $Ca^{2+}$ concentrations, some rFVIII molecules show an additional smaller structure which is apparently situated at the opposite side of the core globular

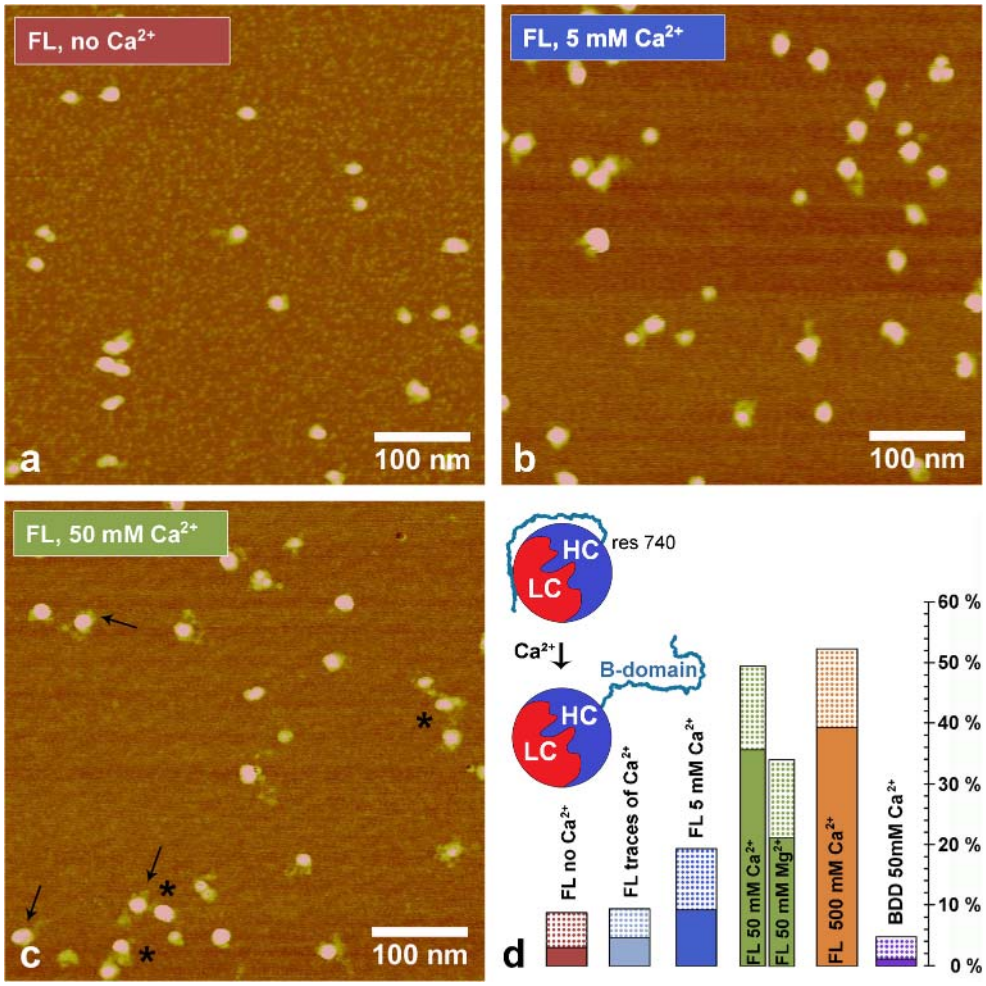


**Fig. 2** Calcium-dependent unfolding of B-domains of full-length (FL) FVIII. **a** FL-FVIII adsorbed from a $Ca^{2+}$-free buffer. Most molecules do not deviate from a globular shape. Tails are rare and typically short and agglomeration is negligible. **b** FL-FVIII adsorbed from a buffer containing 5 mM $Ca^{2+}$. The number of tail structures is slightly increased. **c** FL-FVIII at 50 mM $Ca^{2+}$. The number of tails is significantly increased. Most molecules consist of a globular core structure and a serpentine tail of variable length. In some cases (three of them are marked with arrows), a second, smaller structural feature is visible. Some FVIII molecules marked with asterisks are connected through their B-domains. **d** Statistic evaluation of the numbers of B-domain tails for full-length (FL) FVIII containing different $Ca^{2+}$ concentrations compared to BDD-FVIII at 50 mM $Ca^{2+}$ (control). For comparison, also the effect of $Mg^{2+}$ is shown for a concentration of 50 mM. For each column, more than 150 molecules derived from a minimum of two independent samples were evaluated. The dotted error ranges reflect the uncertainties in interpreting the structures in the AFM images. A t test comparing the lower value of a column with the upper value of the adjacent column revealed a significant difference (confidence level of 95 %) in the fraction of visible B-domains except between traces of $Ca^{2+}$ and 5 mM $Ca^{2+}$. The cartoon depicts our model for $Ca^{2+}$-dependent unravelling of the B-domain. Height scale of images: 3 nm from dark to bright

unit referring to the B-domain (marked with arrows in Fig. 2c). According to the X-ray crystal structure [2], this might be interpreted as the flexible C2-domain; however; this could not be proven directly.

Our high-resolution images support some older studies [13, 14] which also proposed a core globular assembly of A- and C-domains and a "peripheral satellite appendage" representing the B-domain. However, these TEM-based studies did not show isolated heavy chains or B-domain fragments and were limited in terms of resolution. TEM is an ultrahigh-vacuum and partly destructive method which can potentially create deformations or artefacts of molecules [16]. In both studies, specimen was either positively or negatively stained and freeze dried in order to enhance contrast and to achieve a certain fixation. Reproducing these pioneer's images of the 1990s with the resolution of a state of the art AFM under less severe conditions was critical for studying the $Ca^{2+}$-dependent effects described in our present study.

In one of the addressed studies [13], porcine plasma-derived FVIII was used. It would thus be interesting to see if the B-domain of this molecule shows a similar $Ca^{2+}$-triggered conformational change. Pharmaceutical interest in this molecule has risen as a recombinant BDD variant of porcine FVIII which differs in its sequence from human BDD-rFVIII by

16 % [10] is currently handled as a potential alternative in the treatment of patients with acquired haemophilia A [17].

Evidently, calcium stabilized the B-domain in an unravelled conformation, whereas it remained coiled and a part of the globular FVIII structure when $Ca^{2+}$ was lacking, as shown in the cartoon of Fig. 2d. The isolated heavy chain has also been imaged using different $Ca^{2+}$ concentrations. However, in this case, the B-domain always appeared unrolled, independent from the $Ca^{2+}$ concentration (data not shown). This observation vaguely indicates that the tight packing of the B-domain of full-length rFVIII under $Ca^{2+}$ exclusion was caused by an intramolecular interaction with the light chain. To attain further evidence for this hypothesis, the rFVIII light chain was mixed with the isolated B-domain in the presence or absence of $Ca^{2+}$ ions. Figure 3 shows the mixture after incubation and adsorption on the mica substrate. Besides worm-like chains, indicative for B-domains (see Fig. 1b) and spherical structures which can be interpreted as light chains (see Fig. 1d), a significant fraction of globular structures with attached tail-like structures could be observed. Apparently, the B-domains were associated with the light chains. This interaction was $Ca^{2+}$-dependent in that the samples containing no $Ca^{2+}$ showed attachment of B-domains to light chains most frequently, whereas already small amounts of $Ca^{2+}$ significantly reduced this interaction. In support of a B-domain-light chain interaction, in some cases, two or more rFVIII molecules seemed to be connected/to interact with each other by their B-domains (marked with asterisks in Fig. 2c).

We hypothesize that in the circulation, the B-domain of intact full-length rFVIII contributes to a stabilization of the molecule

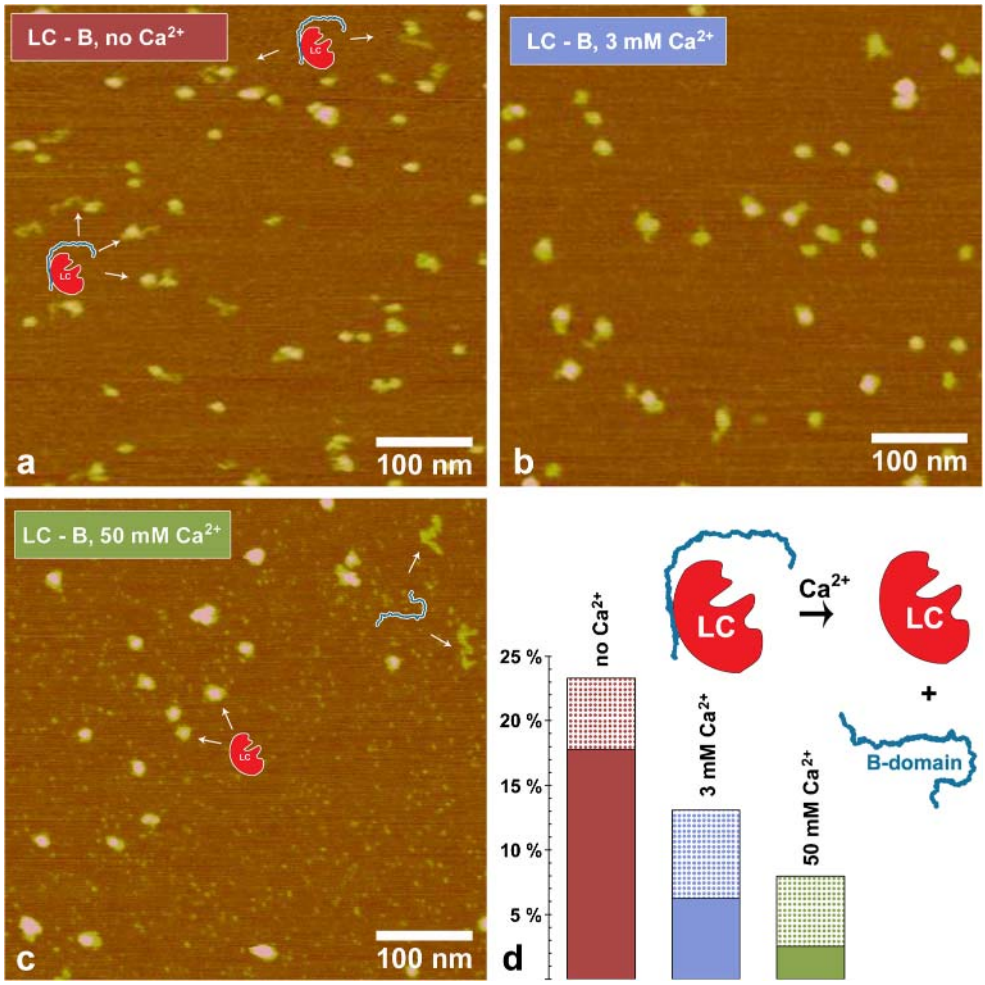


**Fig. 3** Calcium-dependent interaction of FVIII light chain and B-domain. The images show mixtures of light chains and B-domains that had been incubated in the presence of the indicated $Ca^{2+}$ concentrations prior to adsorption. **a** Incubation in $Ca^{2+}$-free buffer. Features consisting of globular dots (light chains, LC) and dangling tails (B-domains) can be observed (some of them are marked), indicating LC–B interactions. At 3 mM $Ca^{2+}$ shown in **b**, the number of such LC–B composites is slightly decreased, and at 50 mM $Ca^{2+}$ shown in **c**, only separated B-domains and LCs are visible and overall, only residual interaction is discernible. **d** Statistic evaluation of the numbers of B-domain tails attached to light chains. The dotted error ranges reflect the uncertainties in interpreting the structures in the AFM images. A *t* test comparing the lower value of a column with the upper value of the other columns revealed a significant difference (confidence level of 95 %) in the fraction of LC–B interactions between "no $Ca^{2+}$" and 3 as well as 50 mM $Ca^{2+}$. The cartoon depicts our model for $Ca^{2+}$-dependent LC–B interactions. Height scale of images: 3 nm from dark to bright

by its association with the light chain at low $Ca^{2+}$ concentrations (see cartoon in Fig. 2d). According to this model, the B-domain would get wrapped around the FVIII core globular unit, thereby shielding it from interactions with thrombin and FIX at physiological concentrations of ionized $Ca^{2+}$ of ~1 mM [18]. Under increased $Ca^{2+}$ concentrations, e.g. on the surface of activated platelets which secrete $Ca^{2+}$, this stabilization bails out and the FVIII gets more vulnerable to activation. Following on that thought, the kinetics of activation of full-length FVIII could be slower compared to BDD-FVIII, as removal of the B-domain through thrombin cleavage at residue 740 would require a preceding $Ca^{2+}$-dependent conformational change. This is supported by studies showing that the B-domain possibly shields the thrombin activation site from premature proteolysis [7].

## Conclusion

Our results not only further elucidate the model of how the rFVIII heterodimer is assembled due to higher image resolution and less denaturating conditions of image generation by using AFM but also revealed a yet unknown $Ca^{2+}$-dependent conformational change of the B-domain. This observation may also help to understand differences between BDD-rFVIII and FL-rFVIII products as well as the effect of functionalization (e.g. PEGylation), which is predominantly affecting the B-domain. More detailed studies on the effect of other cations on the conformation of the B-domain and the nature of the interaction of the B-domain with the FVIII light chain are underway.

**Conflict of interest** H. Rottensteiner, G. Schrenk, C. Fiedler, F. Scheiflinger and P. L. Turecek are full time employees at Baxter Innovations. K. Bonazza, G. Allmaier and G. Friedbacher declare that they have no conflict of interest.

## References


1. Lenting PJ, Van Mourik JA, Mertens K (1998) The life cycle of coagulation factor VIII in view of its structure and function. Blood 92(11):3983–3996
2. Shen B, Spiegel P, Chang C, Huh J, Lee J, Kim J, Kim Y, Stoddard B (2008) The tertiary structure and domain organization of coagulation factor VIII. Blood 111(3):1240–1247
3. Wakabayashi H, Koszelak ME, Mastri M, Fay PJ (2001) Metal ion-independent association of factor VIII subunits and the roles of calcium and copper ions for cofactor activity and inter-subunit affinity. Biochemistry 40(34):10293–10300
4. Ngo JCK, Huang M, Roth DA, Furie BC, Furie B (2008) Crystal structure of human factor VIII: implications for the formation of the factor IXa-factor VIIIa complex. Structure 16(4):597–606
5. Toole JJ, Pittman DD, Orr EC, Murtha P, Wasley LC, Kaufman RJ (1986) A large region (approximately equal to 95 kDa) of human factor VIII is dispensable for in vitro procoagulant activity. Proc Natl Acad Sci U S A 83(16):5939–5942
6. Fay PJ (1993) Factor VIII structure and function. Thromb Haemost 70:63–67
7. Pipe SW (2009) Functional roles of the factor VIII B-domain. Haemophilia 15(6):1187–1196
8. Bovenschen N, Rijken D, Havekes L, Vlijmen B, Mertens K (2005) The B-domain of coagulation factor VIII interacts with the asialoglycoprotein receptor. J Thromb Haemost 3(6):1257–1265
9. Li X, Gabriel DA (1997) The physical exchange of factor VIII (FVIII) between von Willebrand factor and activated platelets and the effect of the FVIII B-domain on platelet binding. Biochemistry 36(35):10760–10767
10. Grushin K, Miller J, Dalm D, Parker E, Healey J, Lollar P, Stoilova-McPhie S (2014) Lack of recombinant factor VIII B-domain induces phospholipid vesicle aggregation: implications for the immunogenicity of factor VIII. Haemophilia 20(5):723–731. doi:10.1111/hae.12421
11. Pipe SW (2012) The hope and reality of long-acting hemophilia products. Am J Hematol 87(S1):S33–S39
12. Turecek P, Bossard M, Graninger M, Gritsch H, Höllriegl W, Kaliwoda M, Matthiessen P, Mitterer A, Muchitsch E-M, Purtscher M (2012) BAX 855, a PEGylated rFVIII product with prolonged half-life. Haemostasiologie 32:S29–S38
13. Mosesson MW, Fass DN, Lollar P, DiOrio JP, Parker CG, Knutson GJ, Hainfeld JF, Wall JS (1990) Structural model of porcine factor VIII and factor VIIIa molecules based on scanning transmission electron microscope (STEM) images and STEM mass analysis. J Clin Investig 85(6):1983–1990
14. Fowler WE, Fay PJ, Arvan DS, Marder VJ (1990) Electron microscopy of human factor V and factor VIII: correlation of morphology with domain structure and localization of factor V activation fragments. Proc Natl Acad Sci U S A 87(19):7648–7652
15. Bonazza K, Rottensteiner H, Seyfried BK, Schrenk G, Allmaier G, Turecek PL, Friedbacher G (2013) Visualization of a protein-protein interaction at a single-molecule level by atomic force microscopy. Anal Bioanal Chem 406:1411–1421
16. Mosesson M, Hainfeld J, Wall J, Haschemeyer R (1981) Identification and mass analysis of human fibrinogen molecules and their domains by scanning transmission electron microscopy. J Mol Biol 153(3):695–718
17. Kempton C, Abshire T, Deveras R, Hoots W, Gill J, Kessler C, Key N, Konkle B, Kuriakose P, MacFarlane D (2012) Pharmacokinetics and safety of OBI-1, a recombinant B domain-deleted porcine factor VIII, in subjects with haemophilia A. Haemophilia 18(5):798–804
18. Larsson L, Ohman S (1978) Serum ionized calcium and corrected total calcium in borderline hyperparathyroidism. Clin Chem 24(11):1962–1965

# 10. Summary of Results and their Significance

The results of this thesis were published in the following 4 Papers:

a) "Visualization of a protein-protein interaction at a single-molecule level by atomic force microscopy"
b) "Shear-dependent interactions of von Willebrand Factor with Factor VIII and protease ADAMTS 13 demonstrated at a single molecule level by Atomic Force Microscopy"
c) "Direct measurement of local wall shear rates with micrometer resolution using sensor molecules"
d) "$Ca^{2+}$ concentration-dependent conformational change of FVIII B-domain observed by atomic force microscopy"

(a) Introduces the new methods which were the key for detecting single molecule binding between VWF and FVIII. Two approaches were described, an "indirect approach" and a "single molecule approach". In the indirect approach a correlation between FVIII concentration in a buffer solution and the surface area coverage number after absorbing FVIII on mica was established. Next, FVIII was absorbed on a VWF spiked mica surface. As a part of FVIII bound to VWF, the number of free FVIII molecules absorbed on the surface was decreased. The number of bound FVIII was obtained indirectly by subtracting the free FVIII from the expected FVIII amount. In the single molecule approach a VWF was marked by a nano-scale scratch in the mica surface, which was made by an AFM tip, in order to be retrieved after subsequent treatment, like addition of FVIII or buffer change. In this way images of the same individual VWF molecule were taken before and after reaction with FVIII. FVIII-VWF complex formation and its inhibition by $Ca^{2+}$ could be shown as well as a $Ca^{2+}$ dependent conformational change of VWF. This method was also used for the work represented in paper (b). While the main focus of paper (a) is the methodical aspects, in paper (b) the methods were applied to solve biological questions: How does VWF contribute to shear flow regulation of hemostasis, by elongation of single molecules or by the formation of VWF fibers? Is secondary hemostasis also regulated by shear flow, due to a flow dependency of FVIII binding? In paper (b) VWF was stretched by a custom-made, microfluidic device which is inspired by a 2 plate rheometer. Single, shear stretched VWF molecules remained absorbed on a mica surface and were therefore "frozen" in their elongated conformation. AFM imaging of these stretched VWF chains yielded the first quantitative, experimental data on the dependence of shear rate and stretching of VWF. Next, the reactivity of these stretched chains was tested by adding ADAMTS13 which is well known to cleave VWF under shear. Proteolysis of single VWF molecules could be visualized for the first time. The final application for the single molecule approach was to study FVIII binding to shear-stretched VWF. Partial stretching of VWF did not impair FVIII binding, whereas total stretching lead to depression of FVIII binding. The microfluidic device that was constructed to stretch VWF was published separately (c). It shows that VWF can also be used as sensor molecule to measure local wall shear-rates. Paper (d) describes a $Ca^{2+}$ dependence of the structure of FVIII. The heterodimer FVIII consists of a light chain carrying most functional exosites that are crucial for hemostasis, and a heavy chain of variable size. This

variability of MW is due to a variable B-domain which accounts for a third of the MW. The B domain is not considered to be indispensable for FVIII´s hemostatic activity in fact most therapeutic FVIII products lack the B-domain. As described in paper (d), the flexible, tail-like B-domain was found to be wrapped around the globular core of the molecule, thereby shielding the functional parts of the light chain. Triggered by $Ca^{2+}$, which is locally enriched at the surface of activated platelets, the B-domain is unraveled and the activity of FVIII increases. This can be seen as a stabilizing mechanism of FVIII.

Taken together, AFM imaging of VWF revealed a targeting mechanism for FVIII to sites of vascular injuries with beginning thrombus formation. FVIII is carried through the circulation and stabilized by VWF, this stable vehicle easily trespasses regions of moderate shear stress. At sites of particularly high shear stress or elongational flow VWF is strongly elongated and releases FVIII. If a white thrombus is already formed, which typically also increases elongational flow (restriction of vascular diameter), full elongation of VWF is further facilitated by the presence of activated, immobile platelets which are equipped with VWF capturing receptors GPIb and GPIIb/IIIa. This leads to a targeting of FVIII to the platelet phospholipid membrane. Short distance migration of free FVIII to the phospholipid surface is also facilitated by its $Ca^{2+}$-triggered uncovering of the phosphatidylserine binding light chain of FVIII.

More generally, the elongation dependent FVIII release, combined with present literature data, suggest a general targeting mechanism of multiple effectors that are transported by VWF. Following proteins were shown to bind to VWF more efficiently at high force, high shear or elongation: Collagen, GPIb and LRP1. Interestingly, these are immobile components of the endothelium or integrated in membranes of “solid” particles. In contrast to that, the plasma soluble effectors FVIII and ADAMTS13 lose their affinity to VWF at force/shear/elongation (ADAMTS13 is released after cleaving VWF). The concept that VWF under shear increases its affinity to immobile components and releases its soluble ligands, can explain targeting of VWF carried effectors for angiogenesis (angiopoietin-2), metastasis and cancer propagation (some integrins) or bone remodeling (osteprotegrin).

# 11. References


1 Vlot, A., Koppelman, S., Bouma, B. & Sixma, J. Factor VIII and von Willebrand factor. *J. Thromb. Haemost.* **79**, 456-465 (1998).

2 Shen, B. *et al.* The tertiary structure and domain organization of coagulation factor VIII. *Blood* **111**, 1240-1247 (2008).

3 Shiltagh, N. *et al.* Solution structure of the major factor VIII binding region on von Willebrand factor. *Blood* **123**, 4143-4151 (2014).

4 Zhou, Y. *et al.* Sequence and structure relationships within von Willebrand factor. *Blood* **120**, 449-458 (2012).

5 Springer, T. A. von Willebrand factor, Jedi knight of the bloodstream. *Blood* **124**, 1412-1425 (2014).

6 Zhang, Q. *et al.* Structural specializations of A2, a force-sensing domain in the ultralarge vascular protein von Willebrand factor. *Proc. Natl. Acad. Sci. U. S. A.* **106**, 9226-9231 (2009).

7 Emsley, J., Cruz, M., Handin, R. & Liddington, R. Crystal structure of the von Willebrand Factor A1 domain and implications for the binding of platelet glycoprotein Ib. *J. Biol. Chem.* **273**, 10396-10401 (1998).
8 Maita, N. *et al.* Crystal structure of von Willebrand factor A1 domain complexed with snake venom, bitiscetin insight into glycoprotein Ibα binding mechanism induced by snake venom proteins. *J. Biol. Chem.* **278**, 37777-37781 (2003).
9 Huizinga, E. G., van der Plas, R. M., Kroon, J., Sixma, J. J. & Gros, P. Crystal structure of the A3 domain of human von Willebrand factor: implications for collagen binding. *Structure* **5**, 1147-1156 (1997).
10 Zhou, Y.-F. & Springer, T. A. Highly reinforced structure of a C-terminal dimerization domain in von Willebrand factor. *Blood* **123**, 1785-1793 (2014).
11 Lenting, P., Casari, C., Christophe, O. & Denis, C. von Willebrand factor: the old, the new and the unknown. *J. Thromb. Haemost.* **10**, 2428-2437 (2012).
12 Wu, T., Lin, J., Cruz, M. A., Dong, J.-F. & Zhu, C. Force-induced cleavage of single VWFA1A2A3 tridomains by ADAMTS-13. *Blood* **114**, 370-378 (2010).
13 Xu, A. J. & Springer, T. A. Calcium stabilizes the von Willebrand factor A2 domain by promoting refolding. *Proc. Natl. Acad. Sci. U. S. A.* **109**, 3742-3747 (2012).
14 Zhang, X., Halvorsen, K., Zhang, C.-Z., Wong, W. P. & Springer, T. A. Mechanoenzymatic cleavage of the ultralarge vascular protein von Willebrand factor. *Science* **324**, 1330-1334 (2009).
15 Crawley, J. T., de Groot, R., Xiang, Y., Luken, B. M. & Lane, D. A. Unraveling the scissile bond: how ADAMTS13 recognizes and cleaves von Willebrand factor. *Blood* **118**, 3212-3221 (2011).
16 Feys, H., Anderson, P., Vanhoorelbeke, K., Majerus, E. & Sadler, J. Multi-step binding of ADAMTS-13 to von Willebrand factor. *J. Thromb. Haemost.* **7**, 2088-2095 (2009).
17 Tsai, H.-M. Physiologic cleavage of von Willebrand factor by a plasma protease is dependent on its conformation and requires calcium ion. *Blood* **87**, 4235-4244 (1996).
18 Deckmyn, H. & Vanhoorelbeke, K. When collagen meets VWF. *Blood* **108**, 3628-3628 (2006).
19 Schneider, S. *et al.* Shear-induced unfolding triggers adhesion of von Willebrand factor fibers. *Proc. Natl. Acad. Sci. U. S. A.* **104**, 7899-7903 (2007).
20 Kim, J., Hudson, N. E. & Springer, T. A. Force-induced on-rate switching and modulation by mutations in gain-of-function von Willebrand diseases. *Proc. Natl. Acad. Sci. U. S. A.* **112**, 4648-4653 (2015).
21 Nashimoto, Y. *et al.* Nanoscale imaging of an unlabeled secretory protein in living cells using scanning ion conductance microscopy. *Anal. Chem.* **87**, 2542-2545 (2015).
22 Wohner, N. *et al.* Shear stress-independent binding of von Willebrand factor-type 2B mutants p. R1306Q & p. V1316M to LRP1 explains their increased clearance. *J. Thromb. Haemost.* **13**, 815-820 (2015).
23 Reininger, A. J. *et al.* Mechanism of platelet adhesion to von Willebrand factor and microparticle formation under high shear stress. *Blood* **107**, 3537-3545 (2006).
24 Aponte-Santamaría, C. *et al.* Force-Sensitive Autoinhibition of the von Willebrand Factor Is Mediated by Interdomain Interactions. *Biophys. J.* **108**, 2312-2321 (2015).
25 Sing, C. E. & Alexander-Katz, A. Elongational flow induces the unfolding of von Willebrand factor at physiological flow rates. *Biophys. J.* **98**, L35-L37 (2010).
26 Colace, T. V. & Diamond, S. L. Direct observation of von Willebrand factor elongation and fiber formation on collagen during acute whole blood exposure to pathological flow. *Arterioscler. Thromb. Vasc. Biol.* **33**, 105-113 (2013).
27 Kragh, T. *et al.* High shear dependent von Willebrand factor self-assembly fostered by Platelet Interaction and controlled by ADAMTS13. *Thromb. Res.* **133**, 1079-1087 (2014).
28 Siedlecki, C. A. *et al.* Shear-dependent changes in the three-dimensional structure of human von Willebrand factor. *Blood* **88**, 2939-2950 (1996).

29 Flood, V. H. *et al.* Crucial role for the VWF A1 domain in binding to type IV collagen. *Blood* **125**, 2297-2304 (2015).
30 Lisman, T. *et al.* A single high-affinity binding site for von Willebrand factor in collagen III, identified using synthetic triple-helical peptides. *Blood* **108**, 3753-3756 (2006).
31 Jakobi, A. J., Mashaghi, A., Tans, S. J. & Huizinga, E. G. Calcium modulates force sensing by the von Willebrand factor A2 domain. *Nat. Commun.* **2**, 385-394 (2011).
32 Schrenk, G. *et al.* Recombinant VWF promotes platelet adhesion under shear stress dependent on its multimer size. *Blood* **124**, 1442-1442 (2014).
33 Lenting, P. J., Van Mourik, J. A. & Mertens, K. The life cycle of coagulation factor VIII in view of its structure and function. *Blood* **92**, 3983-3996 (1998).
34 Vlot, A., Koppelman, S., van den Berg, M., Bouma, B. & Sixma, J. The affinity and stoichiometry of binding of human factor VIII to von Willebrand factor. *Blood* **85**, 3150-3157 (1995).
35 Binnig, G., Quate, C. F. & Gerber, C. Atomic force microscope. *Phys. Rev. Lett.* **56**, 930 (1986).
36 Binnig, G., Rohrer, H., Gerber, C. & Weibel, E. Surface studies by scanning tunneling microscopy. *Phys. Rev. Lett.* **49**, 57-61 (1982).
37 Binnig, G. & Smith, D. Single-tube three-dimensional scanner for scanning tunneling microscopy. *Rev. Sci. Instrum.* **57**, 1688-1689 (1986).
38 Martin, Y., Williams, C. & Wickramasinghe, H. K. Atomic force microscope–force mapping and profiling on a sub 100-Å scale. *J. Appl. Phys.* **61**, 4723-4729 (1987).
39 Bustamante, C. & Keller, D. Scanning force microscopy in biology. *Phys. Today* **48**, 32-38 (2008).
40 Camesano, T. A., Natan, M. J. & Logan, B. E. Observation of changes in bacterial cell morphology using tapping mode atomic force microscopy. *Langmuir* **16**, 4563-4572 (2000).
41 Fotiadis, D., Scheuring, S., Müller, S. A., Engel, A. & Müller, D. J. Imaging and manipulation of biological structures with the AFM. *Micron* **33**, 385-397 (2002).
42 Ido, S. *et al.* Beyond the helix pitch: Direct visualization of native DNA in aqueous solution. *ACS nano* **7**, 1817-1822 (2013).
43 Leung, C. *et al.* Atomic force microscopy with nanoscale cantilevers resolves different structural conformations of the DNA double helix. *Nano lett.* **12**, 3846-3850 (2012).
44 San Paulo, A. & Garcia, R. High-resolution imaging of antibodies by tapping-mode atomic force microscopy: attractive and repulsive tip-sample interaction regimes. *Biophys. J.* **78**, 1599-1605 (2000).
45 Schillers, H., Medalsy, I., Hu, S., Slade, A. L. & Shaw, J. E. PeakForce Tapping resolves individual microvilli on living cells. *J. Mol. Recognit.* (2015).
46 Dufrêne, Y. F., Martínez-Martín, D., Medalsy, I., Alsteens, D. & Müller, D. J. Multiparametric imaging of biological systems by force-distance curve-based AFM. *Nature methods* **10**, 847-854 (2013).
47 Garcia, R. & Proksch, R. Nanomechanical mapping of soft matter by bimodal force microscopy. *Eur. Polym. J.* **49**, 1897-1906 (2013).
48 Sahin, O., Magonov, S., Su, C., Quate, C. F. & Solgaard, O. An atomic force microscope tip designed to measure time-varying nanomechanical forces. *Nat. Nanotechnol.* **2**, 507-514 (2007).
49 Rico, F., Gonzalez, L., Casuso, I., Puig-Vidal, M. & Scheuring, S. High-speed force spectroscopy unfolds titin at the velocity of molecular dynamics simulations. *Science* **342**, 741-743 (2013).
50 Touhami, A., Jericho, M. H. & Beveridge, T. J. Atomic force microscopy of cell growth and division in Staphylococcus aureus. *J. Bacteriol.* **186**, 3286-3295 (2004).
51 Ando, T. *et al.* A high-speed atomic force microscope for studying biological macromolecules. *Proc. Natl. Acad. Sci. U. S. A.* **98**, 12468-12472 (2001).
52 Ando, T., Uchihashi, T. & Kodera, N. High-speed AFM and applications to biomolecular systems. *Ann. Rev. Biophys.* **42**, 393-414 (2013).

53 Kodera, N., Yamamoto, D., Ishikawa, R. & Ando, T. Video imaging of walking myosin V by high-speed atomic force microscopy. *Nature* **468**, 72-76 (2010).

54 Kim, D. & Sahin, O. Imaging and three-dimensional reconstruction of chemical groups inside a protein complex using atomic force microscopy. *Nat. Nanotechnol.* **10**, 264-269 (2015).

55 Cao, W., Krishnaswamy, S., Camire, R. M., Lenting, P. J. & Zheng, X. L. Factor VIII accelerates proteolytic cleavage of von Willebrand factor by ADAMTS13. *Proc. Natl. Acad. Sci. U. S. A.* **105**, 7416-7421 (2008).

56 Cao, W. *et al.* Light chain of factor VIII is sufficient for accelerating cleavage of von Willebrand factor by ADAMTS13 metalloprotease. *J. Biol. Chem.* **287**, 32459-32466 (2012).

57 Skipwith, C. G., Cao, W. & Zheng, X. L. Factor VIII and platelets synergistically accelerate cleavage of von Willebrand factor by ADAMTS13 under fluid shear stress. *J. Biol. Chem.* **285**, 28596-28603 (2010).